Corrosion and Tribocorrosion Kinetics of Al-based Concentrated Alloys in Aqueous Sodium Chloride Solution

Jia Chen

Dissertation submitted to the faculty of the Virginia Polytechnic Institute and State University in partial fulfillment of the requirements for the degree of

Doctor of Philosophy

in

Materials Science and Engineering

Wenjun Cai, Chair

Xianming Bai

Sean G. Corcoran

Xiaoting Jia

November 12, 2021

Blacksburg, VA

Keywords: Al-based concentrated alloys, Corrosion, Tribocorrosion, Passive films, EIS, XPS

Corrosion and Tribocorrosion Kinetics of Al-based Concentrated Alloys in Aqueous Sodium Chloride Solution

Jia Chen

Abstract

Commercial aluminum (Al) alloys are often precipitation strengthened to improve strength and wear resistance. However, localized corrosion due to the galvanic coupling between the precipitates and Al matrix often leads to degraded performance when these alloys are exposed to corrosive environment. In this work, Al-based solid solution was synthesized to simultaneously improve the strength and corrosion resistance of Al alloys, which ultimately led to high tribocorrosion resistance. Specifically, the effects of testing condition (e.g. sliding frequency) and alloying effects (e.g. Mn and Mo) on the corrosion and tribocorrosion behavior of Al-based binary and ternary solid solutions were studied.

To understand the effects of wear condition on the depassivation-repassivation kinetics during tribocorrosion, in the first study, the tribocorrosion behaviors of Al-20 at.%Mn alloys were investigated in simulated seawater by changing the sliding frequency from 0.05 to 1 Hz in reciprocal motion. The results show that the depassivation rate of passive film increased with increasing sliding frequency. Mechanical wear also increased with increasing sliding frequency, which was mainly related to the increase of coefficient of friction and real contact area. Chemical wear tended to increase with scratching frequency, most likely due to faster repassivation kinetics at lower frequency. The surface layer was analyzed by cross-sectional transmission electron microscopy, indicating the passive film was primarily consisted of aluminum oxide where manganese was selectively dissolved.

Despite extensive past research, the fundamental understanding of the alloying effects on the atomistic structure, composition, and chemical state of the passive layer of Al alloys and their formation mechanism is still not well understood. In the second study, the effects of Mn on the aqueous corrosion of Al-Mn alloys were investigated. It was confirmed that Mn alloying could enhance the corrosion resistance of Al without participating in the surface oxidation. Atom probe tomography analysis confirmed the absence of Mn in the anodized and corroded surface of Al-Mn alloys. The selective dissolution of Mn in these alloys was believed to increase the free volume at the metal/oxide interface to facilitate the formation of a denser, thinner oxide layer with closer to stoichiometry composition, leading to its enhanced corrosion resistance than pure Al.

Lastly, to better understand the corrosion and tribocorrosion resistance of Al-based lightweight concentrated alloys and the effects of alloying concentrations on the structure and property of the passive layer, the third study investigated the effects of a passive element (Mo) and non-passive element (Mn) on the corrosion and tribocorrosion behavior of Al-Mn-Mo alloys. Specifically, $Al_{80}Mn_8Mo_{12}$ exhibited higher corrosion resistance than $Al_{80}Mn_{20}$ due to the formation of a more compact and less defective passive film, as explained by the roles Mo played in both the substrate and the passive film. It was found that the pitting potential and corrosion current density of Al-Mn-Mo increased with Mo%. The effect of Mo alloying concentration on the tribocorrosion behavior of Al-Mn-Mo alloys was investigated as well. Adding Mo to Al-Mn alloys led to a lower wear and tribocorroison resistance of Al-Mn-Mo alloys. In addition, decreasing Mn and Mo concentrations resulted in a reduction of the tribocorrosion resistance in the ternary alloy, which was mainly dominated by the mechanical response under the selected testing conditions.

Corrosion and Tribocorrosion Kinetics of Al-based Concentrated Alloys in Aqueous Sodium Chloride Solution

Jia Chen

General Audience Abstract

Various critical current and future applications in the fields of aerospace, transportation, energy, and biomedical industries require not only a strong and tough metal, but one that is robust and reliable when interacting with some very corrosive environment. Such corrosive environment is testing the limits of most engineering metals and challenging the current understanding of the underlying degradation mechanism. For example, strength and wear resistance in most precipitation-hardened Al (aluminum) alloys is often achieved at the expense of sacrificed corrosion resistance, mainly due to micro-galvanic coupling between the soft matrix and hard precipitates. In addition, the performance of Al alloys deteriorates dramatically when there is combined wear and corrosion, i.e. tribocorrosion attack at the surface, due to the depassivation on the wear track as a result of mechanical removal of the passive film.

Recent study shows that alloying Al with appropriate transition metals in supersaturated solid solution simultaneously improves the corrosion and wear resistance of Al. In this thesis, Al-Mn and Al-Mn-Mo solid solutions was synthesized and studied to understand the effects of testing condition (e.g. sliding frequency) and alloy composition (e.g. Mn and Mo concentration) on the corrosion and tribocorrosion behavior. First, the depassivation mechanism during tribocorrosion of Al-Mn alloys was investigated by performing tribocorrosion test using different sliding frequency from 0.05 to 1 Hz in 0.6 M NaCl aqueous solution. Results showed that both chemical and mechanical wear increased with increasing frequency. The mechanical wear increased

with scratching frequency due to faster depassivation rate and increased real contact area, while chemical wear increased with frequency due to higher repassivation kinetics. Secondly, the effects of Mn on the aqueous corrosion and passivation of Al-Mn solid solution alloys were investigated by electrochemical experiments and advanced surface characterization. It was found that Mn addition enhanced the corrosion resistance of Al without participating in the surface oxidation. A denser, thinner oxide layer was formed on Al-Mn due to the increased free volume at the metal/oxide interface as a result of Mn dissolution. Lastly, the effects of alloying concentration on the aqueous corrosion and tribocorrosion of Al-Mn-Mo alloys were studied experimentally. The pitting potential and corrosion current density of Al-Mn-Mo were found to increase with Mo%. The passive film thickness depended on the total alloy concentration, while its compactness and defect density on the individual ones. The tribocorrosion resistance of Al-Mn-Mo alloys decreased with increasing Mn and Mo concentrations. In summary, the results from this thesis develop mechanistic understanding of the corrosion and tribocorrosion mechanisms of Al-based solid solution alloys, which sheds light on a new alloy design strategy for making lightweight, strong, and corrosion-resistant metals.

Dedication

To my mom and dad, Qiuying Chen and Ming Chen

Acknowledgment

First of all, I would like to express my special thanks of gratitude to my advisor Prof. Wenjun (Rebecca) Cai who gave me the golden chance to do this wonderful project on the corrosion and tribocorrosion behaviors of Al-based concentrated alloys. When my first day becoming her student, I realized that I would have a great mentor to lead me in my academic career. Her patient guidance and support continued throughout my whole Ph.D. career at Virginia Tech. She helped me a lot in doing research and I came to know about so many new things. Her passion for research greatly influenced my progress towards a Ph.D. student. What impressed me most was that when I encountered a bottleneck in my research, she came to the lab to discuss with me and gave me a lot of guiding suggestions. You know, this meant a lot to a new Ph.D. student, from which I learned how to solve problems in experiments. At the same time, under her guidance, I know how to design and plan a project by myself. Here all the gratitude will be a word: THANK YOU!

Secondly, I would like to give my thanks to all my other committee members, Professors Xianming (David) Bai, Sean G. Corcoran, and Xiaoting Jia. Thank you for your willingness to become my committee members. Thank you for your valuable suggestions in my preliminary exam and directional suggestions for my future research. With your help, my doctoral career has become very meaningful.

Equally important, I would like to express my sincerest gratitude to Dr. Chuang Deng and Dr. Jianwei Xiao from University of Manitoba. Thanks for your work on molecular dynamic simulation, your knowledge in simulation has given us strong support in our experiments. With your support, my paper can be successfully published in *Corrosion Science*.

I am thankful to former and present staff from Nanoscale Characterization and Fabrication Laboratory (NCFL), Virginia Tech. Dr. Weinan Leng has given me great help on X-ray photoelectron spectroscopy. Without your help and training, I could not quickly understand XPS and completed material characterization. Stephen McCartney

helped and trained me in using scanning electron microscopy, and he gave me very helpful suggestions when I had questions on the characterization. For transmission electron microscopy measurement, Dr. Mitsu Murayama, Dr. Christopher Winkler, and Dr. Chang-Yu Hung gave me great help in training and instrument support. Ya-Peng Yu helped me in the lift-out section of TEM sample preparation.

I am thankful to Dr. Jonathan D. Poplawsky from Oak Ridge National Laboratory. Only with your help in the APT characterization, I can give a better description on the origin passivity of Al-Mn solid solution.

The financial support from the US National Science Foundation (NSF) , and Virginia Tech is greatly appreciated.

I also extend my thanks to my former and present colleagues in our group: Dr. Hesham Mraied, Wenbo Wang, Kaiwen Wang, and Zhengyu Zhang for their constant and patient support on my research.

Lastly, I would like to thank my parents, Qiuying Chen and Ming Chen, for their unconditional love and support throughout my Ph.D. career. Thank you for giving me the strength to pursue my dreams. No matter what difficulties I encounter, you will listen to me and give me advice. I love you forever!

Attribution

In my entire Ph.D. career, some colleagues and staff assisted me with some parts of my dissertation, including sample preparation, characterization, simulation and writing/editing the manuscripts. Their contributions are summarized as follow:

Chapter 2: Dr. Yusuf Emirov (Metrology Scientist, USF, USA) performed FIB sample preparation. Richard Everly (Cleanroom Engineer, USF, USA) conducted physical vapor deposition for Al-Mn system alloys. Dr. Christopher Winkler (now, TEM lab manager at NCSU, USA) performed TEM characterization. I performed all the experiments and characterization in this manuscript. I wrote the whole manuscript and served as first author. Prof. Wenjun Cai served as the corresponding author and was involved in the editing of the manuscript.

Chapter 3: Dr. Jianwei Xiao (Postdoc, University of Manitoba, Canada) performed the MD simulation and served as co-first author. Dr. Jonathan Poplawsky (Research staff, Oak Ridge National Laboratory, USA) performed the analysis of atom probe tomograph. Prof. F. Marc Michel (Virginia Tech, USA) performed X-ray diffraction characterization. Dr. Weinan Leng (NCFL Instrument Specialist, Virginia Tech, USA) gave me suggestion on the XPS data analysis. I performed all the experiments and the remaining characterization in this manuscript. I wrote the manuscript and served as co-first author. Prof. Chuang Deng and Prof. Wenjun Cai both served as the corresponding author and were involved in the editing of the manuscript.

Chapter 4: Dr. Jianwei Xiao (Postdoc, University of Manitoba, Canada) performed the MD simulation. Dr. Chang-Yu Hung (Postdoc, The Johns Hopkins University, USA) performed the TEM analysis on Al-Mn-Mo samples. Dr. Jing Zhao (Laboratory Specialist Senior, Virginia Tech) performed X-ray diffraction characterization. Wenbo Wang performed FIB sample preparation. I performed all the experiments and the remaining characterization. Prof. Chuang Deng and Prof. Wenjun Cai both served as the corresponding author and were involved in the editing of the manuscript.

Table of Contents

List of Figures

List of Tables

Chapter 1: Introduction

1.1 Background

1.1.1 Metal corrosion

Corrosion is the result of the destruction of a metal or metallic alloy following an electrochemical reaction with the environment. Corrosion returns the metal to chemical compounds that are similar or identical to the minerals. In the process of corrosion, the following components are included: electronic path, electrolyte, anodic reaction, and cathodic reaction. For corroding of metal *M*, the anodic (oxidation) reaction is of the form:

$$M \rightarrow M^{n+} + ne^{-}, \tag{1.1}$$

where *n* is number of electrons produced, which is equal to the valence of *M*. The common forms of cathodic reaction are shown below [1]:

$$O_2 + 2H_2O + 4e^{-} \rightarrow 4OH^{-} \text{ (Oxygen reduction in neutral solution)}, \tag{1.2}$$

$$O_2 + 4H^{+} + 4e^{-} \rightarrow 2H_2O \text{ (Oxygen reduction in acidic solution)}, \tag{1.3}$$

$$2H_2O + 2e^{-} \rightarrow H_2 + 2OH^{-} \text{ (Water reduction)}, \tag{1.4}$$

$$2H^{+} + 2e^{-} \rightarrow H_2 \text{ (Hydrogen reduction)}. \tag{1.5}$$

The schematic diagram of metal M dissolution in acidic solution is taken as an example in Fig. 1.1. Electrons migrate to the adjoining surface during metal dissolution, they react with H^{+} to form H_2. Acidic solution, the carrier for ions, is called the electrolyte. Metal is corroded and presents a dynamic equilibrium in a solution, the electrical potential difference between the metal and the solution can be given by Nernst equation [1-3]:

$$E_{M^{n+}/M} = E^{0}_{M^{n+}/M} - \frac{RT}{nF}\ln[M]^{n+}, \tag{1.6}$$

and the equilibrium reaction for the reduction reaction is shown below:

$$E_{Ox/Red} = E^{0}_{Ox/Red} - \frac{RT}{nF}\ln[Ox]^{a}/[Red]^{b}, \tag{1.7}$$

where [M] is the activity of the metal, [Ox] is the oxidizing species, and [Red] is the reducing species. E^{0} is the standard potential of the half cell. The standard potential

of various metals can be found in Table 1.1. A metal with more negative standard potential compared to that of the coupled cathodic reaction will be corroded when placed in a corrosive environment. Pourbaix diagram (see Fig. 1.2) can be used to illustrate the corrosion thermodynamics during such process, where the electrochemical potential is plotted vs. the pH of water at 25 ℃ [2]. In the Pourbaix diagram of metal M (e.g., Fe), as shown in Fig. 1.3, it can be seen that the different electrochemical state (immunity, corrosion, or passivation) of the metal occurs as a function of pH and potential.

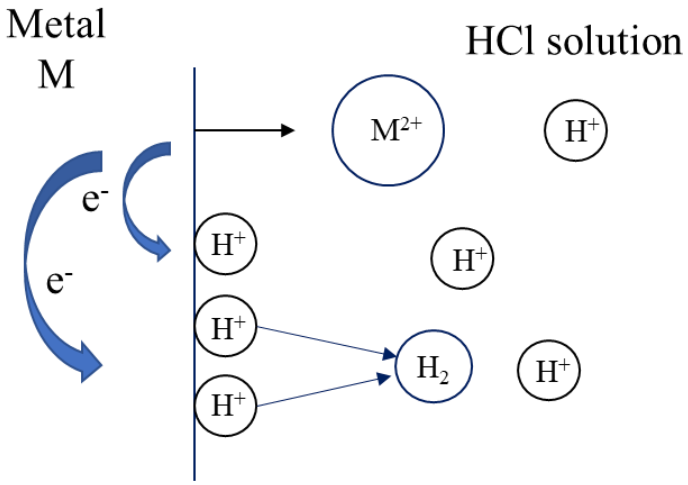

Figure 1.1 The schematic diagram of metal dissolution.

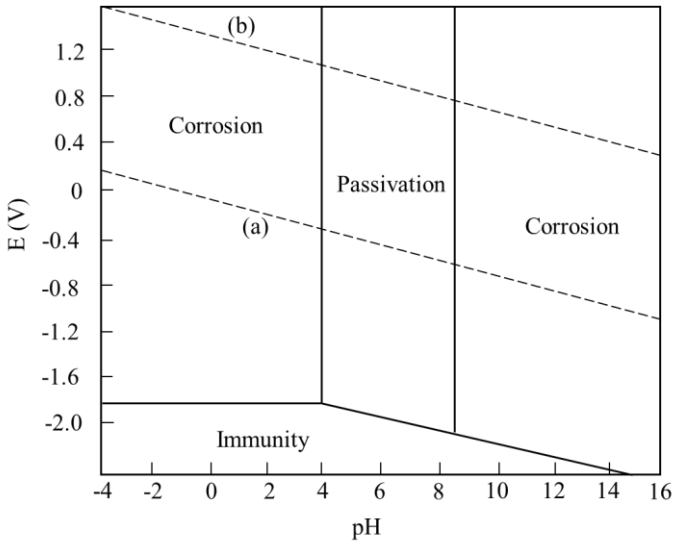

Figure 1.2 Pourbaix diagram for the electrochemical potential vs. the pH of water at 25 ℃.

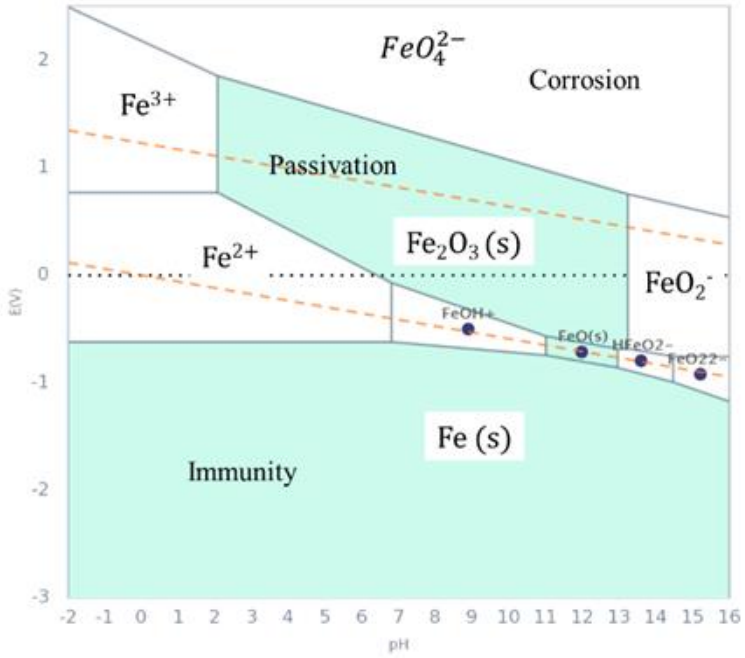

Figure 1.3 The Pourbaix diagram of pure Fe at 25 ℃.

Pourbaix diagrams are useful in informing the phase equilibrium during corrosion, however, it gives no information about the corrosion kinetics, e.g., corrosion rate, which is often estimated from the experimentally measured corrosion current (I_{corr}) by using the Faraday's law as

$$I_{corr} = \frac{nFm}{at}, \tag{1.8}$$

where n is the valence of the metal, F is Faraday's constant (96,500 C/mol), a is the atomic mass of the metal, m is the mass of corroded metal, and t is the time that the current was applied. To measure corrosion kinetics, two commonly used electrochemical measurements including $i = i_{corr}[\frac{\alpha nF\eta}{RT} - \frac{(1-\alpha)nF\eta}{RT}]$ potentiodynamic (PD) polarization and electrochemical impedance spectroscopy (EIS) tests, will be discussed in the following sections.

Table 1.1 Standard electromotive force potentials (reduction potentials) [4].

	Reduction reaction	**E^0 (V_{SHE})**
↑ Noble	$Au^{3+} + 3e^- = Au$	+1.498
	$Cl_2 + 2e^- = 2Cl^-$	+1.358
	$O_2 + 4H^+ + 4e^- = 2H_2O$	+1.229
	$Pt^{2+} + 2e^- = Pt$	+1.118
	$O_2 + 2H_2O + 4e^- = 4OH^-$	+0.820
	$Ag^+ + e^- = Ag$	+0.799
	$Fe^{3+} + e^- = Fe^{2+}$	+0.771
	$Cu^{2+} + 2e^- = Cu$	+0.342
	$Sn^{4+} + 2e^- = Sn^{2+}$	+0.150
	$2H^+ + 2e^- = H_2$	+0.000
	$Pb^{2+} + 2e^- = Pb$	-0.126
	$Sn^{2+} + 2e^- = Sn$	-0.138
	$Ni^{2+} + 2e^- = Ni$	-0.250
	$Co^{2+} + 2e^- = Co$	-0.277
	$Cd^{2+} + 2e^- = Cd$	-0.403
	$2H_2O + 2e^- = H_2 + 2OH^-$	-0.413
	$Fe^{2+} + 2e^- = Fe$	-0.447
	$Cr^{3+} + 3e^- = Cr$	-0.744
	$Zn^{2+} + 2e^- = Zn$	-0.762
Active ↓	$Al^{3+} + 3e^- = Al$	-1.662
	$Mg^{2+} + 2e^- = Mg$	-2.372
	$Na^+ + e^- = Na$	-2.710
	$K^+ + e^- = K$	-2.931

1.1.1.1 PD tests

PD tests can provide important and useful information about corrosion mechanisms, corrosion rates, and the corrosion sensitivity of a particular material in a

given environment. In PD test, the potential varies at a selected range and rate by a sweep or a step mode. An adequate current is generated due to oxidation or reduction reaction on the metal surface. The electric potential drives the anodic or cathodic reaction. The potential as a function of current (I or log I) for each measured point leads to obtain a polarization curve. In Fig. 1.4, the open circuit potential (E_{ocp}) is the potential where the total anodic current equals the total cathodic current. The corrosion potential and the corrosion current can be estimated at the intersection of extrapolated cathodic and anodic current. The corrosion rate of the metal can be computed by linear polarization methods. Combined with polarization resistance (R_p) and Tafel slopes, the corrosion current density (i_{corr}) can be obtained from one form of the Stern-Geary equation below:

$$i_{corr} = \frac{B}{R_P}, \tag{1.9}$$

where R_p is the change in potential that was divided by the current, it is determined by the slope of the line segment of the polarization curve (Tafel). B is given below:

$$B = \frac{\beta_a \beta_c}{2.3(\beta_a + \beta_c)}. \tag{1.10}$$

The β coefficient can be obtained from a Tafel plot or estimated from the experience with the testing system.

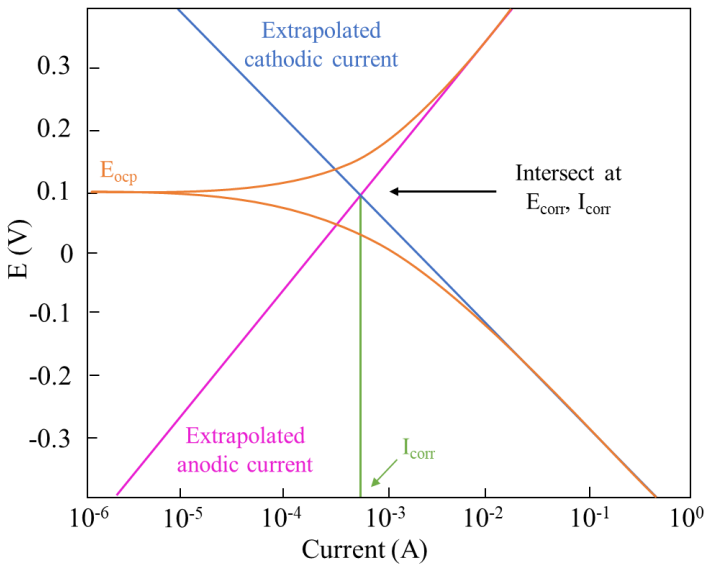

Figure 1.4 The schematic potentiodynamic polarization curve.

In steady-state and simple activation polarization conditions, ignoring mass

transport, the total net current density (i) can be expressed by the Butler-Volmer equation [2, 5]:

$$i = i_{corr}[\frac{\alpha nF\eta}{RT} - \frac{(1-\alpha)nF\eta}{RT}], \quad (1.11)$$

where η is the overpotential, α is the half reaction transfer coefficient, β_a and β_c can be calculated from Tafel slopes, $\beta_a = 2.3RT/\alpha nF$ and $\beta_c = -2.3RT/(1-\alpha)nF$ [3].

1.1.1.2 EIS tests

EIS, a non-destructive technique, is used to determine a number of electrochemical parameters such as polarization resistance and double layer capacitance. The response of corroded electrode to alternating potential signal with small amplitude and large frequency change is analyzed from EIS results. EIS can be used to obtain different parameters such as corrosion rate, reaction kinetics, mass transport, and dielectric properties [6]. EIS can also be used to detect relaxation phenomena over a wide frequency range, its steady-state properties, and availability of time-dependent data [7]. The main disadvantage of EIS is the complex data analysis with different equivalent circuits when fitting experimental data [7]. The impedance, $Z(\omega)$, can be expressed in terms of real, $Z'(\omega)$, and imaginary, $Z''(\omega)$.

$$Z(\omega) = Z'(\omega) + Z''(\omega). \quad (1.12)$$

The impedance behavior can be expressed in Nyquist plots (Fig. 1.5(a)) of $Z''(\omega)$ as a function of $Z'(\omega)$ or in Bode plots (Fig. 1.5(b)) of $\log|Z|$ and $\log\theta$ versus frequency f in Hz, where $\omega = 2\pi f$ [4]. The one major shortcoming is that the frequency used to record the point cannot be told from the plot. The equivalent electrical circuit in the Nyquist plot is used to characterize the semicircle of a single time constant, where R_s is the electrolyte resistance, R_p is the polarization resistance, and C is the passive layer capacitance for ideal behavior which can be replaced by constant phase element (CPE) for non-ideal behavior. Unlike the Nyquist Plot, the Bode Plot does show frequency information. At low frequency, the impedance equals $(R_p + R_s)$, while it equals R_s at high frequency.

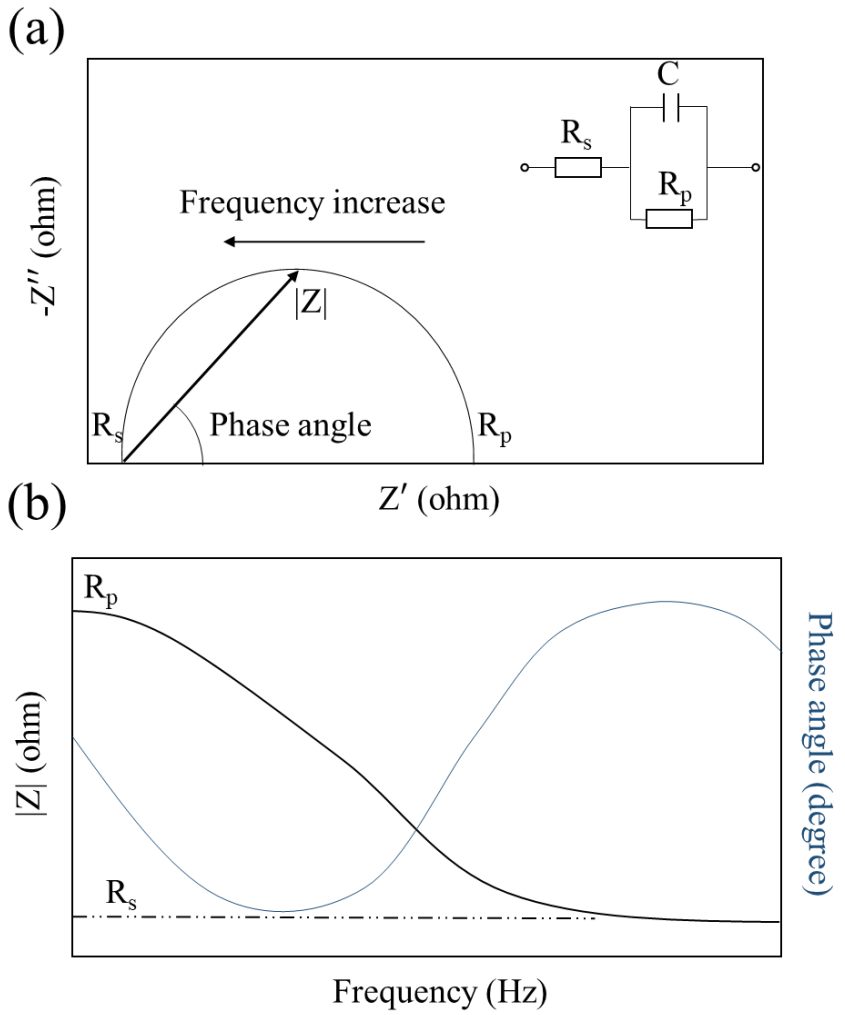

Figure 1.5 The impedance of (a) Nyquist plot and (b) Bode plot.

1.1.2 Metal tribocorrosion

Tribocorrosion describes the degradation of materials due to the effect of chemical and mechanical action simultaneously in a tribological contact [8]. Tribocorrosion can take place under a variety of conditions (i.e., sliding, rolling, fretting, impingement) in a corrosive environment. Tribocorrosion is often measured via the synergistic, mechanistic, and third-body approach, as detailed below.

1.1.2.1 Synergistic approach

In synergistic approach, the pure corrosion (C_0) is measured in a separate test without the mechanical part, the pure wear (W_0) is measured under a cathodic potential of 1 V versus OCP without the corrosion, and the result of wear-corrosion is defined as

the total material loss (T). According to Eqn. 1.13, the total material loss after tribocorroison can be expressed by the sum of pure corrosion, pure wear and the synergy of wear and corrosion (S).

$$T = W_0 + C_0 + S. \tag{1.13}$$

The synergy of wear and corrosion (S) is defined as the sum of the change in wear-accelerated corrosion (ΔC_W) and the change in corrosion-accelerated wear (ΔW_c), which is given below:

$$S = \Delta C_W + \Delta W_C. \tag{1.14}$$

From the above, some factors can be calculated, including the total synergism factor (Eqn. 1.15), corrosion augmentation factor (Eqn. 1.16), and the wear augmentation factor (Eqn. 1.17).

$$\text{Total synergism factor } = T/(T - S), \tag{1.15}$$

$$\text{Corrosion augmentation factor } = (C_0 + \Delta C_0)/C_0, \tag{1.16}$$

$$\text{Wear augmentation factor } = (W_0 + \Delta W_0)/W_0. \tag{1.17}$$

However, the synergistic approach has been proved to be dependent on the applied cathodic potential, which was used to suppress the metal dissolution. According to the study from Espallargas and Mischler in 2010 [9], they found that the oxidation of the alloy even occurred at cathodic potential in nitric acid, resulting in a material loss at cathodic potential similar to that at anodic potentials. Therefore, wear under cathodic protection should not be considered as a pure wear in the solution.

1.1.2.2 Mechanistic approach

The mechanistic approach includes two parts: wear-accelerated corrosion and mechanical wear. It can be assumed that the pure corrosion on the passivated area is negligible, and only the wear-accelerated corrosion is considered in the worn area. The total material loss (V_t) is defined as the sum of chemical material loss (V_{chem}) due to the wear-accelerated corrosion and mechanical wear (V_{mech}), the equation is given below:

$$V_t = V_{chem} + V_{mech}. \tag{1.18}$$

Especially in passive metals, V_{chem} is calculated by the sum of corrosion in both of the passive aeras and the depassivated areas, which is quantified by measuring the current flowing in a potentiostatic tribocorrosion experiment. V_{chem} is determined by using Faraday's law:

$$V_{chem} = \frac{QM}{nF\rho}, \tag{1.19}$$

where Q is the total charge transferred during tribocorrosion, M is the molar mass, n is the number of electrons transferred for the oxidation reaction, F is the Faraday's constant (96,500 C/mol), and ρ is the metal density. To quantify V_{chem}, there are two assumptions: (1) the measured current density in a potentiostatic experiment should be equal to the anodic current (cathodic current is negligible) and (2) the charge number n in the oxidation reaction should be determined by detailed surface analysis (X-ray photoelectron spectroscopy). The total material loss (V_t) can be measured by using an optical profilometer. Then, the mechanical wear (V_{mech}) can be calculated as:

$$V_{mech} = V_t - V_{chem}. \tag{1.20}$$

However, the mechanistic approach only considers the removal rate of chemical and mechanical by the surface chemistry, the simple calculation cannot be used to understand the fundamental tribocorrosion sliding systems, such as in the phenomena of the build-up of third bodies.

1.1.2.3 Third body approach

In tribocorrosion sliding contacts, the mechanical wear could cause the formation of wear debris on the worn area. Those wear debris influence wear morphology, V_{mech} and even V_{chem} value of the material [10]. Barril et al. [11] found that the wear particles from the Ti6Al4V alloy on the worn area can wedge onto the space between the ball and the sample, and a higher value of V_{chem} can be observed. Fig. 1.6 illustrates the material flows and reactions in a tribocorrosion process. It can be seen that the wearing process causes the wear particles formation, which will be ejected to the solution or transferred to a third body. In addition, the wear-accelerated corrosion can be observed in both of the metal and a third body. The total material loss (V_t) can

be calculated as:

$$V_t = V_{met}^{particle} + V_{met}^{ions} + V_{met}^{oxide}, \quad (1.21)$$

where $V_{met}^{particle}$ is the solid metal particles (third body), V_{met}^{ions} is the dissolved metal ions in the solution, and V_{met}^{oxide} is the passive film oxidized by the metal. $V_{met}^{particle}$ can be ejected from the contact ($V_{met,particle}^{ejected}$), oxidized ($V_{met,particle}^{ions}$ or $V_{met,particle}^{oxide}$):

$$V_{met}^{particle} = V_{met,particle}^{ejected} + V_{met,particle}^{ions} + V_{met,particle}^{oxide}. \quad (1.22)$$

The wear-accelerated corrosion (V_{chem}) should include metal and metal particles:

$$V_{chem} = V_{met}^{ions} + V_{met}^{oxide} + V_{met,particle}^{ions} + V_{met,particle}^{oxide}. \quad (1.23)$$

Substituting Eqn. 1.22 to Eqn. 1.21, the Eqn. 1.21 can be rewritten as:

$$V_t = V_{chem} + V_{met,particle}^{ejected}. \quad (1.24)$$

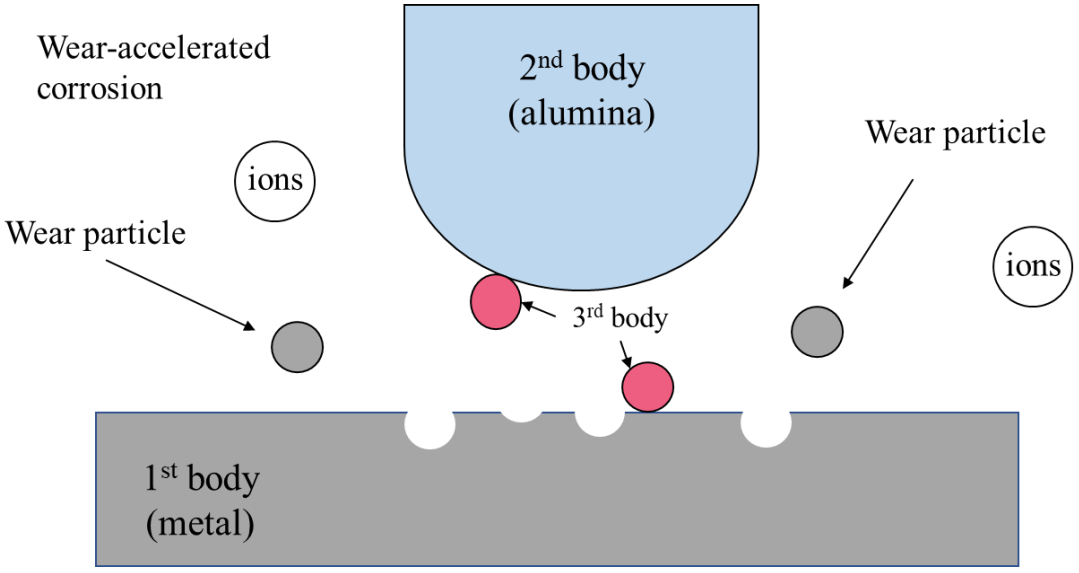

Figure 1.6 The schematic of the material flows and reactions in a tribocorrosion process.

1.2 Corrosion and tribocorrosion behavior for Al alloys

Al and its alloys are often used in automotive, aerospace, and marine applications due to their lightweight, high strength and good corrosion resistance. Al is a passive metal in neutral solution. The exposed surface of aluminum and its alloys can form an inert aluminum oxide when reacting with oxygen, which will prevent further oxidation [12]. However, such materials are still susceptible to corrosion when used in corrosive

environment, such as in salty air and sea water. The corrosion behavior of Al and Al alloys can be understood from their thermodynamics and corrosion kinetics, which will be discussed in section 1.2.1. Common corrosion modes of Al alloys include pitting corrosion, crevice corrosion, intergranular corrosion, and tribocorrosion etc., which will be discussed in section 1.2.2.

1.2.1 Thermodynamics and kinetics of Al corrosion

In terms of thermodynamics, Pourbaix diagram shows stable phases as a function of pH and potential, where potential is defined with respect to the standard hydrogen electrode. From Pourbaix diagram of pure Al-water system shown in Fig. 1.7, metallic state of Al is stable at potential below -1.8 V vs. SHE. In the pH range of -4 to 4 above -1.8 V, Al is oxidized to Al^{3+} in acidic environment. The oxide film is thermodynamically stable in the pH range of 4 to 8.5. At pH higher than 8.5, Al is corroded to the aluminate cation, AlO_2^-. However, the corrosion behavior of Al and Al alloys really depends on the protectiveness of its passive film [13]. Especially in halogens containing media, Al and Al alloys may suffer the localized corrosion. Once the passive film is destroyed, the pitting corrosion occurs and the pH value of the environment will be changed significantly due to the hydrolysis of Al to Al^{3+} and the reaction of Al^{3+} with Cl^- and water shown below [14]:

$$Al^{3+} + 2H_2O \rightarrow H^+ + Al(OH)^{2+}, \quad (1.25)$$

$$Al(OH)^{2+} + Cl^- \rightarrow Al(OH)Cl^+, \quad (1.26)$$

$$Al(OH)Cl^+ + H_2O \rightarrow Al(OH)_2Cl + H^+. \quad (1.27)$$

The corrosion kinectics will follow the corroison mechanism of metal that mentioned in section 1.1.1.

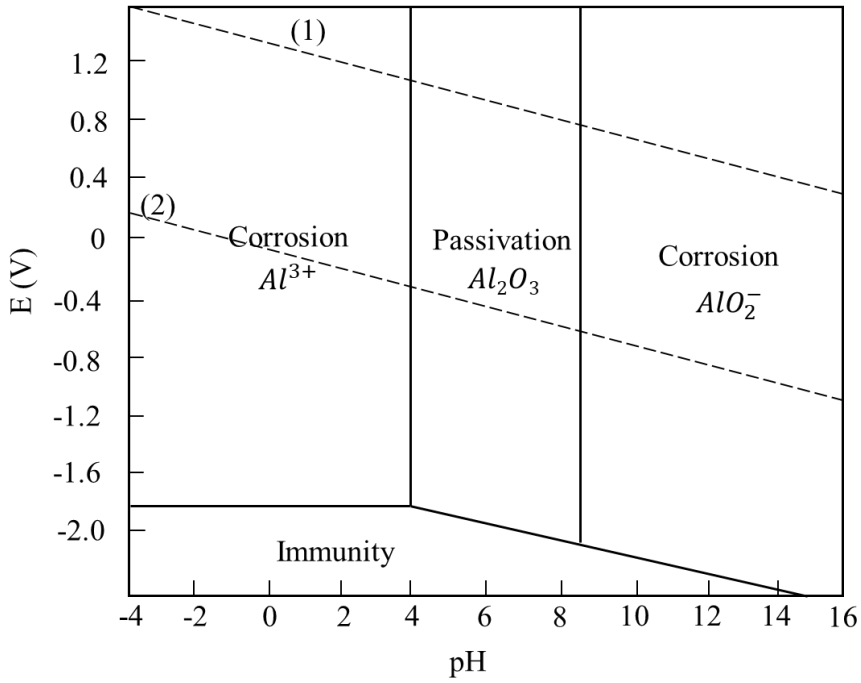

Figure 1.7 The schematic Pourbaix diagram of Al-water system at 25 ℃.

1.2.2 Corrosion modes for Al alloys

Pitting corrosion

Pitting is a common phenomenon in the corrosion of aluminum alloys. It is a cavity, hole or pit that forms in a small area or point. A small and narrow pit may cause the failure of the engineering system, though the whole metal loss is minimal. Pits can form on the surface of Al alloys exposed to atmosphere, salt water, or neutral electrolytes. In highly acidic or alkaline electrolytes, pitting often occurs in pH range of 4.5 to 9.0 due to the instability of the passive film. The negatively charged ions (e.g., Cl^-) accumulated on the surface of Al alloys and penetrated the passive film, the localized breakdown occurred at a specific pitting potential, E_{pit}, which is related to the material, pH, chloride concentration, and temperature. The pitting potentials of Al alloys have been determined by using controlled potential techniques [15, 16]. Pit propagation can take place when the breakdown occurred. The shape of pits in Al alloys can be various from shallow to cylindrical holes, and the pit cavity is hemispherical. This is usually used to distinguish intergranular corrosion, which confines the attack along grain boundaries.

It has been known that Al and Al alloys can form an amorphous semiconducting

passive film in the pH values of 4-9 solutions [17]. However, the passive film can still be breakdown by different halide ions. Rehim et al. [18] found that the corrosion rate of Al and some alloys can be increased by the addition of NaCl, NaBr and NaI in sulphate solutions, because the halide ions penetrated the passive film. Mazhar et al. [19] studied the electrochemical behavior of Al in both acidic and neutral chloride-containing solutions, suggesting the oxide film can be dissolved in the chloride-containing solutions. Natishan et al. [20] studied the chloride ion interaction with oxide-covered aluminum, the pitting potential decreased as the Cl^- concentration increased in the oxide film.

To minimize pitting corrosion, some major principles have been concluded below:

1) Reduce chloride ion concentration, temperature, acidity, and oxidizing agents in the aggressive environment.
2) Improve the pitting resistance of construction, like using 3xxx and 5xxx series alloys.
3) Cathodic protection would be a good solution to minimize the pitting corrosion.

Crevice corrosion

Crevice corrosion of Al alloys is the localized attack at the gap between two joining surfaces. The damage caused by crevice corrosion is usually confined to Al matrix in or near a local area of the connection surface. In chloride ion containing environment, a local cell is created at the mouth of crevice. Outside of the crevice is the cathode, which is the oxygen-rich area. Chlorides concentrate inside the crevice, representing oxygen-depleted zone (the anode). When crevice corrosion occurred, the anode area became acidic, while the cathode area became alkaline. This type of corrosion is unavoidable because of the functional design and exposure period. For example, stacked sheet metal, marine deposits, and riveted connections. There are some major factors influencing crevice corrosion, including crevice type, crevice geometry, material, and environment.

To prevent crevice corrosion, crevices should be eliminated in the beginning of

the design stage. Polymeric sealants and coating combinations are another method to protect the surface from crevice corrosion.

Intergranular corrosion

Intergranular corrosion is also known as intercrystalline corrosion. This type of corrosion usually occurs in most heat treatable and high strength products (2xxx and 7xxx alloys) [21, 22]. In a completely recrystallized grain structure, intergranular corrosion can appear depending on the Al alloy. It is often related to copper depleted area or to anodic precipitates in the grain boundary area of 5xxx Al alloys. In general, intergranular corrosion penetrates more quickly than pitting corrosion, but it will reach a limited depth due to the limited transport of oxygen and narrow corrosion path. When the corrosion reaches its maximum depth, intergranular corrosion spreads out the whole surface. This phenomenon is different from pitting corrosion, which occurs as discrete sites.

Tribocorrosion

Tribocorrosion is another factor of aluminum degradation in industrial application. This phenomenon usually occurred including marine, nuclear, aerospace, and biomedical applications. The protective oxide layer on the aluminum surface can be destroyed by the mechanical process due to wear and wear accelerated corrosion. In the automotive industry, Al parts could degrade in corrosive environment when the passive film was removed or damaged, leading to higher corrosion rate and wear rate in the tribocorrosion process.

During tribocorrosion process the passive film on the worn surface of Al alloys was removed, while the unworn area still remained the passive film. The worn area and the unworn area can form galvanic coupling. In the worn area, the removed passive film is also known as depassivation. A negative shift of potential is observed due to the removal of the passive film. When the worn surface of Al alloys exposes on the electrolyte, it suffers a higher corrosion rate (wear accelerated corrosion) until another passive film formed, which is known as repassivation. Depassivation and repassivation

compete with each other through the whole tribocorrosion process. The degradation of Al alloys is the result of interaction between mechanical and chemical mechanism in tribocorrosion. The literature shows the interaction of wear-corrosion in the tribocorrosion of aluminum alloys. Panagopoulos et al. [23] studied the corrosive wear of 6082 aluminum alloy (Al–Si–Mg alloy) in 0.01 M NaCl solution, the friction coefficient decreased as the addition of sodium molybdate dihydrate inhibitor. Bouaeshi and Li [24] investigated the addition of Y_2O_3 in aluminum in order to improve the strength of aluminum alloys without decreasing the corrosion resistance, they found that the higher tribocorrosion resistance can be achieved by the finer microstructure. Chen et al. [25] studied tribocorrosion behavior of LY12 aluminum alloy in artificial seawater solution, the synergistic effect between wear and corrosion can accelerate material degradation.

1.3 Problem statement and research goals

As discussed in the previous section, two major corrosion modes of aluminum alloy include pitting corrosion and tribocorrosion, the former is related to the chemical breakdown while the latter is related to the mechanical breakdown of the passive film. These two modes of degradation will be the main focused of this thesis. In terms of pure corrosion, previous research shows that alloying addition (including both alloying type and concentration) greatly affect metastable pit initiation and growth rates. For example, small amounts of metallic elements (e.g. Sn, In, Hg, Ga, and Zn) are harmful to the corrosion of Al based alloys, because they could reduce the passive potential area and cause a negative movement in corrosion and pitting potentials [26]. The high current density and corrosion occurred on the surface, which led to the degradation of Al alloys. Other alloying elements such as Cu, Mo, Mn, W, Nb, Cr, Ta, V, and Zr improve corrosion resistance and decrease pitting susceptibility of Al by increasing the overpotential for anodic dissolution and decreasing metastable pit initiation and growth rates [27, 28]. In addition, when both corrosion and wear present at the surface, such as the case of tribocorrosion, alloying addition often increase wear resistance due to

precipitation strengthening, but compromise corrosion resistance due to galvanic coupling between precipitates and aluminum matrix, leading to poor tribocorrosion resistance.

1.3.1 Proposed strategy

To address the above problems, in this thesis, Al-based solid solutions are synthesized from non-equilibrium processing with an ultimate goal of simultaneously enhancing corrosion and tribocorrosion resistance of Al. Unlike precipitation strengthening, solid solution strengthening does not introduce chemical heterogeneity, hence is promising to achieve high resistance to both corrosion and wear. In addition, high alloying concentration can be achieved using non-equilibrium processing, such as pulse electrodeposition [29, 30], high-energy ball milling (HEBM), physical vapor deposition [31-34]. In this thesis, magnetron sputtering method is chosen to produce Al-base solid solutions. Fig. 1.8 shows the schematic of magnetron sputtering system. The sputtering target is bombarded by Ar plasma in magnetic field, the target atoms leave the target and condense on the substrate. The plasma and sputtering rate can control the composition and microstructure of deposited materials.

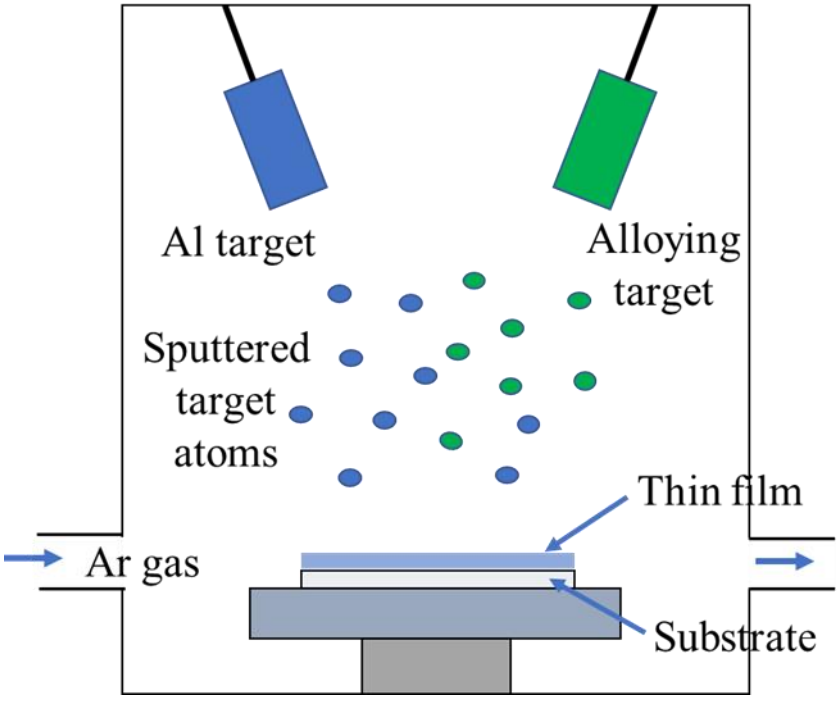

Figure 1.8 The schematic of dual sputtering targets system.

1.3.2 Alloy system selection

1.3.2.1 Al-Mn system

Among all common alloying element for Al, Mn is selected to form Al-Mn binary system in study 1 (chapter 2) and study 2 (chapter 3). Commercial Al-Mn alloys (e.g., Al3003) are widely used in the manufacture of foils, roof panels, cookware, and rigid containers due to their high ductility, good mechanical strength, and excellent corrosion resistance [35, 36]. In Al 3003 alloys, Mn is the main alloying element, and its chemical composition is between 1.0 ~ 1.5 wt.%. Nam et al. [37] found that the addition of Mn can enhance the tensile strength and corrosion resistance of Al alloys at the same time. Liu et al. [38] studied the role of second phase particles in pitting corrosion of 3003 Al alloy in NaCl solution, they found that the initiation of pits firstly occurred on Al substrate around the second phase particles, leading to form large pitting cavities due to the elimination of second phase particles. Yang et al. [39] investigated the corrosion behavior of 3003 aluminum alloy in flue gas condensate, they found that Cl^- and SO_4^{2-} can accelerate the corrosion of 3003 aluminum alloy greatly. In Fig. 1.9(a), it shows the ternary phase diagram of Al-Mn-O in air condition. The equilibrium of the ternary system plotted by Material Project was collected by DFT calculation at 0 K. In Al-Mn-O phase diagram, the formation energy of Al_2O_3 is -3.427, which is stable than that of Mn oxide (see Table 1.2). There are also some intermetallics forming at different formation energy, like AlMn, Al_6Mn, and $Al_{12}Mn$ etc. Pourbaix diagram of Al-Mn alloy systems plotted by Material Project is shown in Fig. 1.9(b). In Al-Mn alloy system, it can be seen that Al-Mn alloy remains stable at the potential below -1.8 V. It is passivated in the neutral pH, remaining MnO_2 and Al_2O_3 at higher potential while Mn^{2+} and Al_2O_3 at lower potential. At the potential higher than -1.5 V on both of acidic and alkaline environment, Al-Mn alloy is corroded while it remains Mn oxide at some certain potentials.

Beyond the commercial Al-Mn alloys, the results show that Al-Mn alloy can be produced by the electrodeposition under room temperature ionic liquids for the

preparation of nano-structured and amorphous alloys with excellent mechanical properties [40]. In Al-Mn solid solution (FCC phase), much higher corrosion and tribocorrosion resistance has been reported than commercial Al 3003. For example, Reffass et al. [41] studied the corrosion behavior of magnetron-sputtered Al_{1-x}-Mn_x in neutral saline solution, they found the pitting corrosion resistance of Al-Mn coatings increased with increasing Mn content. However, the formation mechanism of passive film of Al-Mn solid solution in corrosive environment is still unclear. Hesham et al. [42] studied the effects of Mn concentration on the tribocorrosion resistance of Al-Mn alloys, it was found that the depassivated area was quickly repassivated with faster repassivation kinetics at higher Mn content. However, it is still unknown that the effect of parameters of wearing test on depassivation-repassivation kinetics of passive film during tribocorrosion. Both of these questions will be answered in current studies.

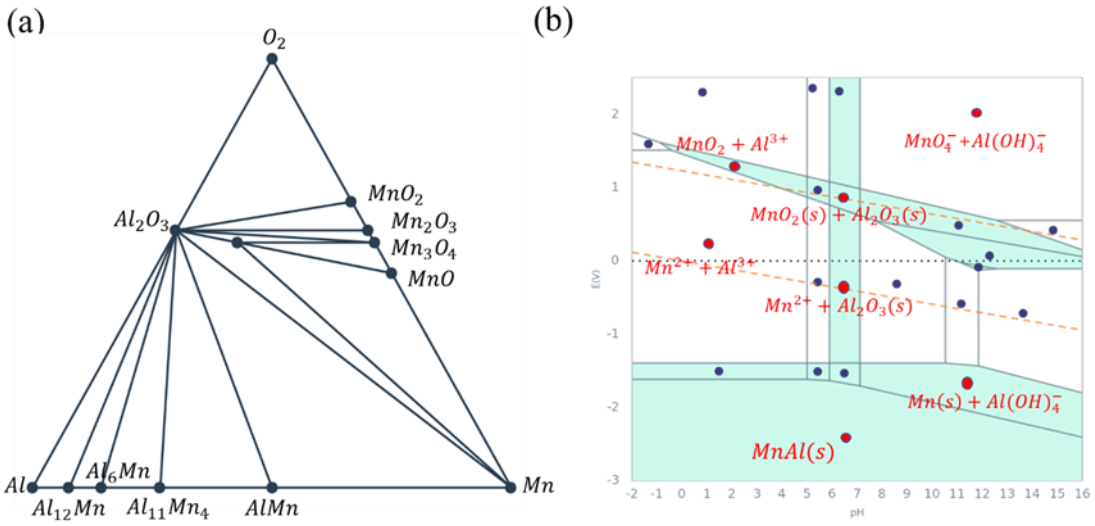

Figure 1.9 (a) The ternary phase diagram of Al-Mn-O at 0 K; (b) Pourbaix diagram of Al-Mn alloy at 25 ℃.

1.3.2.2 Al-Mn-Mo system

In addition to Mn, the effects of Mo on corrosion and tribocorrosion behavior of Al-Mn-Mo ternary system was studied in this thesis (chapter 4). Previous studies show that Mo is highly effective additives for improving the corrosion resistance of aluminum [34]. However, the equilibrium solubility of Mo in aluminum is very low.

Thus, in commercial Al alloys, the addition of Mo in Al alloys leads to the nucleation of pits at the precipitates and reduces the pitting resistance of Al alloys. In Fig. 1.10(a), it shows the ternary phase diagram of Al-Mo-O in air condition. The equilibrium of the ternary system plotted by Material Project was collected by DFT calculation at 0 K. In Al-Mo-O phase diagram, it is calculated that the formation energy of Al_2O_3 is stable than that of Mo oxide (-2.022 for MoO_2 and -1.925 for MoO_3). It must be noted that in the case of reaction with oxygen, it is easier to produce more stable alumina. Pourbaix diagram of Al-Mn-Mo alloy systems plotted by Material Project is shown in Fig. 1.10(b). In Al-Mn-Mo alloy system, the additional passivation area in Pourbaix diagram is due to the formation of Mo oxide compared to Pourbaix diagram of Al-Mn alloy. It can be seen that Mo is dissolved to MoO_4^{2-} at the potential higher than 1 V in the neutral pH, while remains Mo oxide and Mo below the potential of 1 V in the passive film.

When Al-Mo alloy was a single phase solid solution, stable passivity and excellent corrosion resistance of the passive film can be found on the surface of Al-Mo alloys in chloride containing solution. Tsuda et al. [29] electrodeposited Al-Mo alloys from the Lewis acidic $AlCl_3$-EtMeImCl chloride molten salt, the corrosion resistance of this alloy was significantly improved compared to other aluminum-transition metal alloys that have been electrodeposited to date. Although the addition of Mo to Al-Mn alloys may result in a ternary alloy with superior properties to those of Al-Mn and Al-Mo alloys, respectively, few research have described such studies. Tsuda et al. [43] reported the results of the electrodeposition of Al-Mn-Mo alloys that was produced in the 66.7–33.3 mol % $AlCl_3$-EtMeImCl molten salt as a preliminary investigation, they found that the pitting potential of Al-Mn-Mo alloys was improved in sodium chloride solution.

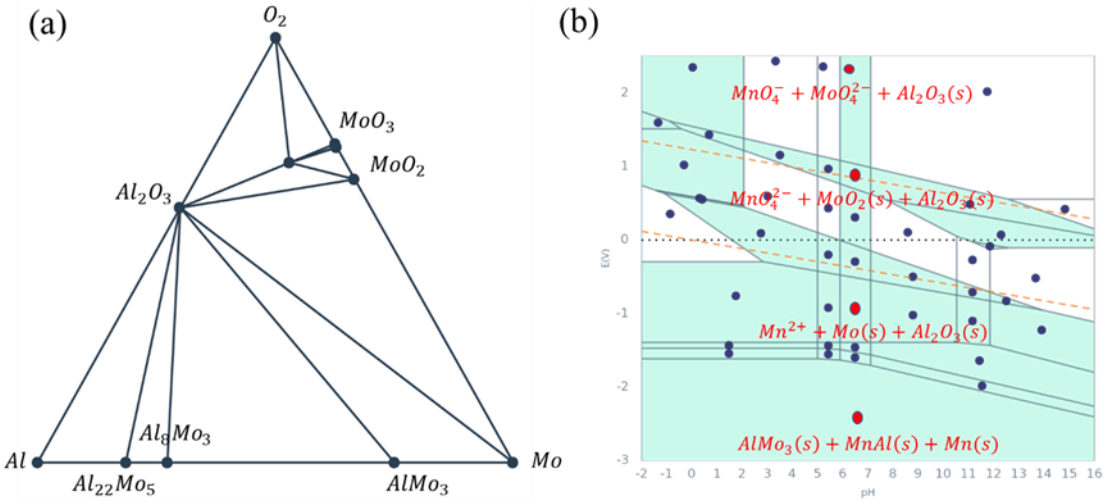

Figure 1.10 (a) The ternary phase diagram of Al-Mo-O at 0 K; (b) Pourbaix diagram of Al-Mn-Mo alloy at 25 ℃.

Table 1.2 The formation and decomposition energy of Al oxide, Mn oxide, and Mo oxide.

Compounds	Formation/Decomposition (energy/atom)
MnO_2	-1.806
MoO_3	-1.925
MnO	-1.979
Mn_2O_3	-2.014
MoO_2	-2.022
Mn_3O_4	-2.05
Al_2O_3	-3.427

1.4 Organization of the thesis

Study 1. Effect of wear conditions on the tribocorrosion behaviors of Al-Mn alloys (chapter 2)

The effect of scratching frequency on amorphous Al-Mn films was studied by changing the scratching frequency from 0.05 Hz to 1 Hz in simulated seawater. Scanning electron microscopy (SEM) and transmission electron microscopy (TEM)

were used to characterize the microstructure before and after tribocorrosion. Non-contact optical 3D profilometer was used to measure the morphology after tribocorrosion. The results show that the total tribocorrosion rate (including mechanical wear and chemical wear) increases with the increase of scratch frequency. Mechanical wear increases with the increase of scratch frequency, which is mainly related to the increase of friction coefficient and actual contact area. On the other hand, chemical wear increases with increasing scratch frequency, most likely due to faster passivation kinetics at lower frequencies. Cross-sectional TEM analysis shows that the disordered surface is mainly composed of alumina and manganese is completely absent.

Study 2. The formation mechanism of the passive layer of Al-Mn alloys (scope of chapter 3)

The effect of Mn on the corrosion of Al-Mn alloy was studied in 0.6 M NaCl aqueous solution. The electrochemical measurement, X-ray photoelectron spectroscopy and atomic probe tomography showed that the addition of Mn can improve the corrosion resistance of aluminum without taking part in surface oxidation. Selective dissolution of Mn is thought to increase the free volume of the metal/oxide interface, facilitating the formation of a denser and thinner oxide layer.

Study 3. Effect of Mo alloying element and concentration on the corrosion and tribocorrosion behaviors of Al-Mn-Mo alloys (scope of chapter 4)

The effect of Mo alloying concentration on the corrosion and tribocorrosion behavior of Al-Mn-Mo alloys was studied. The alloying concentration of Mo was from 0 at.% to 30at.%. The pitting potential and corrosion current density of Al-Mn-Mo increase with the increase of Mo content. The thickness of the passive film depends on the total alloy concentration, while the defect density depends on the individual concentration of the alloy. Among them, the corrosion resistance of $Al_{80}Mn_8Mo_{12}$ is higher due to the formation of a denser passivation film with fewer defects.

References

1. Fontana, M.G. and N.D. Greene, *Corrosion engineering*. 2d ed. McGraw-Hill series in materials science and engineering. 1978, New York: McGraw-Hill. xiii, 465 p.
2. Perez, N., *Electrochemistry and Corrosion Science*. 2016, Springer International Publishing : Imprint: Springer,: Cham. p. 1 online resource (XVII, 455 pages 180 illustrations, 174 illustrations in color.
3. http://resolver.tudelft.nl/uuid:63e16c47-997b-4ad1-b4c1-106fdd558d28.
4. Jones, D.A., *Principles and prevention of corrosion*. 2nd ed. 1996, Upper Saddle River, NJ: Prentice Hall. xvi, 572 p.
5. McCafferty, E., *Validation of corrosion rates measured by the Tafel extrapolation method.* Corrosion Science, 2005. **47**(12): p. 3202-3215.
6. Hamdy, A.S., E. El-Shenawy, and T. El-Bitar, *Electrochemical Impedance Spectroscopy Study of the Corrosion Behavior of Some Niobium Bearing Stainless Steels in 3.5% NaCl.* International Journal of Electrochemical Science, 2006. **1**(4): p. 171-180.
7. Barsoukov, E. and J.R. Macdonald, *Impedance spectroscopy : theory, experiment, and applications*. 2nd ed. 2005, Hoboken, N.J.: Wiley-Interscience. xvii, 595 p.
8. Landolt, D. and S. Mischler, *Tribocorrosion of passive metals and coatings*. Woodhead publishing in materials. 2011, Oxford ; Philadelphia: Woodhead. xxi, 554 p.
9. Espallargas, N. and S. Mischler, *Tribocorrosion behaviour of overlay welded Ni–Cr 625 alloy in sulphuric and nitric acids: Electrochemical and chemical effects.* Tribology International, 2010. **43**(7): p. 1209-1217.
10. Toh, W., et al., *Tribochemical Characterization and Tribocorrosive Behavior of CoCrMo Alloys: A Review.* Materials, 2017. **11**(1).
11. Barril, S., S. Mischler, and D. Landolt, *Electrochemical effects on the fretting corrosion behaviour of Ti6Al4V in 0.9% sodium chloride solution.* Wear, 2005.

259(1-6): p. 282-291.

12. Davis, J.R., Associates, and A.S.M.I.H. Committee, *Aluminum and aluminum alloys*. ASM specialty handbook. 1993, Materials Park, OH: ASM International.
13. Szklarska-Smialowska, Z., *Pitting corrosion of aluminum.* Corrosion Science, 1999. **41**(9): p. 1743-1767.
14. Hagyard, T. and J.R. Williams, *Potential of aluminium in aqueous chloride solutions. Part 1.* Transactions of the Faraday Society, 1961. **57**.
15. Muller, I.L. and J.R. Galvele, *Pitting potential of high purity binary aluminium alloys—I. Al Cu alloys. Pitting and intergranular corrosion.* Corrosion Science, 1977. **17**(3): p. 179-193.
16. Bond, A.P., et al., *Microsegregation and the Tendency for Pitting Corrosion in High-Purity Aluminum.* Journal of The Electrochemical Society, 1966. **113**(8).
17. Vargel, C., *Preface to the Original French Edition*, in *Corrosion of Aluminium*. 2004. p. xiii-xiv.
18. Rehim, S.S.A., H.H. Hassan, and M.A. Amin, *Corrosion and corrosion inhibition of Al and some alloys in sulphate solutions containing halide ions investigated by an impedance technique.* Applied Surface Science, 2002. **187**(3-4): p. 279-290.
19. Mazhar, A.A., W.A. Badawy, and M.M. Abou-Romia, *Impedance studies of corrosion resistance of aluminium in chloride media.* Surface and Coatings Technology, 1986. **29**(4): p. 335-345.
20. Natishan, P.M. and W.E. O'Grady, *Chloride Ion Interactions with Oxide-Covered Aluminum Leading to Pitting Corrosion: A Review.* Journal of the Electrochemical Society, 2014. **161**(9): p. C421-C432.
21. Ketcham, S.J. and F.H. Haynie, *Electrochemical Behavior of Aluminum Alloys Susceptible to Intergranular Corrosion. I. Effect of Cooling Elate on Structure And Electrochemical Behavior in 2024 Aluminum Alloy.* Corrosion, 1963. **19**(7): p. 242t-246t.
22. El-Amoush, A.S., *Intergranular corrosion behavior of the 7075-T6 aluminum*

alloy under different annealing conditions. Materials Chemistry and Physics, 2011. **126**(3): p. 607-613.

23. Panagopoulos, C.N., E.P. Georgiou, and A.G. Gavras, *Corrosion and wear of 6082 aluminum alloy.* Tribology International, 2009. **42**(6): p. 886-889.
24. Bouaeshi, W.B. and D.Y. Li, *Effects Of Y2O3 addition on microstructure, mechanical properties, electrochemical behavior, and resistance to corrosive wear of aluminum.* Tribology International, 2007. **40**(2): p. 188-199.
25. Jun, C., P. Bingli, and Q.A. Li, *Tribocorrosion Behavior of LY12 Aluminum Alloy in Artificial Seawater Solution.* Tribology Transactions, 2020.
26. Gudic, S., I. Smoljko, and M. Kliskic, *The effect of small addition of tin and indium on the corrosion behavior of aluminium in chloride solution.* Journal of Alloys and Compounds, 2010. **505**(1): p. 54-63.
27. Kim, Y. and R.G. Buchheit, *A characterization of the inhibiting effect of Cu on metastable pitting in dilute Al-Cu solid solution alloys.* Electrochimica Acta, 2007. **52**(7): p. 2437-2446.
28. Principe, E.L., B.A. Shaw, and G.D. Davis, *Role of oxide/metal interface in corrosion resistance: Al-W and Al-Mo systems.* Corrosion, 2003. **59**(4): p. 295-313.
29. Tsuda, T., C.L. Hussey, and G.R. Stafford, *Electrodeposition of Al-Mo alloys from the Lewis acidic aluminum chloride-1-ethyl-3-methylimidazolium chloride molten salt.* Journal of the Electrochemical Society, 2004. **151**(6): p. C379-C384.
30. Tsuda, T. and C.L. Hussey, *Electrochemistry of vanadium(II) and the electrodeposition of aluminum-vanadium alloys in the aluminum chloride-1-ethyl-3-methylimidazolium chloride molten salt.* Journal of Mining and Metallurgy, Section B: Metallurgy, 2003. **39**(1-2): p. 3-22.
31. Sanchette, F. and A. Billard, *Main features of magnetron sputtered aluminium–transition metal alloy coatings.* Surface and Coatings Technology, 2001. **142-144**: p. 218-224.
32. Moshier, W.C., et al., *Corrosion Behavior of Aluminum-Molybdenum Alloys in*

Chloride Solutions. Journal of the Electrochemical Society, 1987. **134**(11): p. 2677-2684.

33. Shaw, B.A., et al., *The Influence of Tungsten Alloying Additions on the Passivity of Aluminum.* Journal of The Electrochemical Society, 2019. **138**(11): p. 3288-3295.
34. Frankel, G.S., et al., *Pitting of Sputtered Aluminum Alloy Thin Films.* Journal of The Electrochemical Society, 2019. **136**(4): p. 1243-1244.
35. Suryanarayana, C. and R. Sundaresan, *Metastable phases in mechanically alloyed Al Mn powder mixtures.* Materials Science and Engineering: A, 1991. **131**(2): p. 237-242.
36. Nam, S.W. and D.H. Lee, *The effect of Mn on the mechanical behavior of Al alloys.* Metals and Materials, 2000. **6**(1): p. 13-16.
37. Nam, S.W. and D.H. Lee, *The effect of Mn on the mechanical behavior of Al alloys.* Metals and Materials-Korea, 2000. **6**(1): p. 13-16.
38. Liu, Y. and Y.F. Cheng, *Role of second phase particles in pitting corrosion of 3003 Al alloy in NaCl solution.* Materials and Corrosion, 2010. **61**(3): p. 211-217.
39. Yang, H.J., et al., *Investigation of corrosion behavior of 3003 aluminum alloy in flue gas condensate.* Materials and Corrosion, 2017. **68**(6): p. 664-673.
40. Cai, W.J. and C.A. Schuh, *Tuning nanoscale grain size distribution in multilayered Al-Mn alloys.* Scripta Materialia, 2012. **66**(3-4): p. 194-197.
41. Reffass, M., et al., *Corrosion behaviour of magnetron-sputtered Al1-x-Mn-x coatings in neutral saline solution.* Corrosion Science, 2010. **52**(11): p. 3615-3623.
42. Mraied, H. and W.J. Cai, *The effects of Mn concentration on the tribocorrosion resistance of Al-Mn alloys.* Wear, 2017. **380-381**: p. 191-202.
43. Tsuda, T., C.L. Hussey, and G.R. Stafford, *Electrodeposition of Al-Mo-Mn ternary alloys from the Lewis acidic AlCl3-EtMeImCl molten salt.* Journal of the Electrochemical Society, 2005. **152**(9): p. C620-C625.

Chapter 2:

Effect of Scratching Frequency on the Tribocorrosion Resistance of Al-Mn Amorphous Thin Films

Jia Chen[a,b], Wenjun Cai[b,*]

a Department of Mechanical Engineering, University of South Florida, Tampa, FL 33620, USA

b Department of Materials Science and Engineering, Virginia Polytechnic Institute and State University, Blacksburg, VA 24060, USA

*Corresponding author E-mail address: caiw@vt.edu

Declarations of interest: none

*This chapter has been adapted from a **published** manuscript by Jia Chen and Wenjun Cai from the following reference:*

Jia Chen, and Wenjun Cai. "Effect of Scratching Frequency on the Tribocorrosion Resistance of Al-Mn Amorphous Thin Films." Wear, vol. 426, no. Pb, 2019, pp. 1457–1465.

Reprinted with permission from the Elsevier.

2.1 Abstract

Amorphous metallic thin films show great promise for applications where mechanical and chemical attack coexist due to their excellent wear, corrosion, and tribocorrosion resistance. In this research, the effect of scratching frequency on amorphous Al-Mn thin film were studied in simulated seawater by varying the scratching frequency from 0.05 to 1 Hz in reciprocal motion. Scanning electron microscopy (SEM) and transmission electron microscopy (TEM) were applied to characterize the microstructure before and after tribocorrosion testing. Post-tribocorrosion topography measurement was performed using non-contact optical 3D profilometer. It was found that the total tribocorrosion rate, including both mechanical and chemical wear, increased with increasing scratching frequency. Mechanical wear increased with scratching frequency, mostly related to an increment of coefficient of friction and real contact area. On the other hand, chemical wear tends to increase with scratching frequency, most likely due to faster repassivation kinetics at lower frequency. Cross-sectional TEM analysis shows that the disordered surface layer primarily consists of aluminum oxide where manganese is completely absent.

2.2 Introduction

The area of metal development has been characterized by some gradual changes over the last few decades. The focus has shifted from mainly emphasizing high strength in the past, to achieve a combination of high strength and ductility nowadays [1-4]. Looking into the future, various critical applications require not only a strong and tough metal, but one that is robust and reliable when interacting with some very extreme environment [5, 6]. For example, to develop new pipeline materials to transport oil and gas from unconventional reserves in harsh environment [7, 8]; to build the next generation nuclear power plants with strong and corrosion resistant materials for improved safety and longer lifetime [9, 10]; to develop advanced implantable medical devices with reliable metal interconnect in physiological environment [11, 12]; and to fabricate high capacity fast charging batteries with electrodes that can undergo millions

of charging and uncharging cycles in corrosive electrolyte [13, 14]. These extreme environments are testing the limits of most engineering metals and challenging the current understanding of the underlying degradation mechanism. In most cases. the performance of metals deteriorates dramatically due to the combined mechanical (wear) and chemical (corrosion) attack at the surface [15]. Such material degradation caused by the synergistic effects of wear and corrosion, is often referred as tribocorrosion. Thus, designing tribocorrosion resistant metals and obtaining a fundamental understanding of the associated degradation mechanism is essential for a variety of current and future technologies.

Tribocorrosion is especially prominent for passive metals such as aluminum (Al) and its alloys, where mechanical wear at the surface easily destroys the protective passive film at the contacting asperities and lead to rapid localized corrosion and early failure [16-18]. Unfortunately, optimizing tribocorrosion resistance of Al alloys remains a challenge since there is typically a trade-off between their wear and corrosion resistance [19]. For example, enhanced wear resistance in most precipitation-hardened Al alloys was often achieved at the expanse of sacrificed corrosion resistance, mainly due to micro-galvanic coupling between the matrix and precipitates [20-23]. Our recent study [19, 24] shows that alloying aluminum with appropriate transition metals in supersaturated solid solution simultaneously improve the corrosion and wear resistance of Al. Specifically, it was found that increasing the Mn concentration improved the protectiveness of the passive film, increased the hardness, and accelerated the repassivation kinetics of Al.

The current work is an extension of our previous study [19] with a focus on investigating the effect of scratching frequency on the tribocorrosion resistance of Al-Mn. Extensive work has been performed on evaluating the tribocorrosion behavior of metals so far, but few focused on the effect of scratching speed or frequency. For example, Salasi et al. [25] studied the effect of tangential speed on the triboelectrochemical behavior of 316 L stainless steel. It was shown that the passive film had less time to repassivate at higher tangential speed, which also led to a higher

current rate. Li et al. [26] studied the depassivation-repassivation behavior of a CoCrMo alloy and found that the rubbing frequency significantly affects the depassivation rate. A similar observation was also reported by Stemp et al. [27]. Mischler et al. [28] showed that the anodic current over the wear track of 316 stainless steel and Ti6Al4V increased linearly with sliding distance and sliding frequency. While scratching speed and frequency were sometimes used interchangeably during linear reciprocal motion wear in some studies, here we will use scratching frequency instead of speed. This is because the speed of the tip is not always a constant. During linear reciprocal wear, the speed of the scratching tip has to quickly come to zero at the end of the wear track where the tip changes moving direction. The specific goals of this research include, 1) to identify the effect of scratching frequency on the tribocorrosion resistance, 2) to characterize the atomistic scale microstructure and composition after tribocorrosion, and 3) to understand the effect of scratching frequency on the depassivation and repassivation kinetics of amorphous Al-Mn alloy.

2.3 Materials and methods

2.3.1 Materials synthesis and characterization

Amorphous Al-Mn thin film with ~ 21.6 at% Mn (hereafter referred as Al-Mn thin film for simplicity) was deposited on (100) Si substrate using a CRC-100 magnetron sputtering machine (Torr International, New York, USA) under 80W power and 5 mTorr argon atmosphere. The thickness of the film was ~ 1.1 μm, measured by a Dektak D150 profilometer (Veeco, New York, USA). Surface morphology of the tested samples was characterized by an optical 3D profilometer (Wyko® NT9100 optical profiling system, Veeco, New York, USA). Scanning electron microscopy (SEM, SU-70, Hitachi, California, USA) and transmission electron microscopy (TEM, Tecani F20, Oregon, USA) was used to characterize the surface morphology and microstructure of the samples before and after tribocorrosion test. TEM sample of the as-deposited film was prepared by directly depositing Al-Mn on continuous carbon TEM grid for 10 – 15 min. Energy-dispersive x-ray spectroscopy (EDS, EDAX-Phoenix, New Jersey, USA) was

used to characterize the chemical composition of the samples post to tribocorrosion tests under various scratching frequencies. Cross-sectional TEM analysis of the wear track was performed using TEM samples prepared by the focused ion beam (FIB, Quanta 200 3D, Oregon, USA) lift-out technique on selected samples. During the TEM sample preparation by FIB, the corroded sample surface was protected with Pt layers from Ga ion damage. The Pt layer deposition contains two steps: an electron beam deposition of Pt of ~30 nm was performed first, followed by an ion beam deposition of Pt of ~1–2 µm. The two step-deposition ensures minimal Ga ion damage from the sample milling steps afterwards. This is indeed confirmed by STEM-EDS analysis of the cross-sectional TEM samples (results not shown here).

2.3.2 Tribocorrosion test

Fig. 2.1 shows the schematic set-up of the tribocorrosion system, where a custom-made corrosion cell (Teflon) was attached to a UMT tribometer (Bruker™ Universal Mechanical Tester) stage and leak-proofed by an O-ring. A three-electrode setup comprised of the thin film as the working electrode (WE), activated titanium mesh and 1M KCl Ag/AgCl electrode as the counter (CE) and reference electrode (RE) respectively, was connected to a potentiostat/galvanostat/zero resistance ammeter (Gamry Reference 600™ system).

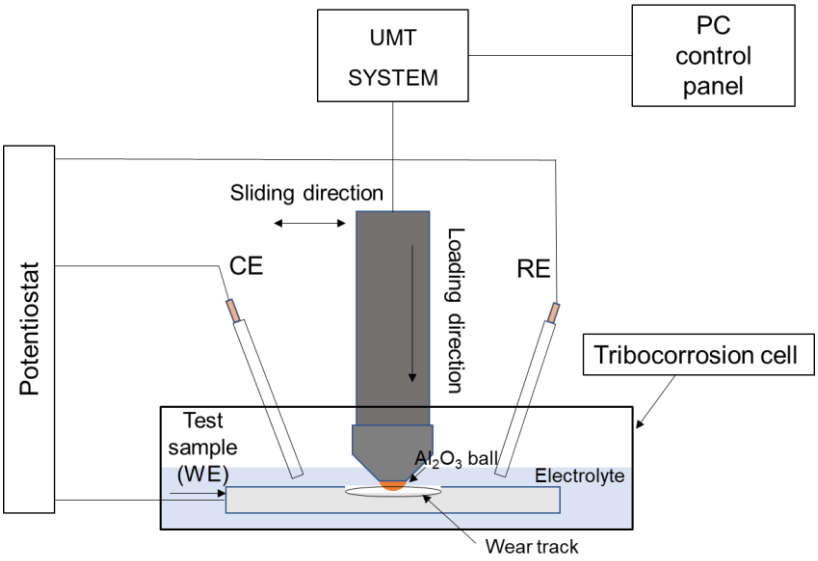

Figure 2.1 Schematic set-up of the tribocorrosion system.

To prepare the WE, an exposed test area of ~ 1×1.5 cm^2 was prepared on each sample using a protective stop-off lacquer. A ~ 5 cm long, 1 mm diameter insulated copper wire was stripped off ~ 5 mm on both ends. where one end was electronically connected to the back of the sample. Special care was taken to ensure that the back of the sample was completely covered by the protective lacquer, including the connection with the copper wire. After drying off the lacquer in a chemical hood for 24 h, the sample was glued to the sample stage using superglue. The electrolyte used was ~40 ml of 0.6 M NaCl aqueous solution (pH ~ 6.4 ± 0.3), open to air. An alumina ball (Al_2O_3, 4 mm diameter) was used as the counter body for the tribocorrosion test. Each test was performed by applying a 0.5 N normal force, 5 mm scratch length, at various scratching frequency (0.05 Hz, 0.1 Hz, 0.5 Hz and 1 Hz) in linear reciprocal motion at ambient temperature (27 ± 2 °C). Based on our previous study [19], an anodic potential of 200 mV vs. Ag/AgCl above open circuit potential (E_{oc}) was applied during tribocorrosion. 200 mV was selected so that it is within the passive region yet well below the pitting potential [19]. Prior to each tribocorrosion test, the open circuit potential (E_{oc}) was first stabilized for 40 min. Then the tribocorrosion test was performed for 5 min by applying a normal load of 0.5 N from the alumina ball at the anodic potential (i.e. 200 mV above E_{oc}). Once finished, the indenter ball was removed, and the sample remained in electrolyte for another 5 min. A new alumina ball was always used after each test to minimize contamination. After the tribocorrosion test, the wear track dimension was measured by Dektak D150 profilometer and the cross-section area of the wear track was calculated by trapezoidal numerical integration method. The tribocorrosion rate was calculated by dividing the total materials loss in volume by the total scratching distance. All the test results reported here were averaged from at least three repeated tests.

2.4 Results and discussion

2.4.1 Microstructure of as-deposited films

The microstructure of the as-deposited Al-Mn films was characterized by SEM

and high-resolution TEM, as shown in Fig. 2.2. It can be seen from Fig. 2.2(a) that the surface of the thin film appears to be smooth and featureless, indicating the formation of ultrafine microstructure. High-resolution TEM analysis confirms the absence of long-range order of the deposit (Fig. 2.2(b)), together with the presence of a diffuse ring in the selected area diffraction (SAD) pattern (Fig. 2.2(b) inset), suggesting the formation of an amorphous solid solution of Al-Mn, well exceeding the equilibrium solubility of Mn in Al (typically less than 0.01 wt.% Mn is completely dissolved in Al at low temperature). Such observations were in good agreement with our prior work [19] and those from electrodeposited Al-Mn alloy [29, 30].

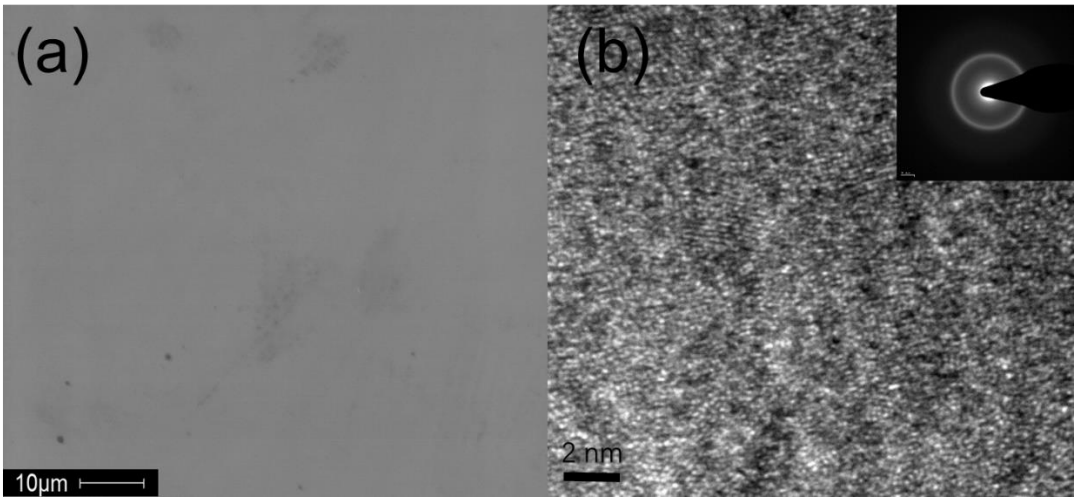

Figure 2.2 (a) Typical surface SEM and (b) bright-field high resolution TEM image of as-deposited Al-21.6 at% Mn. Inset in (b) shows the selected area diffraction (SAD) of image (b).

2.4.2 Current evolution during tribocorrosion test

Fig. 2.3(a) shows the current evolution vs. time during the tribocorrosion tests at various scratching frequency. The current remains close to zero in the majority of the time before and after the tribocorrosion tests. Thus only ~ 220 s of the current prior to and after tribocorrosion tests were plotted in Fig. 2.3(a) for easy visualization. It can be seen that in all cases, a significant current rise was observed during tribocorrosion (from ~ 1220 to 1520 s) test, which is a clear indication that mechanical wear accelerate corrosion. It is also noted that a higher current is observed at high scratching frequency.

Under all frequencies investigated here, there is a significant current fluctuation during tribocorrosion test. The magnitude of such fluctuation tends to increase with increasing scratching frequency. It is also noted that at frequency of 0.5 and 1 Hz, the current drops back to zero before the end of test. This is due to the much higher total scratching distance at higher frequencies, where the Al-Mn thin film were completed removed and the substrate Si were exposed before the end of the test (as confirmed by EDS mapping in the next section).

Since various scratching frequency leads to various wear track area (as detailed in the next section), the current density rather than current, offers a better measurement of averaged charge transfer rate per unit area. Fig. 2.3(b) shows the current density at various scratching frequency. The current density was calculated by normalizing the recorded current at each point by the total area of the wear track of each sample (instead of the exposed area of the whole sample). Since the current of unworn area is close to zero, only the depassivated area, i.e. the wear track area, was used for this conversion. It is noted here since wear track dimensions were measured at the end of each tribocorrosion test, so the current density calculated do not reflect an instantaneous value (where the current should be normalized by the instantaneous wear track area at each point in time). This simplification clearly overestimates the wear track dimensions near the beginning of the test, thus underestimating the current density. Fig. 2.3(b) shows that while the anodic current in the wear track increased monotonically with frequency, it however deviates from linearity.

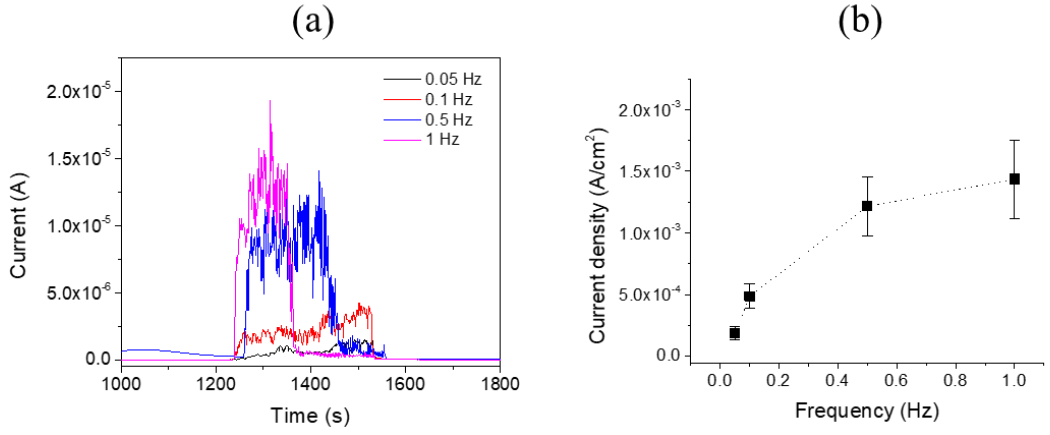

Figure 2.3 Evolution of (a) current over time, and (b) average current density vs. frequency of Al-Mn thin film at scratching frequency of 0.05 - 1 Hz under 0.5 N load at 200 mV above E_{oc} in 0.6M NaCl aqueous solution.

2.4.3 Wear and friction during tribocorrosion test

Figure 2.4 shows the typical 3D optical images of all samples after the tribocorrosion test. It can be seen that both the depth and width of the scratched area increased with increasing scratching frequency. The depth of the scratched area under 0.05 Hz and 0.1 Hz condition is about 300 nm and 580 nm respectively. Under 1 Hz condition, the thin film is completely removed by the Al2O3 ball at the end of the test, where the wear depth is ~ 1.1 μm, corresponding to the total film thickness.

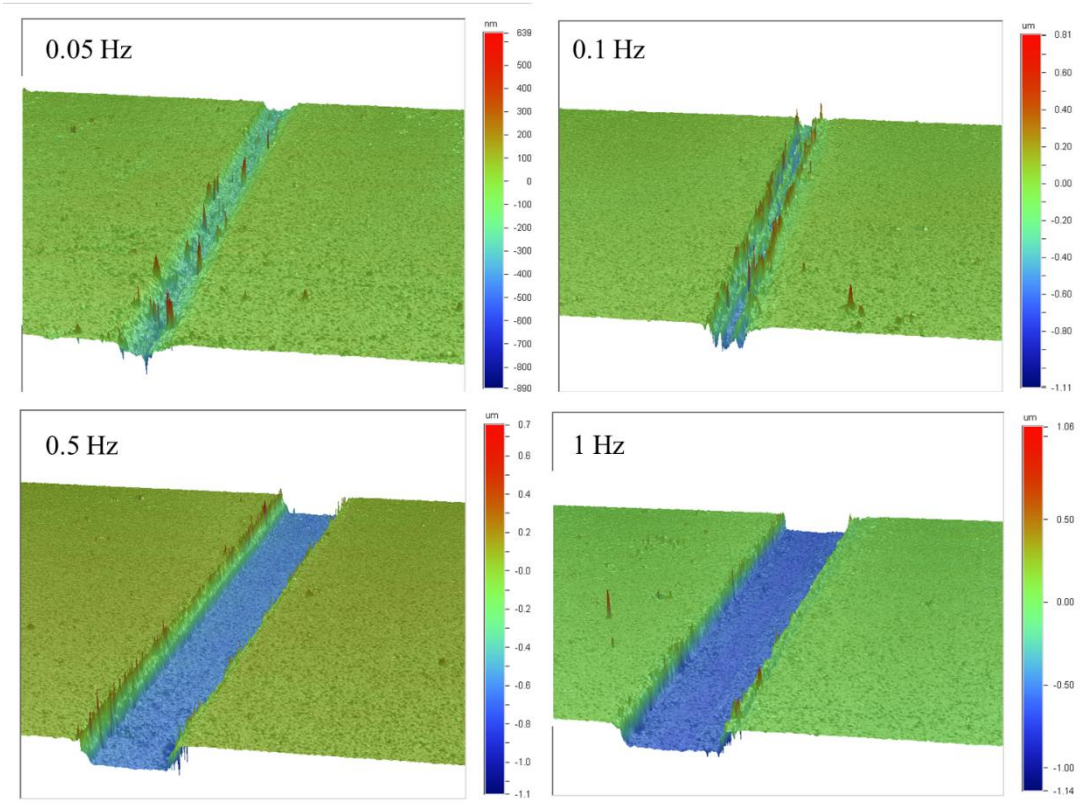

Figure 2.4 3D optical profilometer images of wear tracks of Al-Mn thin film at various scratching frequency. Each image was color coded according to the legend bar on the right. The dimension of each figure is 1.1 mm (horizontal) × 0.83 mm (vertical). (For interpretation of the references to color in this figure legend, the reader is referred to the web version of this article.)

To quantify the tribocorrosion resistance under different scratching frequency, the width and depth of the wear track is measured, as shown in Fig. 2.5, and summarized in Table 2.1. From Fig. 2.5(a), it can be seen that the width of wear track increased from ~ 44 to 125 μm as scratching frequency raised from 0.05 to 1 Hz. The tribocorrosion rate of all samples were plotted in Fig. 2.5(c) and summarized in Table 2.1. It is noted here that at lower frequencies (0.05 and 0.1 Hz), the wear volume was calculated by multiplying the measured wear track width and depth. At higher frequencies (0.5 and 1 Hz), due to the complete removal of Al-Mn film prior to the end of the test, the wear volume of Al-Mn was calculated by multiplying the measured wear track width and the as-deposited thin film thickness (1.1 μm). It can be seen that the tribocorrosion rate increased monotonically with scratching frequency. Such result is similar to the past investigations of 304L SS, Zr-702, Zircaloy-4 and Ti-grade2 [31].

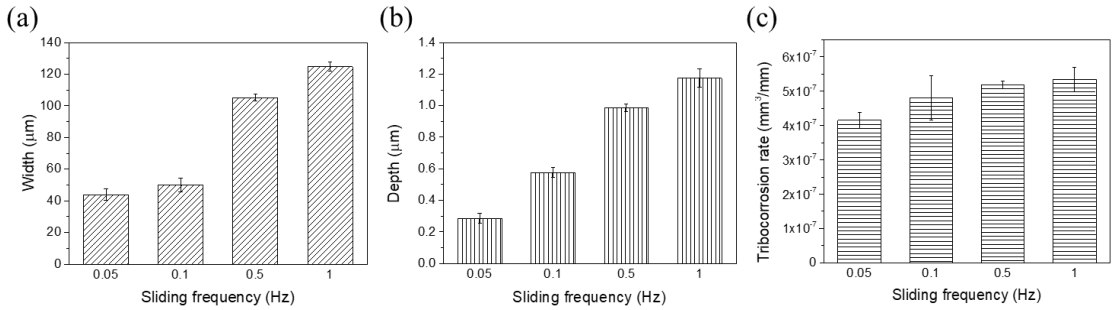

Figure 2.5 Summary of average (a) wear track width, (b) depth, and (c) tribocorrosion rate of each sample sets at various scratching frequency. Error bar represents one standard deviation.

Table 2.1 Summary of tribocorrosion test results at various scratching frequency.

Sample sets	Speed (mm/s)	Scratch length (mm)	Frequency (Hz)	Wear track width (μm)	Tribocorrosion rate ($\times 10^{-8}$ mm^3/mm)	COF
1	0.5	5	0.05	73.81 ± 3.55	9.48 ± 0.50	0.46 ± 0.01
2	1	5	0.1	89.27 ± 2.00	13.3 ± 1.70	0.52 ± 0.02
3	5	5	0.5	128.67 ± 9.14	24.8 ± 1.40	0.55 ± 0.02
4	10	5	1	142.83 ± 1.92	27.2 ± 0.95	0.56 ± 0.01

The evolution of coefficient of friction ($COF = F_f/F_n$, where F_f and F_n is the frictional and normal forces respectively) of all samples is shown in Fig. 2.6. After the

running-in period of ~ 20-40 s, a steady-state COF is reached in all samples. Note here that for high frequency tests (0.5 and 1 Hz), COF data were only plotted before the Al-Mn thin was completely removed. It can be seen that all samples exhibit typical stick-slip scratching during the tests, where the COF fluctuates quasi-periodically between a high (static friction) and low (scratching friction) value. The average COF increased from 0.46 to 0.56 as frequency increased from 0.05 to 1 Hz. The COF value is mainly related to the surface layer structures, surface roughness and other lubricated condition [32]. In the present work, since the same normal load is applied, the change of COF can be directly related to a change of frictional force F_f. During severe abrasive wear, assuming a simplified adhesion theory of friction, F_f can be estimated from $F_f = \tau \times A_{real}$ [33, 34], where τ is the shear stress of the surface layer, and A_{real} is the real contact area. Assuming that the surface layer of all samples has a similar composition (due to the same alloy composition and imposed anodic potential), hence similar τ, the increase of F_f is then an indication of increased Areal as frequency increases. This is indeed in agreement with the experimental measurement. For example, Fig. 2.4 shows that a larger number of contacting asperities were observed over similar wear track area at 0.1 Hz than that at 0.05 Hz.

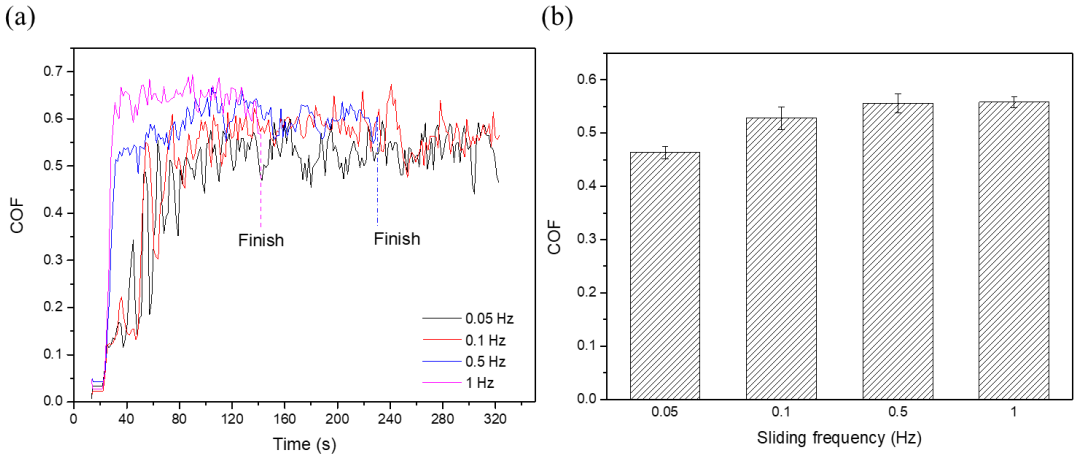

Figure 2.6 (a) Evolution of coefficient of friction (COF) vs time, and (b) average COF measured from tribocorrosion test under various scratching frequency. Error bar represents one standard deviation.

2.4.4 Wear-corrosion synergy

Results in Section 2.4.3 indicates that the total tribocorrosion rate increases with scratching frequency. Since tribocorrosion rate was calculated as the total material loss divided by the total scratching distance (hence eliminating the effect of higher scratching distance at higher frequency), the change in tribocorrosion rate indicates that a higher material loss rate per unit length occurred at higher frequency. To understand the origin of such trend, the total material loss (V_{tot}) can be decoupled into chemical and mechanical wear [35, 36]. The amount of chemical material loss (V_{chem}) could be calculated by Faraday's law as $V_{chem} = \frac{QM}{nF\rho}$ [37-39], where Q is the total charge (including both Al and Mn dissolution) transferred during tribocorrosion (average anodic current multiply by the time) under imposed anodic polarization, M is the molar mass (≈ 32.88 g/mol for Al-20 at.% Mn alloy), n is the number of electrons transferred per ion (n = 2.79 for Al-20 at.% Mn alloy). F is the Faraday's constant (96,500 C/mol), and ρ is the alloy density (≈ 3.7 g/cm^3). Then the mechanical wear (V_{mech}) can be calculated as $V_{mech} = V_{tot} - V_{chem}$ [35, 36, 40]. The results are shown in Fig. 2.7.

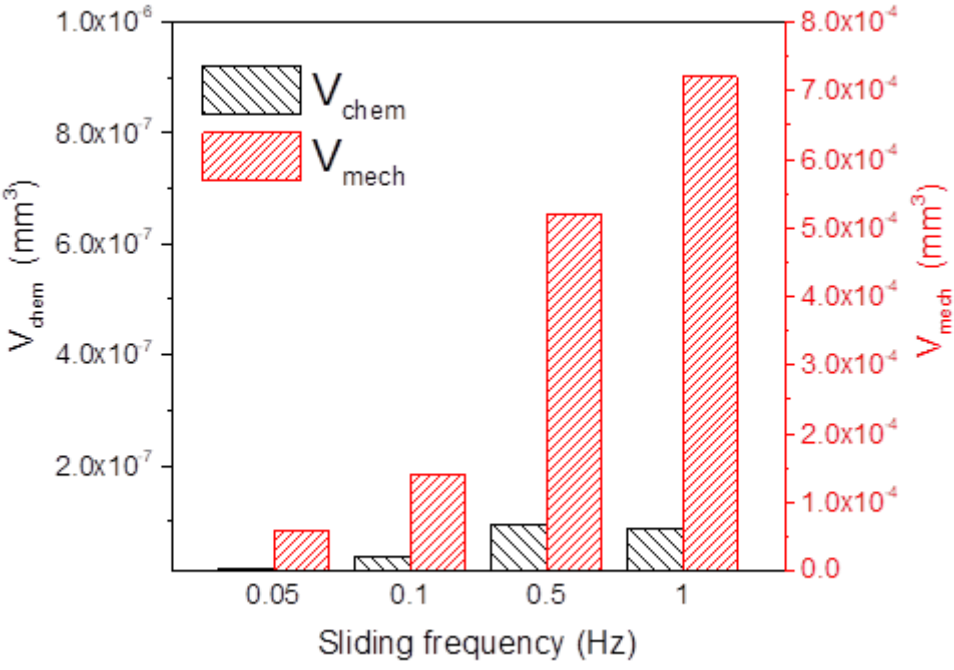

Figure 2.7 Summary of chemical and mechanical wear of all samples.

It can be seen that, with the increment of scratching frequency, both chemical and mechanical effect increased, with the exception of V_{chem} at 1 Hz. However, since the thin film is completely removed before the end of test at 1 Hz, it is thus not surprising that a smaller total V_{chem} is observed than that at 0.5 Hz. At 1 Hz condition, there is a huge difference between V_{chem} and V_{mech}, which means the mechanical wear is dominating the tribocorrosion process and the effect of corrosion could be minimal. This is not surprising, as higher scratching frequency leads to higher depassivation rate, thus less material loss due to corrosion per unit time. This trend is also in agreement with the increasing COF and A_{real} with frequency, since wear rate tend to increase with friction under similar wear mode. The increment of V_{chem} with frequency may be related to the different repassivation kinetics. At lower scratching frequency, the wear track (depassivated area) has enough time to repassivate during each pass of scratch, thus a much lower repassivation current is required to maintain the same imposed anodic potential. On the other hand, at higher frequency, the fast scratching rate leaves little time for repassivation. Hence the current on the wear track remains high throughout the test.

Fig. 2.8 schematically illustrates such two scenarios. At low frequency, the current density periodically fluctuates between a local high value (right after contacting with the counter body) and a low value (when the surface completely repairs itself). The period of one such cycle corresponds to the time that the unit area needs to completely repair itself. Take the 0.05 Hz test as an example, the current density profile in Fig. 2.3(b) agrees well with such hypothesis and one period is ~ 120 s. Note that at f = 0.05 Hz, the counter body scratches a certain location on the wear track every ~10 s. Such discrepancy suggests that during the apparent contact by the counter body each time, the local real contact asperities (hence location of passive film removal) is different most of the time. At higher frequency, the depassivated area has little time to completely repair, hence the current density remains high with a large fluctuation magnitude. This is indeed observed at 0.5 and 1 Hz tests, as shown in Fig. 2.3(b). The current density ratio of j_2/j_1 can thus be considered as the percentage of depassivated area per unit area.

This percentage is ~ 0.70, 0.57, and 0.63 for f = 0.1, 0.5, and 1 Hz respectively.

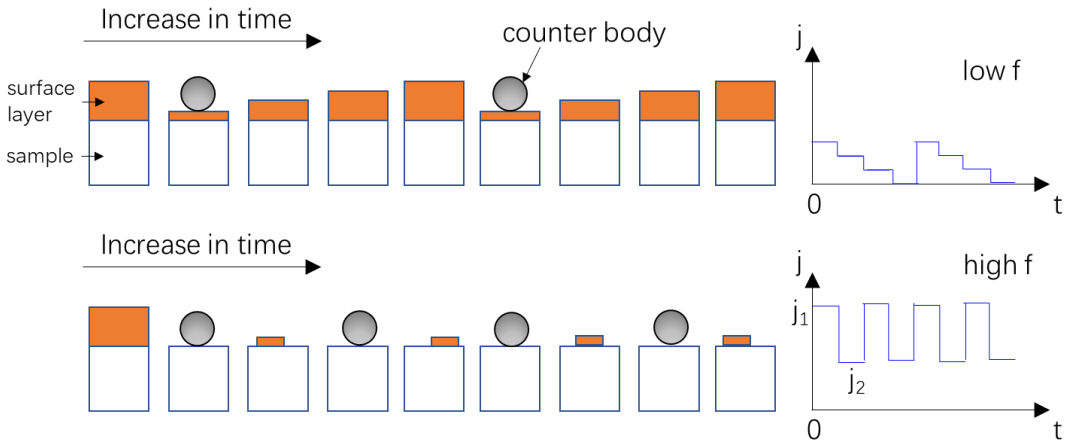

Figure 2.8 Schematic illustration of surface layer evolution and current density vs. time profile during low (top) and high (bottom) frequency tribocorrosion test. The plotted sample in the schematic represent a unit area of the cross-sectional sample.

2.4.5 Post-test surface and cross-section characterization

Fig. 2.9 shows the surface morphology and composition of the wear track after tribocorrosion test at various scratching frequency. The wear track was characterized by scratch grooves and patches of wear debris. The average composition of the wear track of all samples is shown in Table 2.2. It can be seen that a significant amount of oxygen can be detected from the wear track.

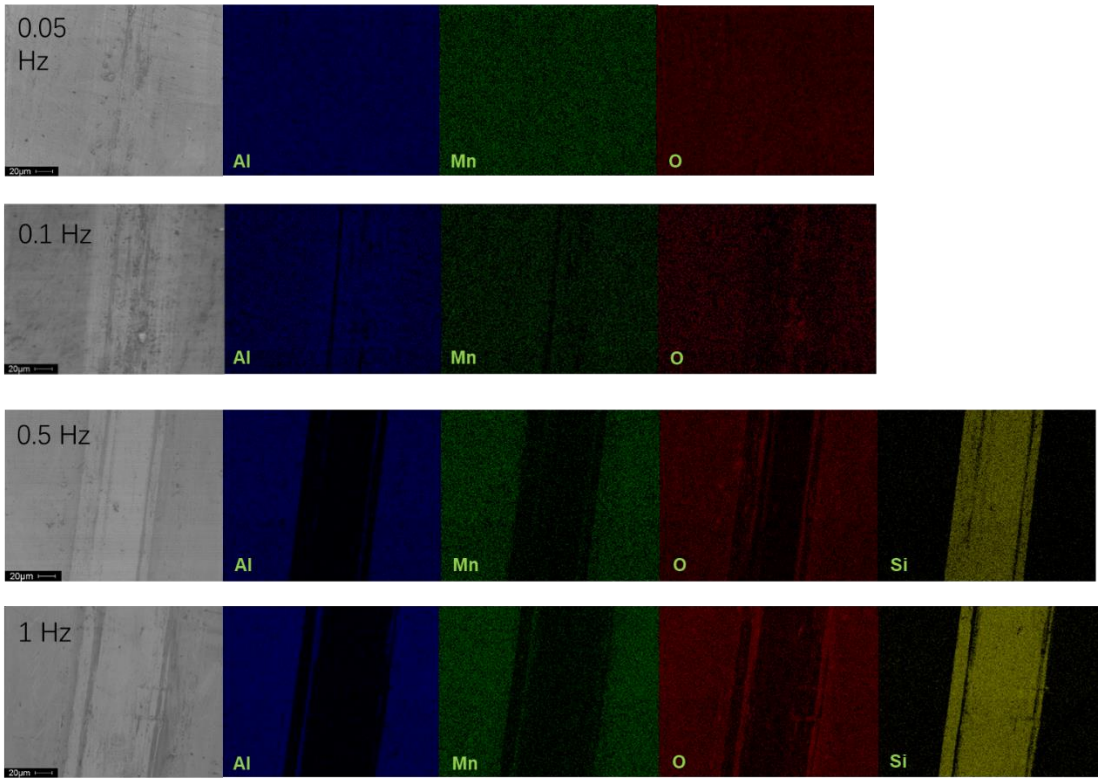

Figure 2.9 Summary of surface SEM images and corresponding EDS element mappings (of Al, Mn, O, and Si) after tribocorrosion tests at various scratching frequency. The scale bar is 20 μm.

Table 2.2 Average element concentration measured on wear track for samples after tribocorrosion test at various scratching frequency. The EDS resolution is ~1 at.%.

Frequency	Element			
	Al (at.%)	Mn (at.%)	O (at.%)	Si (at.%)
0.05 Hz	38.9	22.6	38.5	--
0.1 Hz	59.7	16.8	23.5	--
0.5 Hz	0.6	3.5	5.6	90.3
1 Hz	0.8	3.4	5.3	90.5

To gain better understanding of the surface microstructure and composition, TEM and EDS analysis were carried out on Al-Mn thin film after tribocorrosion test at 0.05 Hz scratching frequency. The results are summarized in Figs. 2.10-2.12. High-resolution TEM images (not shown here) right below the wear track shows that besides

high surface roughness, no amorphous to crystalline phase transition were observed right below the worn surface. Fig. 2.10 shows that an oxygen (O) rich layer (bright layer under Pt coating) developed throughout the sample surface. Within the wear track, the thickness of this surface layer is ~ 17.6 nm and remains relatively uniform on the worn surface. Far away from the wear track, the thickness of surface layer is highly nonuniform, where locations of thick (~ 50-100 nm) corrosion product can be often detected, as shown in Fig. 2.12. Interestingly, EDS analysis (Fig. 2.11) shows that the oxygen-rich surface layer contains mainly O and Al, while Mn is completely absent despite their high concentration in the thin film. Similar observations were made from areas far away from the wear track (Fig. 2.12). In Fig. 2.12, Cl was also detected from the surface corrosion product, although it is absent within the wear track. This result confirmed that in corrosion-only condition, the ingression of Cl^- ion into the passive film leads to the break-down of the passive film and subsequent growth of the corrosion product. The absence of Mn in the surface oxide layer is indeed in agreement with prior x-ray photoelectron spectroscopy study from others, which showed that the passive film of Al-Mn in NaCl aqueous solution mainly consists of AlO(OH), and Mn was selectively dissolved in the exterior part of the oxide film [41]. The absent of Mn in the surface layer leads to mainly a disordered layer of alumina oxide and aluminum hydroxide. Due to the low ionic potential of Al_2O_3 (4.4), such surface is often abrasive instead of lubricious [42]. Thus during tribocorrosion, corrosion may further accelerate wear by trapping abrasive aluminum oxide-rich wear debris between the contacting surfaces.

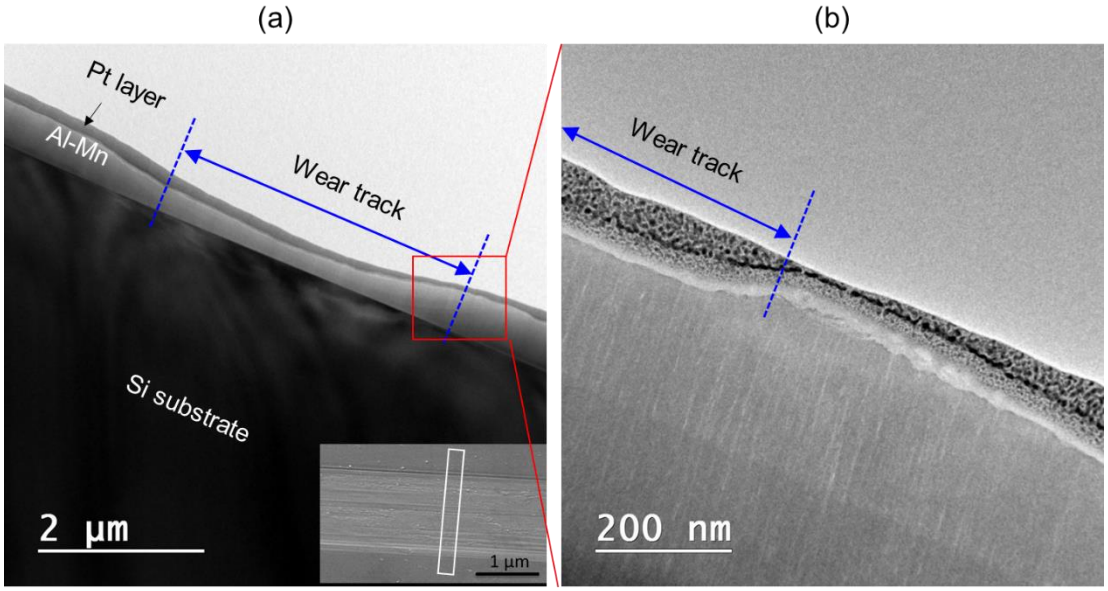

Figure 2.10 Cross-sectional (a) low and (b) high magnification TEM image of Al-Mn thin film after tribocorrosion at 0.05 Hz scratching frequency. Inset in (a) shows the surface SEM image of the sample, where the box area indicates the TEM sample location.

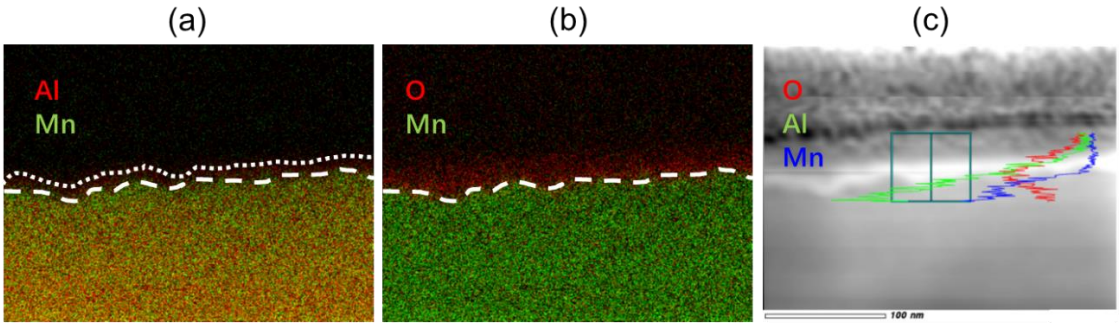

Figure 2.11 (a-b) STEM-EDS element maps and (c) element composition line profiles overlayed on the STEM image from regions within the wear track of cross-sectional Al-Mn TEM sample.

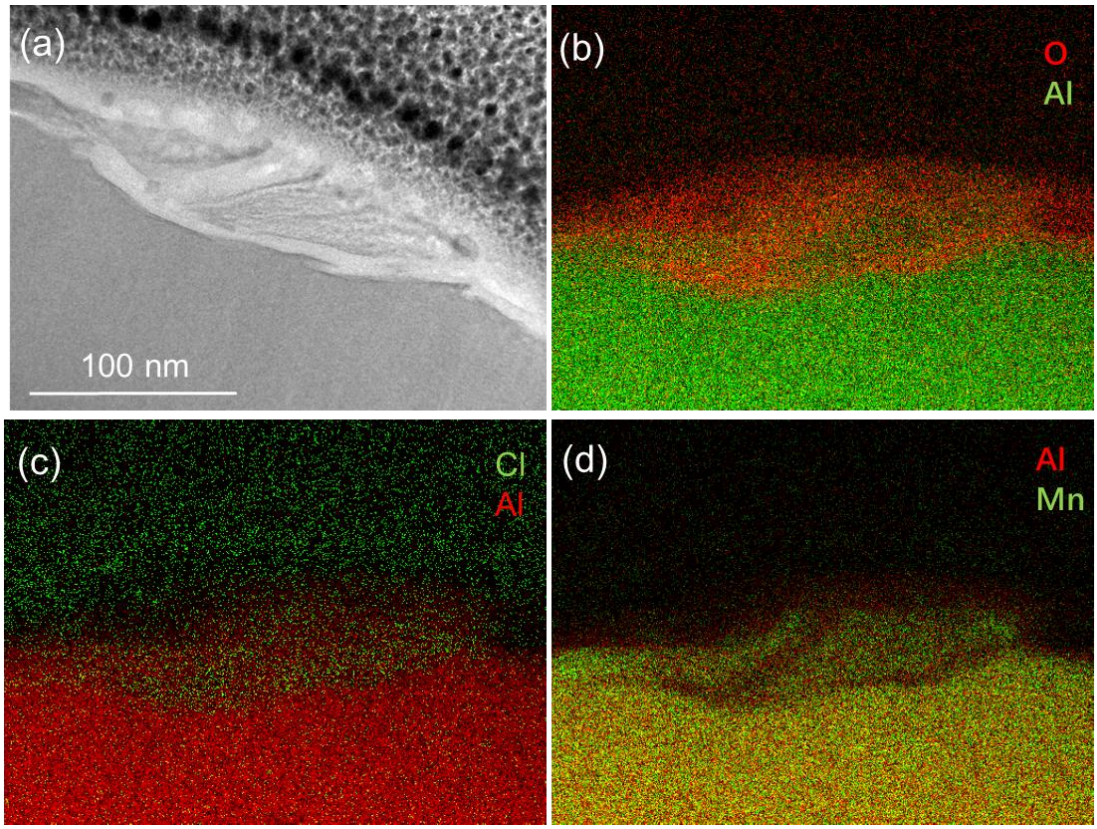

Figure 2.12 (a) Bright-field TEM image, and (b)-(d) STEM-EDS element maps from regions far away from the wear track of cross-sectional Al-Mn TEM sample.

2.5 Conclusions

In summary, scratching frequency was found to play an important role on the tribocorrosion resistance of Al-Mn amorphous thin films in 0.6 M NaCl aqueous solution. By performing the tribocorrosion test under an imposed anodic potential, the mechanical and chemical wear during tribocorrosion have been quantified. Combining tribocorrosion testing, electrochemical analysis, and material characterization, the following conclusions can be drawn:

1) Increasing sliding frequency led to higher tribocorrosion rate, coefficient of friction, and surface current of Al-Mn thin film.
2) Both chemical and mechanical wear increased with increasing frequency. The mechanical wear increased with frequency due to faster depassivation rate and increased real contact area, while chemical wear increased with frequency due to higher repassivation kinetics.

3) Anodic current in the wear track during tribocorrosion increased monotonically with frequency, but not linearly.
4) The subsurface of Al-Mn remained amorphous after tribocorrosion. The outmost surface layer is rich in aluminum and oxygen but lean in manganese. The thickness of this layer remains uniform within the wear track but becomes highly non-uniform outside the wear track due to localized corrosion.

References

1. Bezi, Z., et al., *Processing of ultrafine-grained titanium with high strength and good ductility by a combination of multiple forging and rolling.* Materials Science and Engineering a-Structural Materials Properties Microstructure and Processing, 2017. **688**: p. 210-217.
2. Chen, L.B., et al., *Heavy carbon alloyed FCC-structured high entropy alloy with excellent combination of strength and ductility.* Materials Science and Engineering a-Structural Materials Properties Microstructure and Processing, 2018. **716**: p. 150-156.
3. Zhou, Y.X., et al., *Innovative processing of obtaining nanostructured bainite with high strength - high ductility combination in low-carbon-medium-Mn steel: Process-structure-property relationship.* Materials Science and Engineering a-Structural Materials Properties Microstructure and Processing, 2018. **718**: p. 267-276.
4. Liu, S., et al., *The significance of multi-step partitioning: Processing-structure property relationship in governing high strength-high ductility combination in medium-manganese steels.* Acta Materialia, 2017. **124**: p. 159-172.
5. Lytle, D.A. and M.R. Schock, *Pitting corrosion of copper in waters with high pH and low alkalinity.* Journal American Water Works Association, 2008. **100**(3): p. 115-+.
6. Hu, X.M. and A. Neville, *CO2 erosion-corrosion of pipeline steel (API X65) in oil and gas conditions-A systematic approach.* Wear, 2009. **267**(11): p. 2027-2032.

7. Nordhagen, H.O., et al., *A fracture-propagation-control model for pipelines transporting CO2-rich mixtures including a new method for material-model calibration.* Engineering Structures, 2017. **143**: p. 245-260.
8. Parvizsedghy, L. and T. Zayed, *Consequence of Failure: Neurofuzzy-Based Prediction Model for Gas Pipelines.* Journal of Performance of Constructed Facilities, 2016. **30**(4).
9. Marcus, G.H., *Considering the next generation of nuclear power plants.* Progress in Nuclear Energy, 2000. **37**(1-4): p. 5-10.
10. Tekin, K.C. and U. Malayoglu, *Assessing the Tribocorrosion Performance of Three Different Nickel-Based Superalloys.* Tribology Letters, 2010. **37**(3): p. 563-572.
11. Zhao, C.L., et al., *Development of PLA/Mg composite for orthopedic implant: Tunable degradation and enhanced mineralization.* Composites Science and Technology, 2017. **147**: p. 8-15.
12. Yan, Y., et al., *Biotribocorrosion of CoCrMo orthopaedic implant materials - Assessing the formation and effect of the biofilm.* Tribology International, 2007. **40**(10-12): p. 1728-1728.
13. Xie, M., et al., *Stabilizing an amorphous V2O5/carbon nanotube paper electrode with conformal TiO2 coating by atomic layer deposition for lithium ion batteries.* Journal of Materials Chemistry A, 2016. **4**(2): p. 537-544.
14. Wang, Y. and O. Northwood, *Effects of O-2 and H-2 on the corrosion of SS316L metallic bipolar plate materials in simulated anode and cathode environments of PEM fuel cells.* Electrochimica Acta, 2007. **52**(24): p. 6793-6798.
15. Landolt, D., S. Mischler, and M. Stemp, *Electrochemical methods in tribocorrosion: a critical appraisal.* Electrochimica Acta, 2001. **46**(24-25): p. 3913-3929.
16. Mischler, S., *Sliding Tribo-Corrosion of Passive Metals: Mechanisms and Modeling.* Tribo-Corrosion: Research, Testing, and Applications, 2013. **1563**: p. 1-18.

17. Pokhmurs'kyi, V.I. and V.M. Dovhunyk, *Tribocorrosion of Stainless Steels (Review).* Materials Science, 2010. **46**(1): p. 87-96.
18. Lopez-Ortega, A., J.L. Arana, and R. Bayon, *Tribocorrosion of Passive Materials: A Review on Test Procedures and Standards.* International Journal of Corrosion, 2018.
19. Mraied, H. and W.J. Cai, *The effects of Mn concentration on the tribocorrosion resistance of Al-Mn alloys.* Wear, 2017. **380-381**: p. 191-202.
20. Vashi, R.T. and R.N. Patel, *Corrosion of aluminium, zinc and mild-steel in an industrial atmosphere.* Journal of the Indian Chemical Society, 2004. **81**(8): p. 680-682.
21. Pride, S.T., J.R. Scully, and J.L. Hudson, *Metastable Pitting of Aluminum and Criteria for the Transition to Stable Pit Growth.* Journal of the Electrochemical Society, 1994. **141**(11): p. 3028-3040.
22. Scully, J.R., et al., *Electrochemical Characteristics of the Al2cu, Al3ta and Al3zr Intermetallic Phases and Their Relevancy to the Localized Corrosion of Al-Alloys.* Corrosion Science, 1993. **35**(1-4): p. 185-195.
23. Birbilis, N. and R.G. Buchheit, *Electrochemical characteristics of intermetallic phases in aluminum alloys - An experimental survey and discussion.* Journal of the Electrochemical Society, 2005. **152**(4): p. B140-B151.
24. Mraied, H., W.J. Cai, and A.A. Sagues, *Corrosion resistance of Al and Al-Mn thin films.* Thin Solid Films, 2016. **615**: p. 391-401.
25. Salasi, M., G. Stachowiak, and G. Stachowiak, *Tribo-electrochemical behaviour of 316L stainless steel: The effects of contact configuration, tangential speed, and wear mechanism.* Corrosion Science, 2015. **98**: p. 20-32.
26. Li, X.Y., et al., *Depassivation-repassivation Behavior of a CoCrMo Alloy under Tribological Contact in Simulated Body Fluids.* International Journal of Electrochemical Science, 2017. **12**(3): p. 2495-2505.
27. Stemp, M., S. Mischler, and D. Landolt, *The effect of mechanical and electrochemical parameters on the tribocorrosion rate of stainless steel in*

sulphuric acid. Wear, 2003. **255**: p. 466-475.

28. Mischler, S., S. Debaud, and D. Landolt, *Wear-accelerated corrosion of passive metals in tribocorrosion systems.* Journal of the Electrochemical Society, 1998. **145**(3): p. 750-758.
29. Ruan, S.Y. and C.A. Schuh, *Electrodeposited Al-Mn alloys with microcrystalline, nanocrystalline, amorphous and nano-quasicrystalline structures.* Acta Materialia, 2009. **57**(13): p. 3810-3822.
30. Cai, W.J. and C.A. Schuh, *Tuning nanoscale grain size distribution in multilayered Al-Mn alloys.* Scripta Materialia, 2012. **66**(3-4): p. 194-197.
31. Priya, R., C. Mallika, and U.K. Mudali, *Wear and tribocorrosion behaviour of 304L SS, Zr-702, Zircaloy-4 and Ti-grade2.* Wear, 2014. **310**(1-2): p. 90-100.
32. Zhang, L., et al., *Microstructure and properties of 1Cr12Ni2WMoVNb (GX-8) steel bored barrels with and without QPQ treatment.* Surface & Coatings Technology, 2017. **315**: p. 95-104.
33. Parker, R.C. and D. Hatch, *The Static Coefficient of Friction and the Area of Contact.* Proceedings of the Physical Society of London Section B, 1950. **63**(363): p. 185-&.
34. Cieplak, M., E.D. Smith, and M.O. Robbins, *Molecular-Origins of Friction - the Force on Adsorbed Layers.* Science, 1994. **265**(5176): p. 1209-1212.
35. Watson, S.W., et al., *Methods of Measuring Wear Corrosion Synergism.* Wear, 1995. **181**: p. 476-484.
36. Landolt, D., *Electrochemical and materials aspects of tribocorrosion systems.* Journal of Physics D-Applied Physics, 2006. **39**(15): p. 3121-3127.
37. Vieira, A.C., et al., *Mechanical and electrochemical deterioration mechanisms in the tribocorrosion of Al alloys in NaCl and in NaNO3 solutions.* Corrosion Science, 2012. **54**: p. 26-35.
38. Mischler, S. and A.I. Munoz, *Wear of CoCrMo alloys used in metal-on-metal hip joints: A tribocorrosion appraisal.* Wear, 2013. **297**(1-2): p. 1081-1094.
39. Mischler, S., A. Spiegel, and D. Landolt, *The role of passive oxide films on the*

degradation of steel in tribocorrosion systems. Wear, 1999. **225**: p. 1078-1087.

40. Mischler, S., *Triboelectrochemical techniques and interpretation methods in tribocorrosion: A comparative evaluation.* Tribology International, 2008. **41**(7): p. 573-583.

41. Zhang, J.F., et al., *Corrosion behaviors of Zn/Al-Mn alloy composite coatings deposited on magnesium alloy AZ31B (Mg-Al-Zn).* Electrochimica Acta, 2009. **55**(2): p. 560-571.

42. Erdemir, A., *A crystal chemical approach to the formulation of self-lubricating nanocomposite coatings.* Surface & Coatings Technology, 2005. **200**(5-6): p. 1792-1796.

Chapter 3:

The Origin of Passivity in Aluminum-Manganese Solid Solutions

Jia Chen[a,1], Jianwei Xiao[b,1], Jonathan Poplawsky[c], F. Marc Michel[d], Chuang Deng[b,*], Wenjun Cai[a,*]

a Department of Materials Science and Engineering, Virginia Polytechnic Institute and State University, Virginia, 24061, United States

b Department of Mechanical Engineering, University of Manitoba, Winnipeg, MB R3T 5V6, Canada

c The Center for Nanophase Materials Sciences, Oak Ridge National Laboratory, Tennessee, 37831, United States

d Department of Geosciences, Virginia Polytechnic Institute and State University, Virginia, 24061, United States

*Corresponding author E-mail addresses: Chuang.Deng@umanitoba.ca, caiw@vt.edu.

Declarations of interest: none

*This chapter has been adapted from a **published** manuscript by Jia Chen, Jianwei Xiao, Jonathan Poplawsky, F. Marc Michel, Chuang Deng, and Wenjun Cai from the following reference:*

Jia Chen, et al. "The Origin of Passivity in Aluminum-Manganese Solid Solutions." Corrosion Science, vol. 173, 2020.

Reprinted with permission from the Elsevier.

3.1 Abstract

The effects of manganese on the aqueous corrosion of aluminum-manganese alloys were investigated by experiments and atomistic simulations. Electrochemical measurements, x-ray photoelectron spectroscopy, and atom probe tomography analysis indicate that manganese addition enhanced the corrosion resistance of aluminum without participating in the surface oxidation. The selective dissolution of manganese was believed to increase the free volume at the metal/oxide interface to facilitate the formation of a denser, thinner oxide layer with closer to stoichiometry composition. Atomistic simulations showed that the oxide layer compactness increased, and defect density decreased with increasing free volume content in Al, resulting in enhanced barrier characteristics.

3.2 Introduction

The design of strong and corrosion-resistant alloys, especially those containing lightweight elements such as Al are challenged by the trade-off between strength and corrosion resistance. Solute tends to have small equilibrium solubility limit in Al due to their relatively large negative enthalpy of mixing with Al [1]. As a result, extensive precipitates are often formed to strengthen Al alloys, which compromises corrosion resistance due to the microgalvanic coupling with the metal matrix (with the matrix serving as the local anode) [2, 3]. The presence of precipitates also degrades the passive film's resistance to localized corrosion due to the thickness incompatibility between the precipitates and Al matrix [4]. Such design challenge is also complicated by the fact that a fundamental understanding of the far-from-equilibrium structure, property, and formation mechanism of the passive layer of Al alloys is still lacking, where unusual combinations of structure and chemical composition are a general phenomenon, resulting from different diffusion and transport rates of the constituting elements, selective dissolution or oxidation, and the moving oxidation front, as pointed out recently by Yu et al. in the 'nonequilibrium solute capture' theory [5].

An outstanding question is how to select the appropriate alloying elements and composition to obtain a naturally occurring, protective, and mechanically robust oxide layer on the surface of Al yet minimizing the strength-corrosion resistance trade-off. In the present work, we evaluate an intriguing hypothesis, that the corrosion resistance of Al alloys could be enhanced by increasing the content of a non-passive element (Mn) in solid solution; such non-passive element is selectively dissolved at the surface to enhance surface activity of Al and facilitate the formation of a more compact (i.e. higher density), thinner, yet protective surface oxide layer with closer to stoichiometry composition than those on pure Al or dilute Al-Mn alloys. Here, solid solution is chosen as an 'electrochemically benign' strengthening mechanism that does not introduce measurable chemical heterogeneity [6-9]. Thanks to the fast effective quenching rate during non-equilibrium processes such as physical vapor deposition, metastable solid solutions of Al-based binary and ternary thin films have been prepared and their corrosion properties studied extensively [6-12]. Previous studies show that the effects of alloying additions on the pitting corrosion resistance of such Al-based solid solutions are complex [12, 13]. Small quantities of Sn, In, Hg, Ga, and Zn are found to be detrimental to Al corrosion, as they reduce the passive potential region and shift the corrosion and pitting potentials in the negative direction [14]. Thus, these alloying elements lead to high anodic current density and uniform active surface corrosion. Other alloying elements such as Cu, Mo, Mn, W, Nb, Cr, Ta, V, and Zr improve corrosion resistance and decrease pitting susceptibility of Al by increasing the overpotential for anodic dissolution and decreasing metastable pit initiation and growth rates [6, 15]. Specifically, in terms of the roles of Mn addition, the pitting resistance of Al was improved by ~ 350-500 mV and corrosion current density reduced by ~ 2-10 times when alloyed with up to ~ 30 at.% Mn compared to pure Al [10, 11, 16]. It should also be noted that with increasing Mn content, the microstructure of the alloy experiences a transition from nanocrystalline to complete amorphous structure at high Mn content [11, 16-18]. However, as reported previously [11], the pitting potential increases monotonically with Mn content up to ~ 20 at.%, regardless of its crystallinity.

It is also interesting to note that when Mn content further increases to above ~ 40 at.%, a reduction of pitting potential was also reported [16]. Several explanations have been proposed to elaborate the roles of Mn on the corrosion behavior of Al. It was suggested that its influence on the composition of the passive layer is small, rather its effects on enhancing the corrosion resistance of Al has been attributed to its influence on the pH of zero charge of the passive film, the solubility of dissolved species in the pit solution, enrichment of the solute species at the active surface in a pit, and ennobling the pit dissolution kinetics [10, 16, 19-21]. It was argued that when Mn is added, higher potentials are needed to achieve the high current densities necessary for stable pit growth compared to pure Al, which leads to higher pitting potential [19, 22]. Limited studies have been performed to identify the structural origin of such corrosion behavior. For example, Crossland et al. [23] studied the structure of barrier-type anodic films (~ 132 nm thick) of Al-2.5 at.% Mn and Al-16 at. % Mn in ammonium pentaborate, sodium hydroxide, and sulphuric acid electrolytes. They found that under the anodization voltage of 60 and 100 V, the faster migration of Mn species than Al leads to the formation of a bilayered anodic film in pentaborate and hydroxide solutions (pH > 7), with the inner film enriched in Al_2O_3 and MnO, and an outer layer of primarily Mn_2O_3. However, in sulphuric acid (pH < 7), no outer Mn-rich layer was observed. On the other hand, Zhang et al. [21] showed that the passive film of Al-23.7 wt.% Mn at open circuit potential contains mainly alumina and hydrated alumina during long term (2808 h) immersion in 3.5 wt.% NaCl aqueous solution, while no prominent Mn oxide was detected, similar to those reported by Moffat et al. [20].

The lack of fundamental understanding of the atomistic structure, composition, and chemical state of the passive layer and their formation mechanism, which is difficult to characterize due to its thinness and delicate structure, has greatly hindered our understanding of the specific roles Mn play on the corrosion behavior of Al. Such challenge is coupled with a lack of understanding of the defect type and density in the passive layer, which often dominate the charge and mass transfer events that govern both the oxide growth and metal dissolution kinetics. For example, the argument on the

pit dissolution kinetics cannot explain why the pitting potential of Al-Mn starts to decrease when Mn% is above ~ 40 at.%. The present work aims to combine atomistic surface characterization (e.g. 3D atom probe tomography) and computer simulation (molecular dynamics) to understand the roles of Mn addition on the structure, chemistry, and protectiveness of the surface oxide layer of Al-Mn alloys and its barrier characteristics. Atom probe tomography (APT) is the only technique so far capable of producing 3D compositional reconstructions with sub-nanometer-scale resolution and ~10 ppm sensitivity, and has only recently been applied to corrosion science [24-26]. Specifically, we studied the aqueous corrosion of a concentrated binary alloy of Al-20 at.% Mn, commercial Al-Mn alloy (Al 3003), and high purity Al. Finally, a rationalization of the origin of passivity in Al-based solid solution is proposed based on the experimental and simulation results. The obtained understanding could shed light on the design of new corrosion-resistant concentrated alloys such as multi-principle elements alloys, high entropy alloys, and metallic glasses.

3.3 Experimental procedure

Al-Mn thin films with a nominal composition of 20.3 at.% Mn were prepared by direct current (DC) magnetron sputtering on (100) silicon (Si) wafers. Sputtering was operated inside a vacuum chamber (PVD 75, Kurt J. Lesker, Pennsylvania, USA), applying 200W power for the Al (99.99 %, Kurt J. Lesker, Pennsylvania, USA) target and 38W for the Mn target (99.95 %, Kurt J. Lesker, Pennsylvania, USA) under 5.9×10^{-3} Torr argon atmosphere (99.99 %). Prior to the deposition, Si wafers were etched with 1:20 hydrofluoric acid water solution to remove the natural oxidation layer. The thickness of the thin film was ~ 1.2 μm, measured by a contact profilometer (DektakXT, Bruker, Massachusetts, USA). The chemical composition of samples was characterized by energy-dispersive X-ray spectroscopy (EDS, Quantax, Bruker, Massachusetts, USA) in a scanning electron microscopy (SEM, Quanta 600 FEG, FEI, Oregon, USA) under 10 keV.

Electrochemical measurements were performed on as-deposited and anodized Al-

20 at.% Mn thin films (hereafter referred as AM20 and a-AM20 respectively), Al 3003 (Metal Supermarkets, Florida, USA), and high purity Al (99.99 %, Alfa Aesar, Massachusetts, USA) with an effective exposed area of ~ 1 cm^2. The chemical composition (in mass fraction) of Al 3003 is 1.14 % Mn, 0.15 % Cu, 0.60 % Fe, 0.10 % Si, and balanced Al. A potentiostat/galvanostat/zero resistance ammeter (Gamry model 600, Pennsylvania, USA) was used for all electrochemical experiments in a three-electrode setup, where the sample, a mixed metal oxide coated titanium mesh, and a silver-silver chloride electrode with 1 M KCl internal solution was used as the working, counter, and reference electrode respectively. Naturally aerated 0.6 M NaCl aqueous solution with pH ≈ 6.4 at 25 ± 2 °C was used as the electrolyte in all experiments. The a-AM20 sample was prepared by anodic polarization of AM20 at a constant potential of 200 mV above the open circuit potential (E_{ocp}) at 15 ℃ for 2000 s. This anodizing potential was chosen within the passive region where the current density is largely independent of potential. The lower temperature (than room temperature) is chosen to suppress the generation of joule heating [27]. The enhanced protectiveness of this passive layer on a-AM20 is confirmed by the current evolution during anodizing, as shown in Fig. 3.1, where the current density decreased from ~ 7.75×10^{-8} A/cm^2 to 3.68×10^{-8} A/cm^2 after 2,000 s. Potentiodynamic polarization (PD) tests were performed with a scan rate of 0.167 mV/s for 1.5 h after stabilizing at E_{ocp} for 300 s, starting at a potential of -150 mV below E_{ocp}. Electrochemical impedance spectroscopy (EIS) analysis was performed after 300 s stabilization at E_{ocp}, with 10 mV_{rms} sinusoidal potential excitation, 100 kHz to 10 mHz frequency, and 5 points per decade. Note the time allowed for E_{ocp} stabilization (300 s) was determined by measuring the time evolution of E_{ocp} until no significant fluctuations of potential was recorded, as confirmed by E_{ocp} measurements over a longer period of 1800 s on selected samples. The obtained data was then fitted by the equivalent circuit (EC) model using Gamry E-chem software. Mott-Schottky (M-S) test was performed to analyze the electronic properties of passive layer on all samples at a frequency of 1000 Hz and scan rate of 10 mV/s, after immersion at E_{ocp} for 600 s. The potential scan range of pure Al and Al 3003

were from -1.0 V to -0.7 V vs. their respective E_{ocp} while that of AM20 and a-AM20 were from -1.0 V to -0.1 V vs. their respective E_{ocp}.

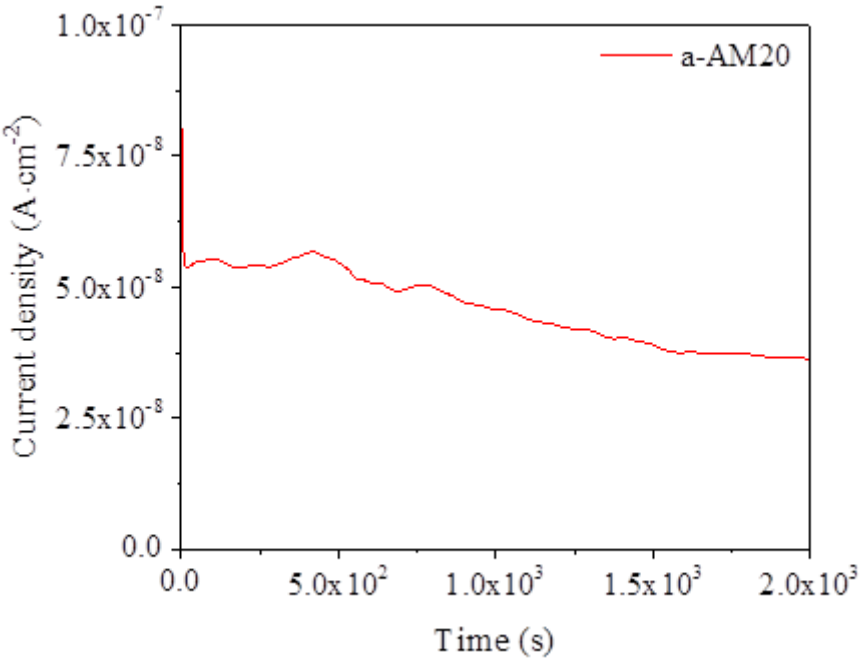

Figure 3.1 Current evolution during potentiostatic anodizing of AM-20 in 0.6 M NaCl solution at 15 ℃.

X-ray diffraction (XRD) measurements of pure Al and Al 3003 was performed using PANalytical X'pert PRO MRD at 0.01° step size, 2.5 s scan step time, using Cu Kα under 45 kV and 40 mA. Grazing incidence XRD (GI-XRD) of AM20 and a-AM20 were performed using PANalytical Empyrean Nano Edition with a grazing incidence angle of 0.9149°, 0.02° step size and 10 s scan step. The X-ray photoelectron spectroscopy (XPS, PHI Quantera SXM, USA) characterization was operated under an ultra-high-vacuum system with 10^{-9} Torr base pressure. On each sample, a monochromatic Al Kα X-ray source with a beam diameter of 100 μm and an angle of 45° source analyzer was applied to measure the sputter depth profiles. Pre-sputtering was applied for 15 s using 1 kV ion beam directly on the sample surface to remove any potential carbon contamination. The sputter depth profiles were obtained using 1-3 kV argon ions on an area of ~ 2×2 mm^2 using a number of sweeps, step sizes and pass energy, as shown in Table 3.1. The estimated instrumental resolution is ~ 0.39 eV for

O 1s spectra, 1.0 eV for Al 2p spectra and ~ 2.1 eV for Mn 2p spectra. C 1s at 285 eV was used to calibrate the spectrum prior to data analysis of each element. MultiPak analysis software was used to perform the spectral deconvolution after the curve fitting procedure.

Table 3.1 Summary of parameters in sputter depth profile.

Element	sweep	Step size (eV)	Pass energy (eV)
Al 2p	10	0.125	69
Mn 2p	10	0.125	140
O 1s	8	0.05	26

Atom probe tomography (APT) analysis was conducted on the as anodized a-AM20 and corroded a-AM20 after potentiodynamic polarization tests for 1.5 h in 0.6 M NaCl aqueous solution. The sample surface was protected by depositing a 60-100 nm Ni layer using a South Bay Technologies ion beam deposition system. APT specimens were made using a Thermo Fisher Nova 200 dual beam focused ion beam (FIB)/scanning electron microscope (SEM) with standard lift out and needle fabrication methods described by Thompson et al. [28]. An equilateral triangular prism was cut and lifted out, mounted on Si microtip array posts, and sharpened using a 30 kV Ga^+ ion beam. Pt from the needle surface was removed using a 2 kV ion beam until the deposited Ni above the oxide layer was at the needle surface. The APT experiment was run on a CAMECA LEAP 4000XHR using laser mode with a 30 K base temperature, 40-50 pJ laser power, a 0.2-0.5 % detection rate, and a 200 kHz pulse repetition rate. The APT results were reconstructed and analyzed using CAMECA's interactive visualization and analysis software (IVAS 3.8).

3.4 Experimental results

3.4.1 XRD characterization

Fig. 3.2 shows the XRD results of all samples. Pure Al and Al 3003 exhibit a single face-centered-cubic phase with a strong (200) texture parallel to the sample normal direction. A broad peak was observed around 42-43 ° for AM20, indicating the

formation of largely amorphous microstructure, in consistent with prior works on electrodeposited or sputtered Al-Mn alloys with similar compositions [10, 16, 18, 20]. Compared to AM20, the structure of a-AM20 does not change after anodizing. A small feature at ~ 34.8° was also observed in both AM20 and a-AM20, close to the (104) diffraction peak of corundum (α-Al_2O_3) (JCPDS-ICDD File No 46-1212).

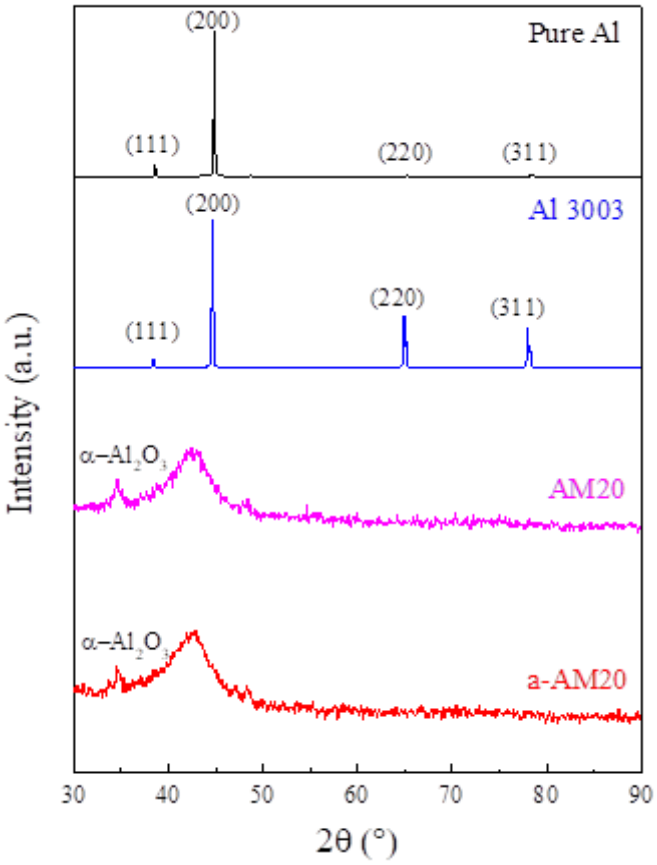

Figure 3.2 The X-ray diffraction patterns of pure Al, Al3003, as-deposited Al-20at.%Mn (AM20), and anodized Al-20at.%Mn (a-AM20).

3.4.2 Corrosion behavior

Representative PD curves and the PD results of all samples are shown in Fig. 3.3. The passive regions of AM20 and a-AM20 are much wider than those of Al3003 and pure Al. The pitting potential increased with increasing Mn content in Al, as shown in Fig. 3.3(b). In addition, the protectiveness of naturally formed passive layer on AM20 can be further improved by anodizing the alloy surface, similar to those reported on

other Al-based alloys [29, 30]. Fig. 3.4(a) shows the Nyquist plots of all samples obtained after immersion in 0.6 M NaCl aqueous solution at room temperature for 300 s under E_{ocp}. The diameter of the capacitive semicircle is largest for a-AM20, followed by AM20, Al3003 and pure Al, indicating the enhanced protectiveness of the passive layer after alloying and anodizing, consistent with the PD results. The Bode plots of all samples are shown in Fig. 4.4(c) and (d). At high frequencies, the electrolyte resistance R_s was estimated to be $\sim$ 11-15 Ω from Fig. 4.4(c). At lower frequencies, the polarization resistance increases in the sequence of pure Al, Al 3003, AM20, and a-AM20, in agreement with their PD behavior. The phase shift Bode plot (Fig. 4.4(d)) shows a wave trough for all samples in the low frequency region, characteristic of an electrical circuit with two relaxation processes. Sample a-AM20 exhibited a maximum phase angle close to -90° over a wide frequency range of 0.1 Hz-100 Hz (Figs. 4.4(d)), indicating its good capacitive response, while all others showed narrower frequency range of the capacitive effect.

The Nyquist and Bode plots were fitted using an equivalent circuit model shown in Fig. 4.4(b), where R_s represents the ohmic solution resistance, R_1 is the charge transfer resistance, R_2 is the electrolytic resistance through the passive layer defects, the constant phase element CPE_1 and CPE_2 represent the non-ideal capacitive behavior of the double layer and the passive layer respectively. The double layer is formed between the metal surface and the electrolyte. As ions from the electrolyte is adsorbed onto the metal surface, the charged metal surface is separated from the charged ions in the electrolyte by an insulating surface (typically on the orders of angstroms) to form a capacitor CPE_1. The geometrical capacitance of the passive layer, which is mainly a metal oxide layer, as shown later in Section 3.5.3, corresponds to CPE_2. This model represents just one of several possible equivalent circuits that can fit the measured EIS data. It is chosen due to its inclusion of two relaxation processes, and the fact that it has been successfully adopted in prior research for Al-Mn [11, 21] and Al-W [31] solid solutions in NaCl electrolytes. Table 3.2 summarizes the model fitting parameters. The impedance of the CPE is defined as $Z = \frac{1}{Y_0(j\omega)^n}$, Y_0 is a constant, j is the imaginary

unit, ω is the angular frequency of the sinusoidal signal, and n is an exponent in the range of $0 < n < 1$. When n = 1, the CPE behaves like an ideal capacitor; when n = 0, it behaves like a pure resistor. For CPE_2, the n_2 value increases from 0.813 for pure Al to 0.949 for a-AM20, indicating a more ideal capacitor behavior in the later. The thickness of the passive layer d was estimated by [32]

$$d = \varepsilon\varepsilon_0 A/C, \tag{3.1}$$

where ε_0 is the vacuum dielectric constant ($\varepsilon_0 = 8.85 \times 10^{-14} F \cdot cm^{-1}$), ε is the dielectric constant (relative electric permittivity) of barrier-type alumina ($\varepsilon = 20$), A is the area exposed to the electrolyte solution ($\sim$ 1 cm^2), and C is the capacitance from CPE_2. Table 3.2 shows that the values of CPE_2 increases in the order of pure Al, Al3003, a-AM20, and AM20. Hence the calculated passive layer thickness decreases in that same order. The passive layer thickness on a-AM20 is $\sim$ 4.62 nm, which is slightly higher than that on AM20 ($\sim$ 4.09 nm) but smaller than that on Al3003 (6.94 nm) and pure Al (7.25 nm).

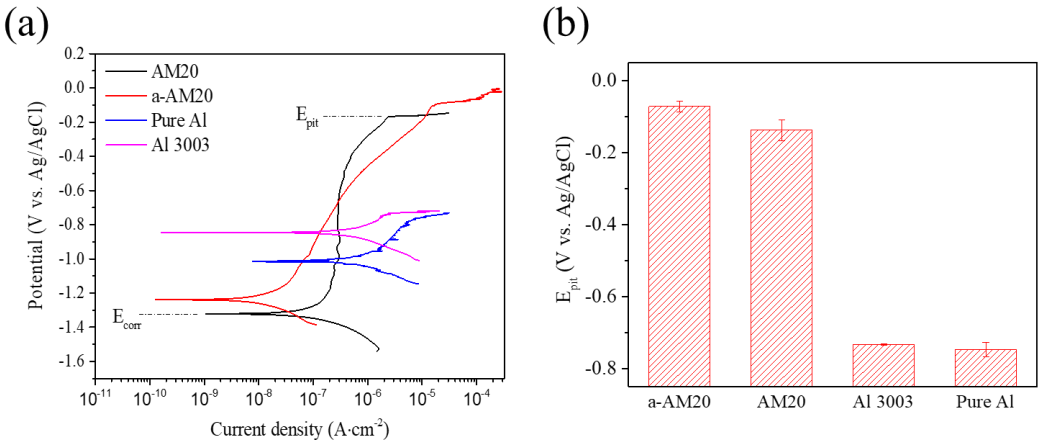

Figure 3.3 (a) Representative potentiodynamic polarization curves and (b) summary of pitting potential of all samples after corrosion in 0.6 M NaCl solution at room temperature.

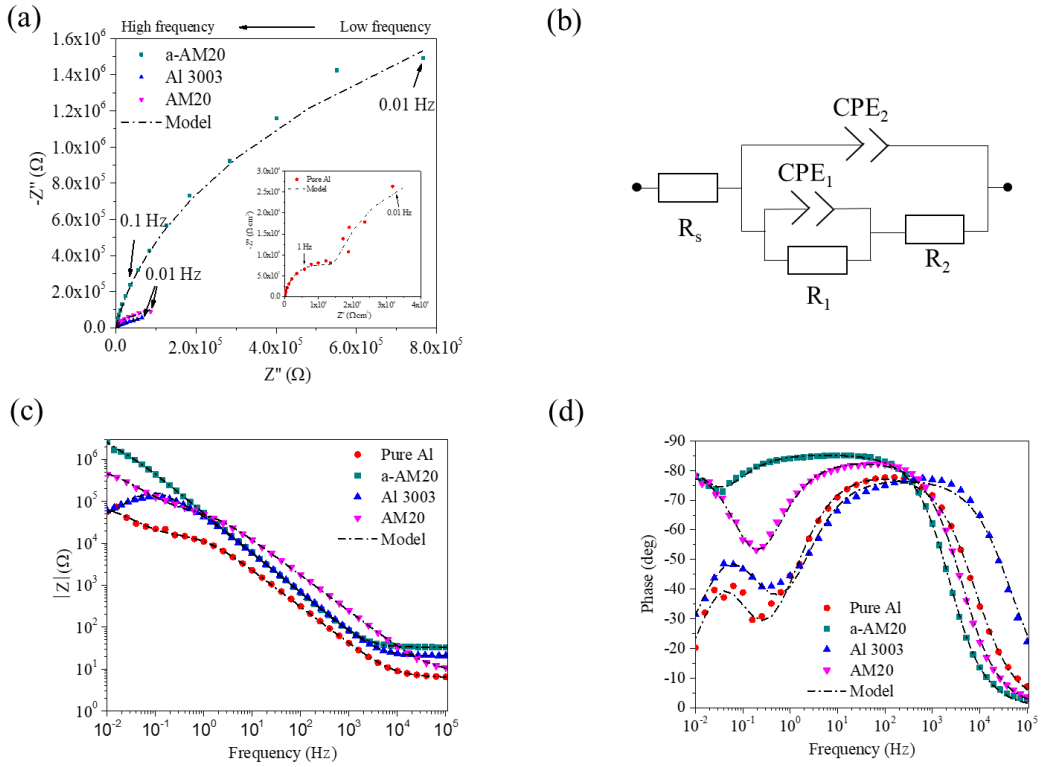

Figure 3.4 (a) Nyquist plot of EIS measurements and model fit and (b) the equivalent circuit model used for the model fitting in (a). Bode plot of the impedance (c) magnitude and (d) phase shift angle as a function of frequency from EIS measurements of all samples at open circuit potential in 0.6 M NaCl solution.

Table 3.2 Summary of equivalent circuit model fitting parameters defined in Fig. 3.4(b).

	R_s (Ω)	R_1 (Ω)	Y_1 ($S \cdot s^n$ Ω)	n_1	CPE_1 (F)	R_2 (Ω)	Y_2 ($S \cdot s^n$ Ω)	n_2	CPE_2 (F)	d (nm)
Pure Al	10.95	2.00×10^4	1.93×10^{-5}	0.838	1.61×10^{-5}	3.69×10^4	3.84×10^{-6}	0.813	2.45×10^{-6}	7.25
Al 3003	14.88	5.02×10^4	2.70×10^{-5}	0.869	2.83×10^{-5}	5.93×10^4	3.54×10^{-6}	0.826	2.55×10^{-6}	6.94
AM20	14.59	8.43×10^4	5.23×10^{-5}	0.947	5.69×10^{-5}	4.28×10^5	4.13×10^{-6}	0.922	4.33×10^{-6}	4.09
a-AM20	13.90	9.30×10^4	5.75×10^{-5}	0.967	6.09×10^{-5}	2.63×10^6	3.41×10^{-6}	0.949	3.83×10^{-6}	4.62

3.4.3 Surface characterization via XPS

Fig. 3.5 shows the element depth profile measured from XPS over 24 sputtering cycles, where the metal/oxide interface was defined by a change of bulk alloy concentration by ~ 10 %. It can be seen that the trend of surface oxide layer thickness of all samples is consistent with the EIS results. Mn was absent from Al3003 due to its low concentrations (~ 0.6 at.%). In AM20 and a-AM20, Mn concentration decreases

from 20 at.% at the metal/oxide interface to zero at the oxide surface, confirming their selective dissolution in the passive layer. In the outer surface of the oxide, the composition of oxide is ~ $Al_{33}O_{67}$ for pure Al, $Al_{36}O_{64}$ for Al3003, and $Al_{40}O_{60}$ for AM20 and a-AM20. Such results indicate that ~ 20 at.% Mn addition in these alloys and its selective surface dissolution brings the surface oxide composition to the exact stoichiometry of its stable oxide (i.e. corundum Al_2O_3).

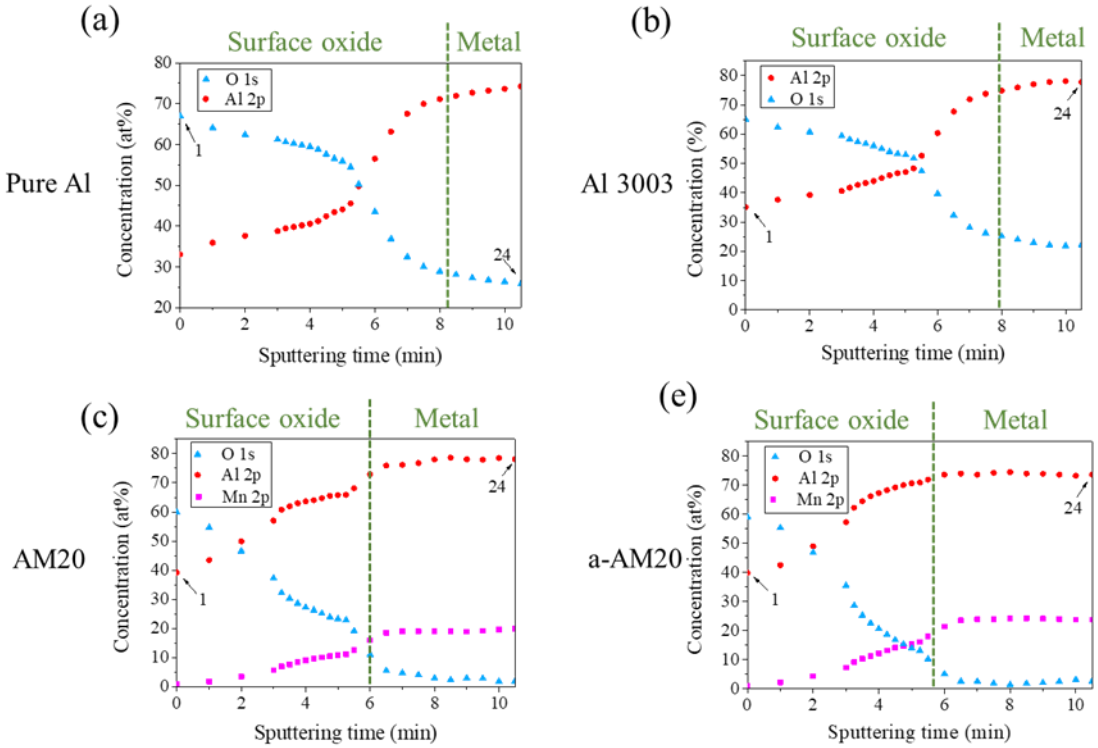

Figure 3.5 XPS depth-profile for O, Al, and Mn elements of all samples.

Fig. 3.6 summarizes the Al 2p, O 1s and Mn 2p core levels for all samples as a function of sputtering cycle, where cycle 1 corresponds to the outmost surface. The Al 2p spectra fitting of selected samples are provided in the supplementary materials (Fig. 3.7-3.8). For pure Al, the outer surface contains aluminum oxide, AlO(OH) and a small amount of Al-Al bond. The intensities of both aluminum oxide and AlO(OH) dramatically decreases after 24 cycles (~ 10 min sputtering time), while the O content around 25 at.% can still be detected. A similar trend was also observed for Al 3003. Aluminum oxide, AlO(OH) and $Al(OH)_3$ have been detected near the top surface of a-AM20 before and after potentiodynamic polarization for 1.5 h while only Al oxide and

AlO(OH) have been detected for AM20. In terms of Mn 2p spectra, for both AM20 and a-AM20, Mn remains in the elemental form throughout the surface oxide layer, with extremely low concentrations in the first three cycles (~ 2 min sputtering time), while those of Mn oxide species was absent (whose binding energy is at 640.5 eV and 642.3 eV). A similar behavior was observed for corroded a-AM20, with the exception that a very small intensity of MnO_2 was detected on the outmost surface (cycle 1). This observation is somewhat in agreement with prior research. For example, Zhang et al. [21] showed that Mn is present on the surface of anodized Al-Mn but becomes absent after long term (2808 h) immersion in NaCl aqueous solution.

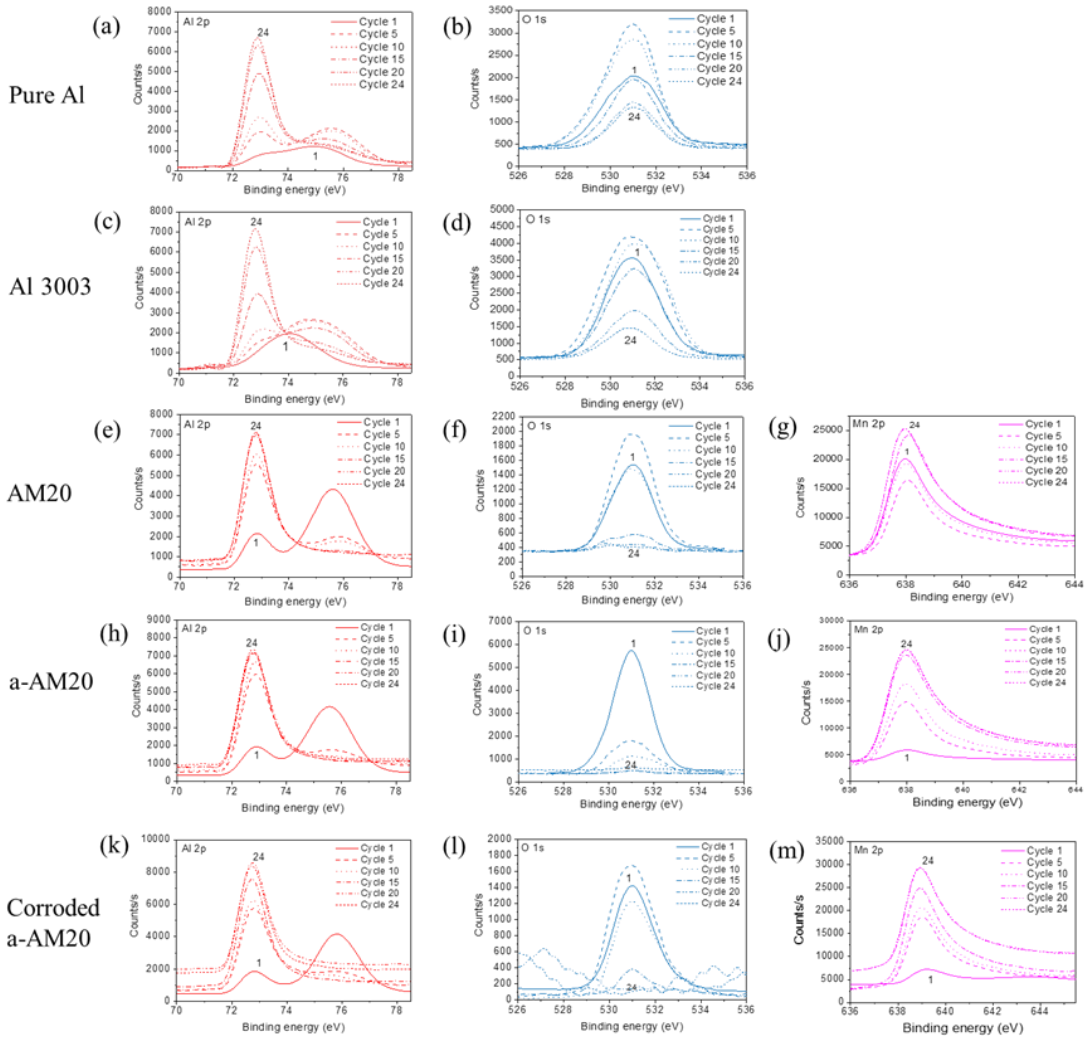

Figure 3.6 XPS depth-profile of Al 2p, O 1s, and Mn 2p spectra for all samples.

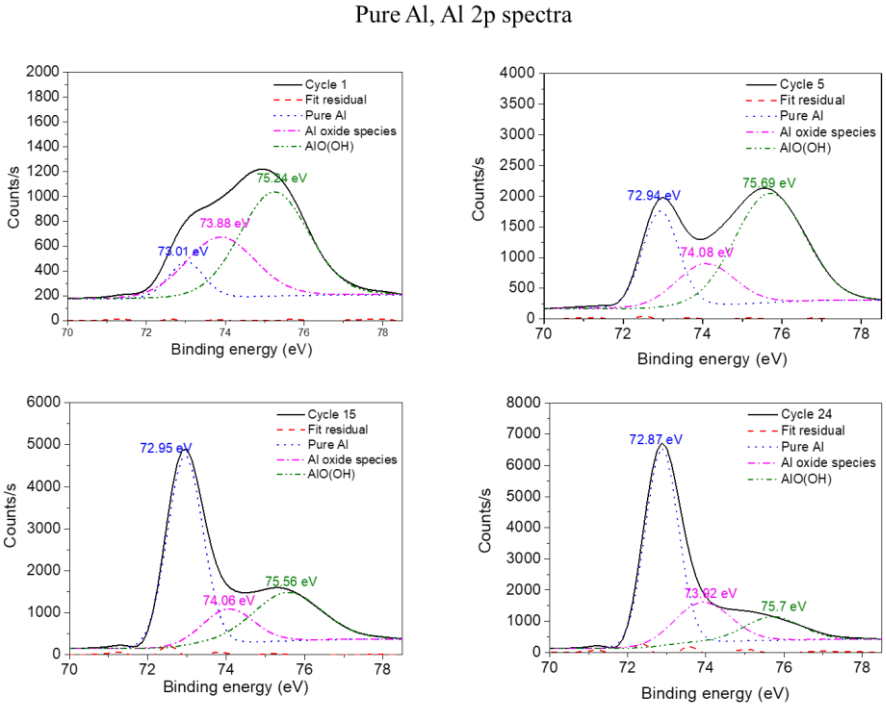

Figure 3.7 Summary of Al 2p spectra as a function of XPS sputtering cycles of pure Al.

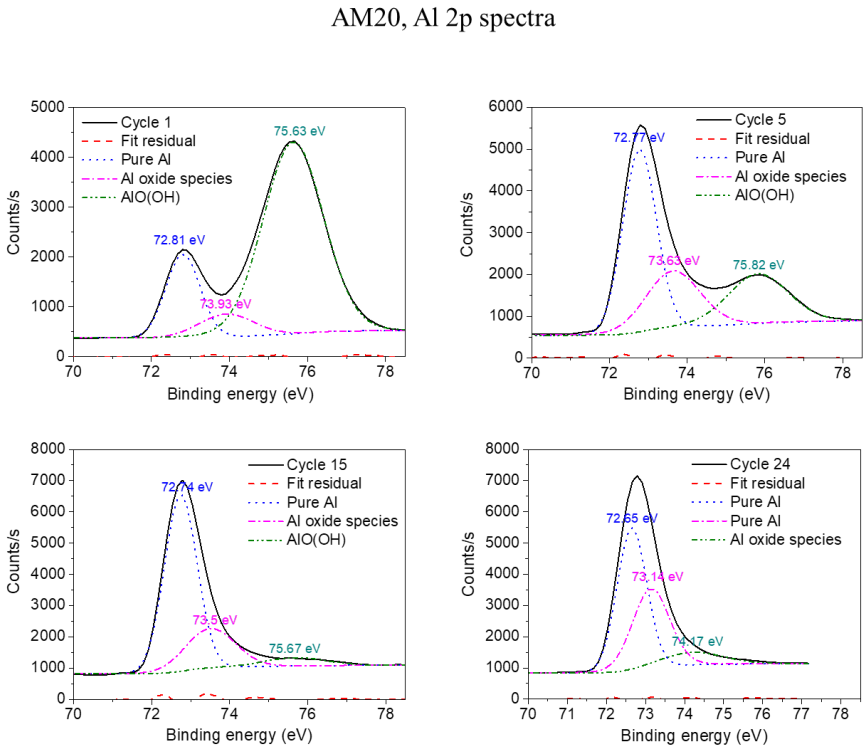

Figure 3.8 Summary of Al 2p spectra as a function of XPS sputtering cycles of AM20.

3.4.4 APT results

To further understand the atomic structure of the oxide layer that provided the

corrosion protection on the metal surface, APT analysis was performed on selected samples with the results presented in Fig. 3.9. APT atom maps are shown in Fig. 3.9(a) and (b) for the a-AM20 sample before and after corrosion. Fig. 3.9(c) and (d) display the 1D concentration profiles of the oxide/alloy interfaces, which were calculated using proximity histograms of 10 at.% O isoconcentration surfaces within density corrected (using the Z-redistribution algorithm) 15×15×50 nm ROIs extracted from the center of the dataset [33, 34]. The results show ~ 4 nm and 8 nm surface oxide layers formed on a-AM20 before and after PD corrosion, respectively. The thickness of a-AM20 before corrosion is in good agreement with the EIS results (4.78 nm). In both cases, the oxide layer is mainly enriched in Al and O with an Al/O ratio close to 2:1, while that of Mn is largely absent, as shown in Fig. 3.9(c) and (d). The MnO mass spectral peaks were found to be basically zero in the oxide layer and the metal substrate. Such results are consistent with our prior TEM analysis on anodized $Al_{80}Mn_{20}$ after tribocorrosion [35]. Interestingly, in both cases, a slight enrichment of Mn near the oxide/metal interface was also observed, similar to those reported previously in anodized Al-Mn alloys [23].

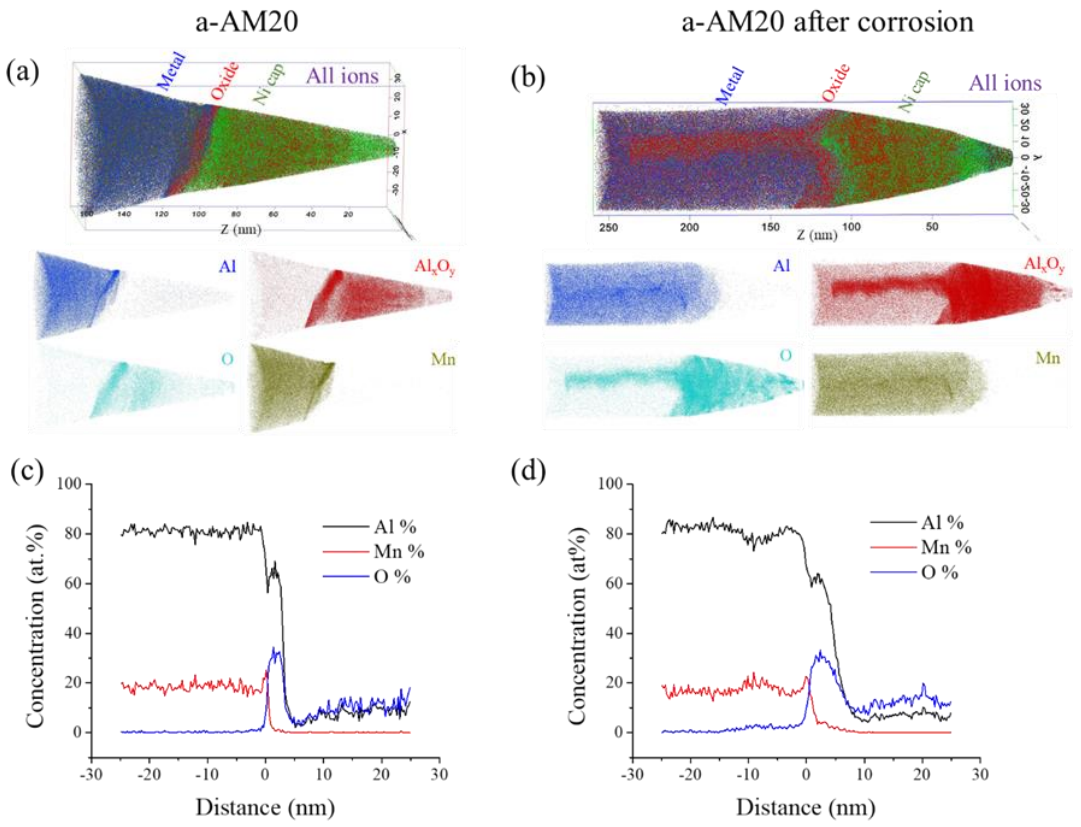

Figure 3.9 3D re-constructed surface of (b) a-AM20 and (b) a-AM20 after corrosion,

and (b, d) element concentration line profile of the 3D re-constructed surfaces.

3.4.5 Defect characterization by Mott-Schottky (M-S) analysis

Fig. 3.10 summarizes the M-S analysis results of all samples. Here, the capacitance of the Helmholtz layer is assumed to be much bigger than the semiconductor capacitance of the passive layer, hence the measured capacitance of the interfacial double layer C is taken as the semiconductor capacitance of the passive layer to calculate the defect densities according to the following equation [21, 36-39]:

$$\frac{1}{C^2} = \frac{\pm 2}{\varepsilon \varepsilon_0 eN}\left(E - E_{fb} - \frac{kT}{e}\right), \tag{3.2}$$

where C is the capacitance, ε is the passive film dielectric constant (10 for Al_2O_3 [32]), ε_0 is the permittivity of vacuum ($\varepsilon_0 = 8.85 \times 10^{-14} F/cm$), N is the dopant density, E is the applied potential, E_{fb} is the flat band potential, k is the Boltzmann constant (1.38×10^{-23} JK^{-1}), T is the absolute temperature, and e is the elementary charge (1.602×10^{-19} C). It was found that while only n-type defects such as oxygen vacancies and cation interstitials (e.g. Al^{3+}) were observed in pure Al, all Al-Mn alloys contain p-type defect (e.g. cation vacancies) at low potentials and n-type defect at high potentials. As Mn% increases, the density of n-type defect decreases while that of p-type increases (except after anodizing). These results indicate alloying with Mn changed the metal-excess oxide (n-type) of Al into a metal-deficit (p-type) oxide at low potentials, most likely due to the selective dissolution of Mn, thus leaving behind cation vacancies. At higher potentials, with increased population of Al^{3+} interstitials due to polarization, the surface oxide becomes n-type again, but with lower defect density than pure Al, probably due to the originally lower (or absent) O^{2-} vacancies and Al^{3+} interstitials. A similar "V-shaped" p-n junction behavior has also been reported for anodic aluminum oxide films [40], passive films formed on Fe-based amorphous alloys after corrosion in acetic acid [41], and those on AISI 304 stainless steel in NaCl aqueous solution [42]. In the present work, such p-n junction could be interpreted as two capacitors in series, one corresponding to the p-Al_2O_3/n-Al_2O_3 interface and the other to the n-Al_2O_3/electrolyte interface [43].

Fig. 3.10(c) summarizes the n-type defect density and pitting potential of all samples. It can be seen that as the n-type defect density decreases, the pitting potential increases. This is in good agreement with the classical point defect theory [44], which assumes that pitting corrosion initiates at the oxide/solution interface involving the adsorption of chloride ions into oxygen vacancies [44]. Hence a reduced n-type defect density leads to reduced chloride adsorption, and better pitting resistance. Although not fully understood at this point, these results indicate the complex defect state due to selective dissolution of the solute element Mn at different potentials.

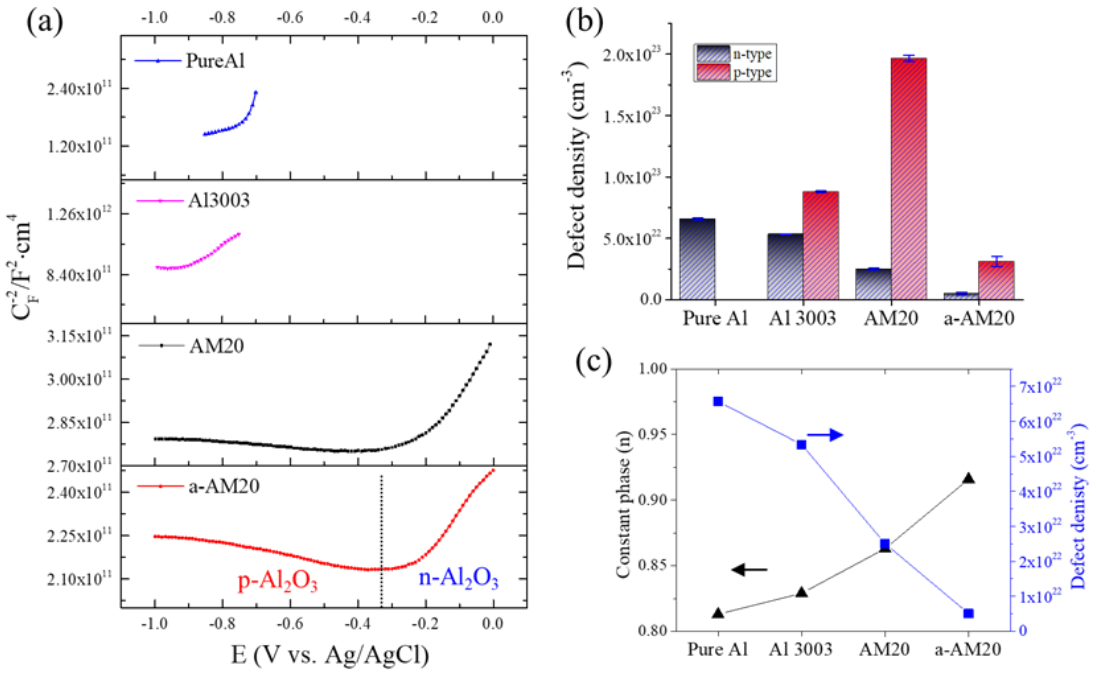

Figure 3.10 (a) Summary of Mott–Schottky plots, (b) defect density, and (c) n-type defects vs. pitting potential Epit of all samples.

The above APT and XPS results have shown that in the surface oxide layer of AM20 and a-AM20, only aluminum (hydr)oxide was present while Mn was present in the non-oxidized metal form (Mn^0), with a decreasing concentration from 20 at.% Mn (bulk concentration) at the metal/oxide interface to zero at the outermost (hydr)oxide surface. In other words, Mn addition enhanced the corrosion resistance of Al without participating in the surface oxidation. To gain a better understanding of the passive layer formation (i.e. oxidation) mechanisms of Al and Al-Mn, additional molecular dynamic

simulations were performed to study the oxidation energetics in collaboration with Jianwei Xiao and Chuang Deng, as shown in Fig. 9-13 in reference [45]. Since crystalline Al, amorphous Al, and amorphous Al-Mn represents a trend of increased Al-Al bond distance and free volume, it is assumed that the trend from crystalline to amorphous Al could be potentially extended to Al-Mn, where the presence of Mn further increased the Al-Al bond distance and free volume but does not participate in the oxidation process. It was confirmed that with an increasing free volume in Al, the density of the oxide layer increases due to the lower activation energy and more oxygen transport pathways.

3.5 Discussion

Corrosion resistance of complex alloys depends heavily on the structure and property of the surface oxide layer. Generally speaking, both the composition and crystal structure of the oxide layer are far from equilibrium in the surface oxide layer of complex alloys. Such complexity makes theory-guided alloy design and selection rather challenging. In the present work, we show that when alloyed with nonpassive element Mn in solid solution, the corrosion resistance of Al was significantly enhanced although Mn is largely absent from the passive layer. Such results cannot be explained by only considering the thermodynamics during corrosion. For example, the calculated potential/pH (Pourbaix) diagram of $Al_{80}Mn_{20}$ is shown in Fig. 3.11 following algorithms in [46, 47]. It can be seen that near neutral pH, the passivity region of $Al_{80}Mn_{20}$ is very similar to pure Al. In other words, the addition of Mn does not increase the passivity region of the alloy because Mn is dissolving/corroding under such pH/potential condition. Due to this reason, the effect of Mn must be related to the corrosion kinetics.

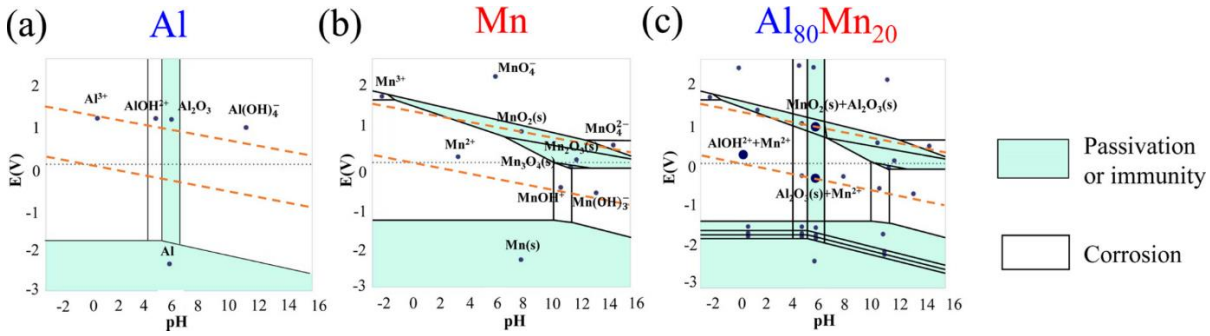

Figure 3.11 Pourbaix diagrams of (a) Al, (b) Mn, and (c) Al80Mn20 alloys.

Specifically, our experimental study shows that increasing Mn% in Al enhanced its pitting resistance and reduced its corrosion rate compared to pure Al. This corrosion protection was further enhanced by anodizing, where the passive film thickness slightly increased, with reduced p-type defect density. Through comprehensive surface characterization, we found that the selective dissolution of Mn facilitates the formation of a thinner oxide layer with closer to stoichiometric composition than that on pure Al. At the same time, the surface depletion of Mn reduces the n-type defect density in the passivation layer that further affects charge transfer and chloride adsorption. MD simulations on crystalline and amorphous Al further confirm that increasing the free volume content and Al-Al bond distance lead to lower activation energy and more O transport pathways of amorphous Al, and hence the formation of a denser oxide layer.

Several observations are interesting: (1) the oxide layer on Al-Mn alloys is thinner than that on pure Al, and the oxide thickness decreases with increasing Mn content (by comparing those on Al 3003 and AM20); (2) the defect type is n-type in pure Al, but p-n junction for all Al-Mn alloys studied. In addition, the total defect density in the alloy is higher at higher Mn%. Such results indicate that the effect of Mn is mostly in reducing mass transport, rather than electronic transport, by forming a more compact oxide layer.

Finally, a simplistic model is proposed in Fig. 3.12 to explain the observed alloying effect by considering an effective Pilling-Bedworth (PB) ratio of a binary alloy and its implications on the structural compatibility between the metal and oxide. For a pure metal, PB ratio is defined as

$$R_{PB} = \frac{volume\ of\ oxide\ produced}{volume\ of\ metal\ produced} = \frac{M_{oxide} \cdot \rho_{metal}}{nM_{metal} \cdot \rho_{oxide}}, \quad (3.3)$$

where M is the atomic or molecular mass, ρ is the density, and n is the number of metal atoms per molecule of the oxide [48]. Now consider a binary alloy of A_mB_n (where m% and n% are the atomic percentage of element A and B respectively). We define an effective PB ratio for the whole alloy as:

$$R_{PB}^{eff} = \sum_{i=1}^{n} x_i R_{PB}^{i}, \quad (3.4)$$

where x_i is the atomic percentage of the passivating element i and R_{PB}^{i} is the corresponding PB ratio. Under a given corrosive environment, each constituting element's passivity can be identified thermodynamically from its Pourbaix diagram. Note here that this calculation does not include the PB ratio of any non-passivating elements in the alloy. We hypothesize that once the alloy composition is optimized to achieve an effective PB ratio close to 1, the naturally formed oxide layer is of the highest protectiveness by having high density and low porosity due to excellent structural compatibility between the oxide and the metal lattices. Note that this parameter is formulated based on structural consideration, hence completely different from the empirical parameters such as pitting resistant equivalent number (PREN) used for steel design [49]. This compact surface oxide layer would be an effective barrier to oxygen diffusion and, as a result, lead to the formation of a thinner oxide layer than those with a higher PB ratio. The three alloys studied here: pure Al, Al 3003 (1.6 at.% Mn), and AM20 (20 at.% Mn), having an R_{PB}^{eff} of 1.33, 1.31 and 1.06, respectively, indeed showed increased corrosion resistance and reduced oxide thickness, supporting our hypothesis. These PB ratios are calculated assuming the formation of α-Al_2O_3 (corundum, trigonal $R\bar{3}c$), as confirmed by XRD results in Fig. 3.2. Interestingly, this simple model can also explain why the pitting potential of Al-Mn starts to decrease when Mn% is above ~ 40 at.% [16], where its R_{PB}^{eff} becomes 0.8, significantly smaller than 1. Hence the formed oxide layer does not have enough volume to completely cover the metal substrate for effective passivation. Such a simplistic model needs future examination, especially from complex alloy systems such as high entropy alloys and

metallic glasses. As a last note, the presence of a thin oxide layer, coupled with enhanced surface activity of Al, could also render a faster repassivation rate if the surface oxide layer is damaged, in agreement with our prior work [10].

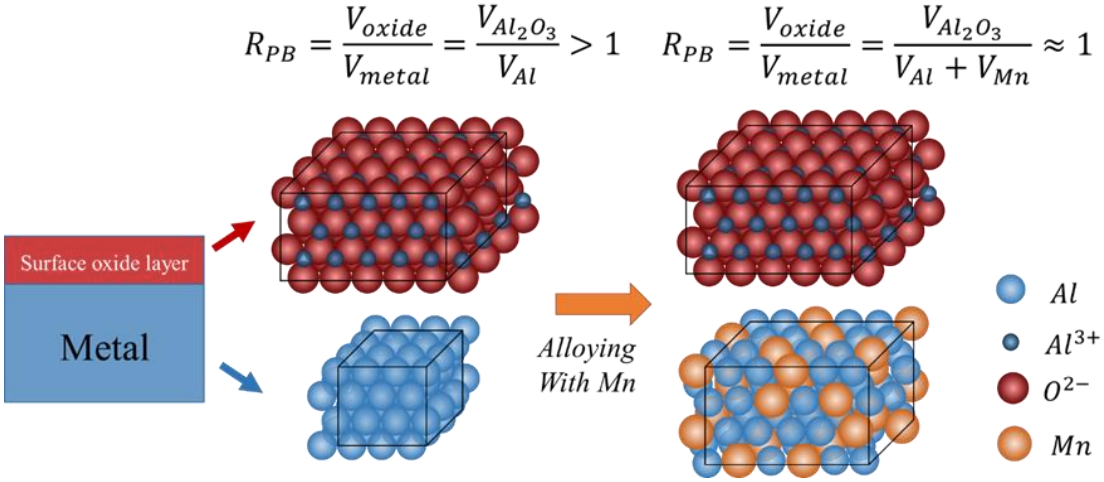

Figure 3.12 Proposed selective solute dissolution model with schematics showing change of PB ratio of Al after alloying with Mn. We hypothesize that the oxide barrier characteristics can be tailored by alloying with non-passivating element (Mn) in solid solution, whose selective dissolution in the surface results in a PB ratio close to 1.

3.6 Conclusions

A synergistic experimental and computational study was carried out to evaluate the effects of a non-passive element, Mn, on the aqueous corrosion behavior of a passive element, Al. It was found experimentally using APT and XPS that the corrosion resistance of Al increased with increasing Mn content (to 20 at.%) in the alloy, despite the fact that Mn does not participate in the surface oxidation process. Although the addition of Mn also changed the defect type and defect density in the oxide layer, its effect on corrosion kinetics is more related to the restriction of mass transport by forming a denser, thinner oxide layer with closer to stoichiometry composition due to the selective dissolution of Mn, resulting in a higher free volume than pure Al. Finally, a simplistic model was proposed to guide future alloy design by considering the optimization of the passive and non-passive element ratio to achieve an optimum effective Pilling-Bedworth ratio of the system.

References

1. Shukla, A. and A. Pelton, *Thermodynamic Assessment of the Al-Mn and Mg-Al-Mn Systems.* Journal of Phase Equilibria and Diffusion, 2009. **30**(1): p. 28-39.
2. Ahmad, Z., *Aluminium Alloys - New Trends in Fabrication and Applications*. 2012.
3. Zamin, M., *The Role of Mn in the Corrosion Behavior of Al-Mn Alloys.* Corrosion, 1981. **37**(11): p. 627-632.
4. Streinz, C.C., et al., *Analysis of Passive Film Growth by Dynamic Imaging Microellipsometry.* Journal of the Electrochemical Society, 1992. **139**(3): p. 711-715.
5. Yu, X.X., et al., *Nonequilibrium Solute Capture in Passivating Oxide Films.* Physical Review Letters, 2018. **121**(14).
6. Kim, Y. and R.G. Buchheit, *A characterization of the inhibiting effect of Cu on metastable pitting in dilute Al-Cu solid solution alloys.* Electrochimica Acta, 2007. **52**(7): p. 2437-2446.
7. Kim, Y., R.G. Buchheit, and P.G. Kotula, *Effect of alloyed Cu on localized corrosion susceptibility of Al-Cu solid solution alloys-Surface characterization by XPS and STEM.* Electrochimica Acta, 2010. **55**(24): p. 7367-7375.
8. Sanchette, F., et al., *Nanostructured aluminium based coatings deposited by electron-beam evaporative PVD.* Thin Solid Films, 2009. **518**(5): p. 1575-1580.
9. Merl, D.K., P. Panjan, and I. Milosev, *Effect of tungsten content on properties of PVD sputtered Al-W-X alloys.* Surface Engineering, 2013. **29**(4): p. 281-286.
10. Mraied, H. and W.J. Cai, *The effects of Mn concentration on the tribocorrosion resistance of Al-Mn alloys.* Wear, 2017. **380-381**: p. 191-202.
11. Mraied, H., W.J. Cai, and A.A. Sagues, *Corrosion resistance of Al and Al-Mn thin films.* Thin Solid Films, 2016. **615**: p. 391-401.
12. Creus, J., et al., *Reactivity classification in saline solution of magnetron sputtered or EBPVD pure metallic, nitride and Al-based alloy coatings.* Corrosion Science, 2012. **57**: p. 162-173.

13. Szklarska-Smialowska, Z., *Pitting corrosion of aluminum.* Corrosion Science, 1999. **41**(9): p. 1743-1767.
14. Gudic, S., I. Smoljko, and M. Kliskic, *The effect of small addition of tin and indium on the corrosion behavior of aluminium in chloride solution.* Journal of Alloys and Compounds, 2010. **505**(1): p. 54-63.
15. Principe, E.L., B.A. Shaw, and G.D. Davis, *Role of oxide/metal interface in corrosion resistance: Al-W and Al-Mo systems.* Corrosion, 2003. **59**(4): p. 295-313.
16. Reffass, M., et al., *Corrosion behaviour of magnetron-sputtered Al1-x-Mn-x coatings in neutral saline solution.* Corrosion Science, 2010. **52**(11): p. 3615-3623.
17. Li, J.C., S.H. Nan, and Q. Jiang, *Study of the electrodeposition of Al-Mn amorphous alloys from molten salts.* Surface & Coatings Technology, 1998. **106**(2-3): p. 135-139.
18. Ruan, S.Y. and C.A. Schuh, *Electrodeposited Al-Mn alloys with microcrystalline, nanocrystalline, amorphous and nano-quasicrystalline structures.* Acta Materialia, 2009. **57**(13): p. 3810-3822.
19. Frankel, G.S., et al., *On the Pitting Resistance of Sputter-Deposited Aluminum-Alloys.* Journal of the Electrochemical Society, 1993. **140**(8): p. 2192-2197.
20. Moffat, T.P., G.R. Stafford, and D.E. Hall, *Pitting Corrosion of Electrodeposited Aluminum-Managanese Alloys.* Journal of the Electrochemical Society, 1993. **140**(10): p. 2779-2786.
21. Zhang, J.F., et al., *Corrosion behaviors of Zn/Al-Mn alloy composite coatings deposited on magnesium alloy AZ31B (Mg-Al-Zn).* Electrochimica Acta, 2009. **55**(2): p. 560-571.
22. Frankel, G.S., *Pitting corrosion of metals - A review of the critical factors.* Journal of the Electrochemical Society, 1998. **145**(6): p. 2186-2198.
23. Crossland, A.C., et al., *Formation of manganese-rich layers during anodizing of Al-Mn alloys.* Corrosion Science, 1999. **41**(10): p. 2053-2069.

24. Eder, K., et al., *Nanoscale Analysis of Corrosion Products: A Review of the Application of Atom Probe and Complementary Microscopy Techniques.* Jom, 2018. **70**(9): p. 1744-1751.

25. La Fontaine, A., et al., *Atom probe study of chromium oxide spinels formed during intergranular corrosion.* Scripta Materialia, 2015. **99**: p. 1-4.

26. Hudson, D., G.D.W. Smith, and B. Gault, *Optimisation of mass ranging for atom probe microanalysis and application to the corrosion processes in Zr alloys.* Ultramicroscopy, 2011. **111**(6): p. 480-486.

27. Chernyakova, K., et al., *Effect of Joule Heating on Formation of Porous Structure of Thin Oxalic Acid Anodic Alumina Films.* Journal of the Electrochemical Society, 2018. **165**(7): p. E289-E293.

28. Thompson, K., et al., *In situ site-specific specimen preparation for atom probe tomography.* Ultramicroscopy, 2007. **107**(2-3): p. 131-139.

29. Huang, Y.L., et al., *Evaluation of the corrosion resistance of anodized aluminum 6061 using electrochemical impedance spectroscopy (EIS).* Corrosion Science, 2008. **50**(12): p. 3569-3575.

30. Zuo, Y., P.H. Zhao, and J.M. Zhao, *The influences of sealing methods on corrosion behavior of anodized aluminum alloys in NaCl solutions.* Surface & Coatings Technology, 2003. **166**(2-3): p. 237-242.

31. Merl, D.K., P. Panjan, and J. Kovac, *Corrosion and surface study of sputtered Al-W coatings with a range of tungsten contents.* Corrosion Science, 2013. **69**: p. 359-368.

32. Gonzalez, J.A., et al., *Characterization of porous aluminium oxide films from ac impedance measurements.* Journal of Applied Electrochemistry, 1999. **29**(2): p. 229-238.

33. Vurpillot, F., D. Larson, and A. Cerezo, *Improvement of multilayer analyses with a three-dimensional atom probe.* Surface and Interface Analysis, 2004. **36**(5-6): p. 552-558.

34. Dyck, O., et al., *Accurate Quantification of Si/SiGe Interface Profiles via Atom*

Probe Tomography. Advanced Materials Interfaces, 2017. **4**(21).

35. Chen, J. and W.J. Cai, *Effect of scratching frequency on the tribocorrosion resistance of Al-Mn amorphous thin films.* Wear, 2019. **426**: p. 1457-1465.
36. Zhang, B., Y. Li, and F.H. Wang, *Electrochemical corrosion behaviour of microcrystalline aluminium in acidic solutions.* Corrosion Science, 2007. **49**(5): p. 2071-2082.
37. Hamdy, A.S., E. El-Shenawy, and T. El-Bitar, *Electrochemical Impedance Spectroscopy Study of the Corrosion Behavior of Some Niobium Bearing Stainless Steels in 3.5% NaCl.* International Journal of Electrochemical Science, 2006. **1**(4): p. 171-180.
38. de Oliveira, M.C.L., et al., *Correlation between the corrosion resistance and the semiconducting properties of the oxide film formed on AZ91D alloy after solution treatment.* Corrosion Science, 2013. **69**: p. 311-321.
39. Lv, J.L. and H.Y. Luo, *Comparison of corrosion properties of passive films formed on phase reversion induced nano/ultrafine-grained 321 stainless steel.* Applied Surface Science, 2013. **280**: p. 124-131.
40. Mibus, M., et al., *Improving dielectric performance in anodic aluminum oxide via detection and passivation of defect states.* Applied Physics Letters, 2014. **104**(24).
41. Liang, D.D., et al., *Effects of W Addition on the Electrochemical Behaviour and Passive Film Properties of Fe-Based Amorphous Alloys in Acetic Acid Solution.* Acta Metallurgica Sinica-English Letters, 2018. **31**(10): p. 1098-1108.
42. Amri, J., et al., *Effect of the final annealing of cold rolled stainless steels sheets on the electronic properties and pit nucleation resistance of passive films.* Corrosion Science, 2008. **50**(2): p. 431-435.
43. Wang, T., et al., *Homogeneous Cu2O p-n junction photocathodes for solar water splitting.* Applied Catalysis B-Environmental, 2018. **226**: p. 31-37.
44. Macdonald, D.D., *Passivity - the key to our metals-based civilization.* Pure and Applied Chemistry, 1999. **71**(6): p. 951-978.

45. Chen, J., et al., *The origin of passivity in aluminum-manganese solid solutions.* Corrosion Science, 2020. **173**.

46. Persson, K.A., et al., *Prediction of solid-aqueous equilibria: Scheme to combine first-principles calculations of solids with experimental aqueous states.* Physical Review B, 2012. **85**(23).

47. Singh, A.K., et al., *Electrochemical Stability of Metastable Materials.* Chemistry of Materials, 2017. **29**(23): p. 10159-10167.

48. *Pourbaix,M - Atlas of Electrochemical Equilibria in Aqueous Solutions.* Anti-Corrosion, 1967. **14**(2): p. 28-&.

49. Tan, H., et al., *Effect of annealing temperature on the pitting corrosion resistance of super duplex stainless steel UNS S32750.* Materials Characterization, 2009. **60**(9): p. 1049-1054.

Chapter 4:

Effects of Alloying Concentration on the Corrosion and Tribocorrosion of Aluminum-Manganese-Molybdenum Concentrated Alloys

Jia Chen[a], Jianwei Xiao[b], Chang-Yu Hung[a], Wenbo Wang[a], Jing Zhao[c], F. Marc Michel[c], Chuang Deng[b,*], and Wenjun Cai[a,*]

a Department of Materials Science and Engineering, Virginia Polytechnic Institute and State University, Virginia, 24061, United States

b Department of Mechanical Engineering, University of Manitoba, Winnipeg, MB R3T 5V6, Canada

c Department of Geosciences, Virginia Polytechnic Institute and State University, Virginia, 24061, United States

*Corresponding author E-mail addresses: Chuang.Deng@umanitoba.ca, caiw@vt.edu.

Declarations of interest: none

*This chapter has been adapted from a manuscript with **submission** in Corrosion Science.*

4.1 Abstract

The effects of alloying concentration on the aqueous corrosion behavior of aluminum-manganese-molybdenum (Al-Mn-Mo) alloys with 8-20 at.% Mn and 0-30 at.% Mo were investigated by experiments and atomistic simulations. The pitting potential and corrosion current density of Al-Mn-Mo were found to increase with Mo%. The passive film thickness depended on the total alloy concentration, while its compactness and defect density on the individual ones. Specifically, $Al_{80}Mn_8Mo_{12}$ exhibited higher corrosion resistance than $Al_{80}Mn_{20}$ due to the formation of a more compact and less defective passive film, as explained by the roles Mo played in both the substrate and the passive film. It is also noted that the current density of the worn area increased with increasing Mo content.

4.2 Introduction

Critical technologies in the fields of aerospace industries, transportation, biomedical, and wearable devices etc. require low density structural materials to operate reliably under corrosive environment [1-3]. These extreme conditions are testing the limits of existing materials and demanding the development of new high-performance metals that could maintain structural integrity under combined stress and corrosion over the long term. The design of strong and corrosion resistant lightweight alloys is challenged as composition and microstructure govern strength and corrosion resistance in different ways [4-6]. Prevalent precipitation strengthening mechanisms in lightweight alloys (e.g. Al alloys) lead to compromised corrosion resistance due to the micro-galvanic coupling between the precipitates (local cathodes) and the substrate (local anode). For example, ultra-high purity Al exhibit much lower corrosion rate compared to most commercial Al alloys despite its low mechanical properties [7].

To overcome the tradeoff between strength and corrosion resistance in lightweight alloys, it is critical to identify *'electrochemically benign'* strengthening mechanisms. Such mechanisms would strengthen the material without introducing significant

chemical heterogeneity. Precipitation strengthening would be an example of undesirable *'electrochemically hostile'* mechanism. It should also be pointed out that if only mild heterogeneity (e.g. nanoscale compositional wavelength and coherent interfaces) was introduced during precipitation, such as during spinodal decomposition or GP zone formation [8], such mechanism should be considered as more 'benign' than 'hostile'. Solid solution strengthening, on the other hand, is an *'electrochemically benign'* mechanism. For example, it was found that even the traditionally corrosion-detrimental alloying elements such as Cu could enhance corrosion resistance of Al as long as it remains in solid solution [9, 10]. Thus, to simultaneously enhance corrosion and strength, it is desirable to form *lightweight concentrated alloys (LCAs)*, where the high solute concentrations (typically above ~ 5 at.%) in solution strengthen the material, without compromising corrosion resistance. Examples of such LCAs include Al-based supersaturated solid solutions [11-15], metallic glasses [16-19], and emerging lightweight high entropy alloys such as AlBeFeSiTi [20], AlTiVCr [21, 22], AlNbTiV [23], and AlCrNbTiV [24] etc.

The effects of alloying additions on corrosion resistance of Al-based LCAs are much more complex than conventional alloys and poorly understood. Firstly, contradictory behaviors are often reported in terms of the roles played by individual alloying element. For example, the addition of Y was found to enhance corrosion resistance of Al-Y alloys but decrease corrosion resistance in Zr-Al based metallic glasses [25, 26]. Similarly, Al addition was found to be beneficial for corrosion resistance in AlxCrFeMoV [27] but detrimental in AlxCrFeMnNi system [28]. Secondly, the optimum alloy concentration for the best corrosion resistance is not known *a priori* [29]. Thirdly, the trend of pitting potential could be opposite to that of corrosion current. For example, increasing Y content from 9% to 11% in Al-Y lead to a reduction of both corrosion current and pitting potential [25]. Fourthly, the high alloying concentration could lead to oxidation of non-passive element against thermodynamics predictions [25]. Lastly, in complex alloys, not all elements participate in oxide formation, but sometimes the surface enrichment of certain non-oxidizing

element enhances the barrier characteristics of the passive layer through a poorly understood mechanism [21].

To better understand the corrosion resistance of Al-based LCAs and the effects of alloying concentrations on the structure and property of the passive layer, specifically, this work aims to study the effects of a passive element (Mo) and non-passive element (Mn) on the corrosion behavior of Al-Mn-Mo LCAs. In our previous work [30], the roles of Mn on the origin of passivity in Al-Mn alloys in 0.6 M NaCl solution were investigated. It was found that Mn can significantly improve the corrosion resistance of aluminum. The selective dissolution of Mn is thought to increase the free volume of the metal/oxide interface, promoting the formation of a denser, thinner, and more protective passive film. Structurally, higher Mn leads to a transition from single phase face-centered-cubic (FCC) at low Mn% to complete amorphous structure when Mn% is above ~ 20 at.% [31]. Nonetheless, corrosion resistance increases monotonically with Mn% up to ~ 41% as long as Mn remains in homogenous solid solution with Al [32]. Similar to Mn, the equilibrium solubility of Mo in Al at low temperatures is very low. Thus in traditionally cast or wrought Al alloys, the addition of Mo generally leads to precipitate formation and reduces the pitting resistance of the alloy [33]. When Mo is alloyed with Al in single phase solid solution, stable passivity and excellent corrosion resistance of Al-Mo (up to 45% Mo) in chloride-containing solution has been reported [34-37]. However, the specific roles played by Mo, its presence or absence in the passive film and charge state were poorly understood. Some studies [35, 38-40] showed that Mo improved the pitting potential of Al alloys by forming a Mo enrichment layer underneath the passive film, while others [41] found no Mo enrichment at the oxide/metal interface of Al-Mo after corrosion in near-neutral pH chloride environment.

To address the above questions and provide a better understanding of the alloying effects, in this work, Al-Mn-Mo concentrated alloys with Mo% from 0 to 30 at.% and Mn% from 8 to 20 at.% were fabricated by sputtering deposition. The corrosion behaviors of these LCAs were measured by electrochemical measurements, and the as-deposited and corroded microstructure characterized by X-ray diffraction (XRD),

scanning electron microscopy (SEM) and transmission electron microscopy (TEM). Specifically, an optimum alloying concentration was identified, and the roles Mo played in affecting the passivity of Al-Mn-Mo was discussed based on X-ray photoelectron spectroscopy (XPS) and Mott-Schottky measurements, and molecular dynamics (MD) simulation results.

4.3 Methods and Materials

4.3.1 Materials synthesis and characterization

Al-Mn-Mo thin films were produced by direct current (DC) magnetron deposition on (100) silicon wafers in a vacuum chamber (PVD 75, Kurt J. Lesker, Pennsylvania, USA) under 5.7×10^{-3} Torr argon atmosphere (99.99%). Prior to the deposition, Si wafers were etched by hydrofluoric acid water solution (1:20) to remove the natural formed oxide layer. The chamber was purged for at least three times by flowing Ar gas to minimize oxygen contamination, followed by silicon wafer cleaning via Ar plasma. The composition of all samples is listed in Table 4.1, which was controlled by tuning the power of two targets (see Table 4.2) during deposition. Specifically, Al-Mn was synthesized using Al (99.99 %) and Mn (99.99 %) targets, while Al-Mn-Mo using Al and AlMnMo (equal atomic composition, 99.95%) targets, all purchased from Kurt J. Lesker, Pennsylvania, USA. The thickness of all thin film samples was in the range of ~ 1.2 - 1.5 μm, measured by a surface profilometer (DektakXT, Bruker, Massachusetts, USA). The composition was found to be homogenous of all samples, as measured by a scanning electron microscopy (SEM, Quanta 600 FEG, FEI, Oregon, USA) equipped with energy-dispersive X-ray spectroscopy (EDS, Quantax, Bruker, Massachusetts, USA) at 10 keV.

Table 4.1 Composition, diffraction angle and calculated d-spacing of all samples.

Sample ID	Nominal composition	Al (at.%)	Mn (at.%)	Mo (at.%)	θ (°)	d-spacing (Å)
A	$Al_{80}Mn_{20}$	79.6 ± 1.6	20.4 ± 1.5	-----	21.28	4.24
B	$Al_{80}Mn_8Mo_{12}$	79.2 ± 0.4	8.4 ± 0.1	12.4 ± 0.3	20.70	4.36
C	$Al_{65}Mn_{13}Mo_{22}$	66.1 ± 1.4	12.7 ± 0.5	21.2 ± 0.9	20.65	4.37
D	$Al_{58}Mn_{15}Mo_{27}$	58.6 ± 1.2	14.3 ± 0.4	27.1 ± 0.8	20.70	4.36
E	$Al_{52}Mn_{18}Mo_{30}$	52.2 ± 1.1	18.0 ± 0.3	29.8 ± 0.9	20.50	4.40

Table 4.2 Summary of the dual target powers used during PVD deposition.

Sample	Al target (Watts)	Mn target (Watts)	AlMnMo target (Watts)
$Al_{80}Mn_{20}$	200	40	----
$Al_{80}Mn_8Mo_{12}$	200	----	50
$Al_{65}Mn_{13}Mo_{22}$	200	----	100
$Al_{58}Mn_{15}Mo_{27}$	200	----	150
$Al_{52}Mn_{18}Mo_{30}$	200	----	200

The as-deposited samples were characterized by using grazing incidence X-ray diffraction (GI-XRD) (PANalytical Empyrean Nano Edition) with Cu Kα radiation under 45 kV and 40 mA condition. The grazing incidence angle was 0.8° with 0.01° step size and 10 s scan step. The measurements were performed from 30° to 90° in 2θ configuration. The surface morphology before and after corrosion tests were examined by using SEM and the surface composition by EDS. Selected samples were characterized by TEM (JEOL JEM 2100, Tokyo, Japan) in the bright-field, dark-field, and selected area diffraction (SAD) modes. The TEM samples were prepared by the standard lift-out method using focused ion beam (FIB, FEI Helios 600 NanoLab, USA), the sample surface was coated by a total of ~ 4 μm Pt layer (including e-beam followed by ion beam deposition) to prevent Ga ion damage during ion milling.

4.3.2 Electrochemical test

Prior to electrochemical tests, all sample were prepared with ~ 1 cm^2 exposed area by using a protective stop-off lacquer. The electrochemical measurements were performed in naturally aerated 0.6 M NaCl solution with pH≈6.4 at room temperature

using a potentiostat/galvanostat/zero resistance ammeter (Gamry model 600, Pennsylvania, USA). A three-electrode setup was used for all electrochemical measurements. The working electrode (W.E.) was the test sample whereas the counter and reference electrodes (R.E.) were activated titanium mesh and silver-silver chloride 1 M KCl, respectively. Samples were stabilized at open circuit potential (E_{ocp}) for 20 hrs before all tests. Potentiodynamic polarization (PD) tests were performed by sweeping the potential from -200 mV below E_{ocp} at a scan rate of 0.167 mV/s and terminated when the corrosion current reaches 10^{-4}~10^{-3} A/cm^2. The electrochemical impedance spectroscopy (EIS) analysis was conducted at E_{ocp} within a frequency range of 100 kHz to 10 mHz with 10 mV_{rms} sinusoidal potential excitation. The obtained EIS data was fitted with an equivalent circuit (EC) model by using Gamry E-chem software. The electronic properties of the passive layer of all samples were analyzed by Mott-Schottky (M-S) method at a frequency of 1,000 Hz at a scanning rate of 10 mV/s, from 100 mV above E_{ocp} till 100 mV below the pitting potential of each sample.

4.3.3 Tribocorrosion test

The tribocorrosion test was performed in 0.6 M sodium chloride aqueous solution at room temperature using a multifunctional tribometer (Rtec, CA, USA) connected with Gamry model 600. The electrochemical part was a three-electrode setup as well. An alumina ball (Al_2O_3, 4mm diameter) was used as the counter body for the tribocorrosion test. Each test was performed by applying a 0.5 N normal force, 5mm scratch length, at a constant frequency of 1 Hz in linear reciprocal motion. An anodic potential of 200 mV (within the passive region) vs. Ag/AgCl above open circuit potential was applied during tribocorrosion. Prior to each tribocorrosion test, the open circuit potential was first stabilized for 1500 s. Then the tribocorrosion test was performed for 120 s by applying a normal load of 0.5 N. When the test finished, the indenter ball was removed, and the sample still remained in electrolyte until reached to 2,000 s. Post-tribocorrosion analysis was performed by SEM equipped with EDS.

4.3.4 Post-corrosion X-ray photoelectron spectroscopy analysis

The corroded surface was characterized by using X-ray photoelectron spectroscopy (XPS, PHI Quantera SXM, USA) in an ultra-high vacuum of 10^{-9} Torr. The depth-profile curve of each sample was measured using a monochromatic Al Kα X-ray source with a spot size of 100 μm and a 45° angle source analyzer. To remove potential carbon contamination, 1 kV primary ion source was used to pre-sputter the sample surface for 10 s. The sputtering depth curve was obtained by a number of sweeps, step sizes and pass energy as listed in Table 4.3, with 1-3 kV argon ion over an area of ~ 2×2 mm^2. The A1 2p, Mn 2p, Mo 3d and O 1s core levels obtained at the step size of 0.1-0.125 eV were used for quantitative analysis. The estimated instrument resolution is ~ 0.39 eV for O 1s spectrum, ~ 1.0 eV for Al 2p spectrum, and ~ 2.1 eV for Mn 2p and Mo 3d spectrum. Before analyzing the data, the spectra were calibrated using C 1s at 285 eV. After curve fitting, the spectral deconvolution was performed using Multipak analysis software.

Table 4.3 Summary of XPS parameters used in sputter depth profiling

Element	Number of sweeps	Step size (eV)	Passage energy (eV)
Al 2p	8	0.125	69
Mn 2p	8	0.125	140
Mo 3d	8	0.125	140
O 1s	6	0.1	26

4.4 Results and discussion

4.4.1 Microstructure characterization of as-deposited samples

Fig. 4.1 shows the GI-XRD diffraction patterns of all as-deposited samples. Previous work shows in binary Al-Mn solid solutions, a complete amorphous phase forms at Mn% above ~ 15 - 18% [31, 32], showing a broad peak around 42 - 43° from XRD [30]. As shown in Fig. 4.1, comparing XRD patterns of $Al_{80}Mn_{20}$ vs. $Al_{80}Mn_8Mo_{12}$, replacing 12 at.% Mn with Mo led to a slight left shift of the diffraction angles (triangle marks in Fig. 4.1), indicating a slight increase of the average

interatomic distance (d-spacing shown in Table 4.1), likely due to the slightly larger atomic radii (r) of Mo than Mn (r_{Mo}/r_{Mn}=1.18). In all ternary alloys studied, the diffraction angles (θ) remained almost constant, as shown in Table 4.1, and d was calculated by Bragg's law as $n\lambda = dsin\theta$, where the diffraction order n=1, and the wavelength λ=1.5406 Å for Cu Kα. In addition to the main diffraction peak, a small peak at $2\theta \approx$ 34-36° was observed in $Al_{80}Mn_{20}$ and $Al_{80}Mn_8Mo_{12}$ samples, which was close to the (104) diffraction peak (~ 35.14°) of corundum (α-Al_2O_3) (JCPDS-ICDD File No 46-1212). It is noted that amorphous alumina is produced almost instantaneously on Al and its alloys in any oxygen containing environment at low temperatures. Once the thickness of this layer exceeds a critical value [42], e.g. 0.5 nm for (111), 2.5 nm for (100), and 5 nm for (110) planes, it transforms to its crystalline allotropes following: amorphous alumina $\rightarrow \gamma \rightarrow \delta \rightarrow \theta \rightarrow \alpha$. These results thus indicate that the naturally formed oxide layer on $Al_{80}Mn_{20}$ and $Al_{80}Mn_8Mo_{12}$ samples are thicker than those on the other ternary alloys, likely due to their higher Al% (80 at.%), which is indeed consistent with the XPS results (Fig. 4.7) as detailed later in section 4.4.3. Nonetheless, our previous work indicates that a thicker oxide layer does not guarantee a higher corrosion resistance in Al alloys [30].

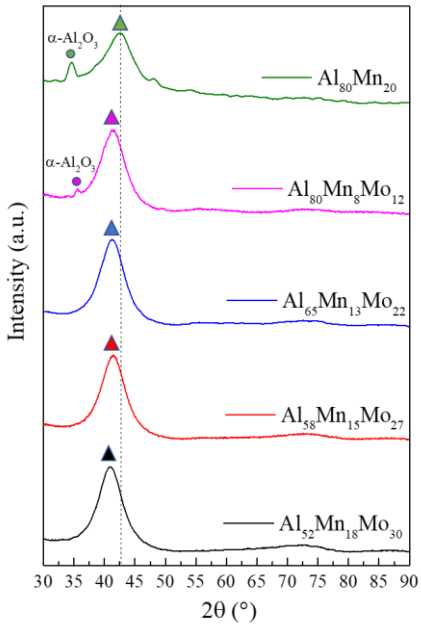

Figure 4.1 GI-XRD patterns of all as-deposited samples.

In addition to XRD, TEM analysis was performed for a selected sample, $Al_{52}Mn_{18}Mo_{30}$, to reveal the microstructure, as shown in Fig. 4.2. HRTEM image in Fig. 4.2(a) shows that the majority of the sample was amorphous with a diffuse halo in the FFT pattern (Fig. 4.2(a) inset). However, occasional crystalline diffraction was also observed, as shown in the SAD pattern in Fig. 4.2(b), indicating the presence of a small fraction of nanocrystalline phases of 50 -100 nm (as revealed by the dark-field images), which was not detected by XRD. It is also noted that the bright and dark areas shown in the bright-field image in Fig. 4.2(b) have almost identical compositions, which was confirmed by EDS analysis (results not shown here). These XRD and TEM results thus indicated that the amorphous phase was dominating in Al-Mn-Mo alloys, with occasional presence of nanocrystalline phases. Fig. 4.3(a)-(e) show the surface SEM images of all as-deposited samples. In all cases, a smooth and featureless surface was observed, indicating the formation of ultrafine microstructure, in agreement with the XRD and TEM results.

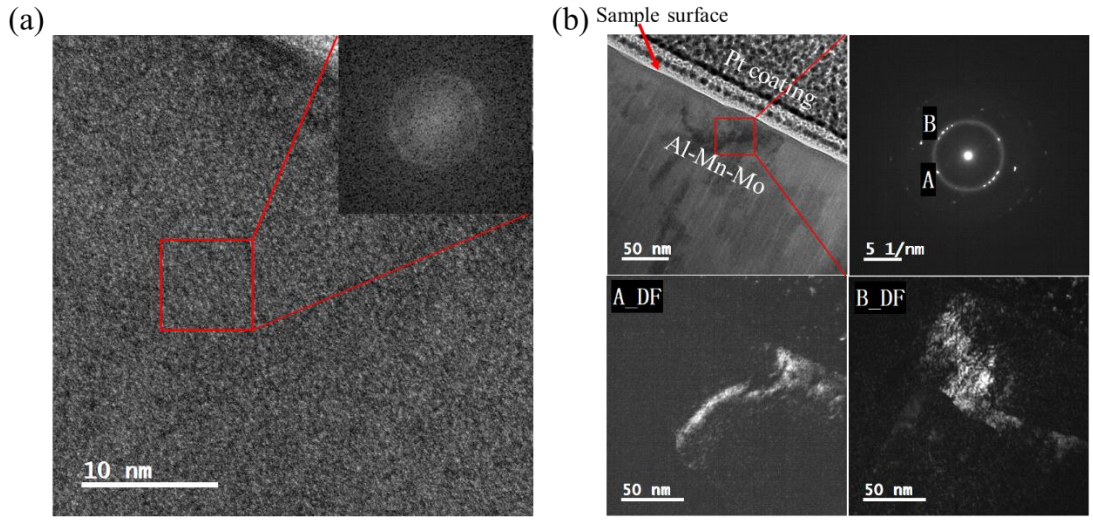

Figure 4.2 (a) High resolution TEM image and (b) bright-field (top left), SAD (top right), and dark-field (bottom) images of as-deposited Al52Mn18Mo30 thin film. Inset in (a) is the FFT image of the box area in (a).

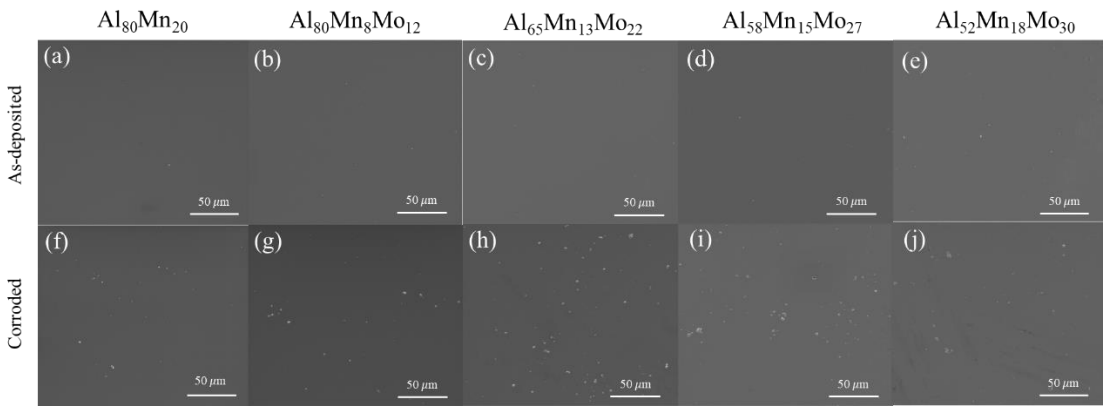

Figure 4.3 The surface SEM images of all samples before and after PD corrosion tests.

4.4.2 Corrosion behavior

Fig. 4.4(a) shows the time evolution of E_{ocp} for all samples during immersion test over 20 hrs. The potential increased from its initial value quickly towards a steady-state value after 5,000 sec for all samples, likely due to the rapid formation of the passive film in neutral pH solutions. The E_{ocp} value of Al-Mn (~ -1.29 V vs. Ag/AgCl) and all Al-Mn-Mo alloys (-0.435−-0.523 V vs. Ag/AgCl) were quite different, with those of Al-Mn-Mo alloys ~ 0.8 V nobler. According to the standard electromotive force (EMF) series, the equilibrium potential (vs. SHE) is -1.66 V for $Al|Al^{3+}$ (vs. SHE), -1.18 V for $Mn|Mn^{2+}$, and -0.2 V for $Mo|Mo^{3+}$. Thus, the incorporation of Mo in the alloy tends to increase the corrosion potential of Al. Indeed, $Al_{52}Mn_{18}Mo_{30}$ exhibited the highest E_{ocp} among all samples.

Fig. 4.4(b) shows the PD curves of all samples. It can be seen that in general, the ternary Al-Mn-Mo samples have higher pitting potential (E_{pit}) and corrosion potential (E_{corr}) than those of the binary Al-Mn sample. Specifically, E_{pit} increased from -0.16 V for $Al_{80}Mn_{20}$ to 0.49 V for $Al_{52}Mn_{18}Mo_{30}$, with the later even higher than that of 304 stainless steels (~ 0.333 V) [43]. In terms of the corrosion current density (i_{corr}), with the exception of $Al_{80}Mn_8Mo_{12}$ (sample B), all ternary alloys exhibited higher i_{corr} than $Al_{80}Mn_{20}$, and i_{corr} increased from samples B to E. It is interesting to note here that, comparing the results of $Al_{80}Mn_{20}$ (sample A) and $Al_{80}Mn_8Mo_{12}$ (sample B), the corrosion current was lower and the pitting potential higher in the latter. Overall, the optimum concentration for a high E_{pit} and low i_{corr} in the Al-Mn-Mo ternary system

studied here was $Al_{80}Mn_8Mo_{12}$, from which further reducing Mo% will decrease the E_{pit}, while increasing Mo% will increase i_{corr}. More discussion of this behavior will be provided in sections 4.6.

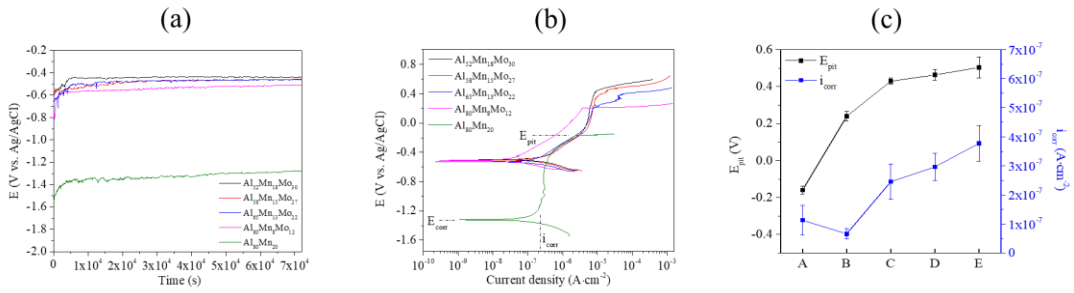

Figure 4.4 Summary of (a) time evolution of open circuit potential, (b) PD curves, (c) pitting potentials (E_{pit}) and corrosion current densities (i_{corr}) of all samples measured from PD tests in 0.6 M NaCl solution.

Fig. 4.3(f)-(j) shows the SEM images of the corroded surfaces of all samples after PD tests. The corrosion product density, defined as number of corrosion particles/area, is slightly higher in $Al_{65}Mn_{13}Mo_{22}$ (14 particles/1000 μm^2) than that of the other samples (3-9 particles/1000 μm^2). The corrosion particle size of all samples is similar, as shown in the particle size distribution in Fig. 4.5. A slightly higher oxygen content was present in all corrosion products as compared to the rest of the surface, as shown in Table 4.4. The thickness of the passive film on a selected sample: $Al_{52}Mn_{18}Mo_{30}$, was measured to be around 11.9 nm by cross-sectional TEM (Fig. 4.6). As discussed later in section 4.4.3, this slayer is primally composed of alumina, thus leading to the higher O content measured at the surface.

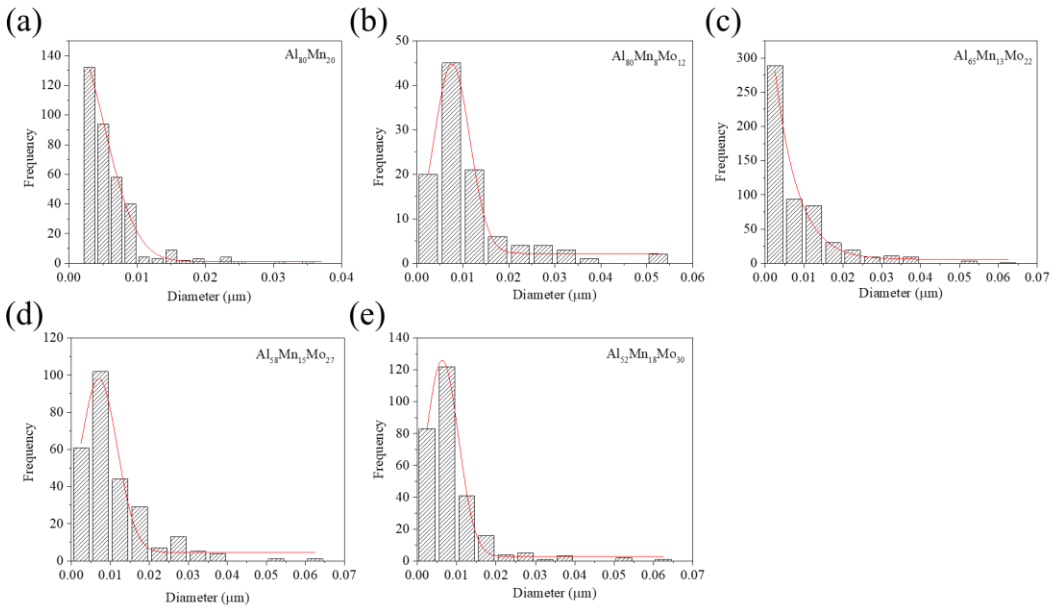

Figure 4.5 The size distribution of corrosion particles on the surface of all samples after PD test.

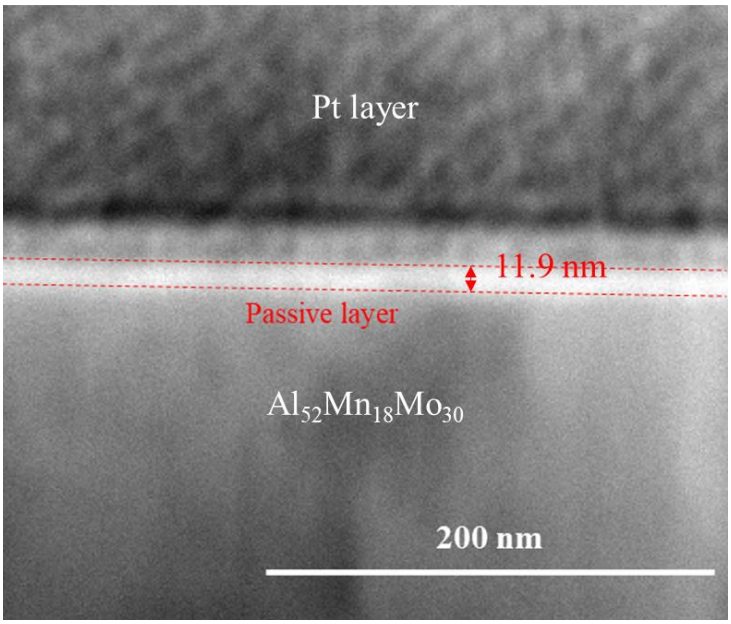

Figure 4.6 Bright-field TEM image of the cross-section of $Al_{52}Mn_{18}Mo_{30}$ alloy after PD test.

Table 4.4 Summary of surface and corrosion product composition of corroded samples as measured by EDS.

Sample	Surface (at.%)				Corrosion products (at.%)			
	Al	Mn	Mo	O	Al	Mn	Mo	O
$Al_{80}Mn_{20}$	75.6 ± 0.7	20.6 ± 0.6	---	3.8 ± 0.4	73.5 ± 0.9	21.8 ± 0.3	---	4.8 ± 0.6
$Al_{80}Mn_8Mo_{12}$	73.5 ± 0.2	7.8 ± 0.6	13.0 ± 1.1	5.7 ± 0.5	73.0 ± 1.6	7.6 ± 0.2	12.7 ± 0.7	6.8 ± 1.0
$Al_{65}Mn_{13}Mo_{22}$	57.1 ± 0.7	12.3 ± 0.6	21.4 ± 0.3	9.2 ± 0.4	54.7 ± 1.2	11.8 ± 0.2	22.4 ± 1.3	11.2 ± 0.1
$Al_{58}Mn_{15}Mo_{27}$	49.3 ± 0.9	13.9 ± 0.6	26.0 ± 0.04	10.7 ± 0.3	45.5 ± 0.2	13.2 ± 0.6	27.0 ± 0.3	14.4 ± 0.5
$Al_{52}Mn_{18}Mo_{30}$	45.6 ± 0.6	16.0 ± 0.9	29.9 ± 0.9	8.5 ± 0.7	43.8 ± 0.5	15.4 ± 0.2	29.7 ± 0.6	11.2 ± 0.6

The EIS results are summarized in Fig. 4.7. Fig. 4.7(a) shows that the diameter of the capacitive semicircle for $Al_{80}Mn_8Mo_{12}$ is larger than all other samples, consistent with the PD results. Further increasing Mo from 12 to 30 at.% and Mn from 8 to18 at.%, the diameter of semicircle reduced monotonically. One of several possible equivalent circuits that can fit the EIS data was shown in Fig. 4.7(b), where R_s is the ohmic solution resistance, R_p denotes the polarization resistance, CPE is the constant phase element, which accounts for the non-ideal capacitive behavior of the double layer and (possibly) the passive layer. The impedance response of CPE, Z_{CPE}, is defined as:

$$Z_{CPE} = (j\omega)^{-n}/Y_0, \tag{4.1}$$

where j is the imaginary unit, ω is the angular frequency of the sinusoidal signal, Y_0 is the numerical value of the admittance (1/|Z|) at ω =1 rad/s, and n (0≤n≤1) is an exponent equaling 1 for a pure capacitor and zero for a pure resistor. The effective capacitance (C) of the CPE is calculated as:

$$C_{CPE} = Y_0(\omega_{max})^{n-1}, \tag{4.2}$$

where ω_{max} is the angular frequency at which the imaginary part of impedance has its maximum [44]. The model fitting parameters are summarized in Table 4.5. It can be seen that the values of R_p and n in $Al_{80}Mn_8Mo_{12}$ are the highest, showing its higher charge transfer resistance and a more ideal capacitor behavior than other samples. The thickness of the passive film was not calculated in this work, due to the unknown dielectric constant of Al_2O_3 doped with Mo oxide. The Bode plots of all samples are shown in Fig. 4.7(c) and (d). At lower frequencies, the polarization resistance of $Al_{80}Mn_8Mo_{12}$ can be confirmed as the highest one, in agreement with prior results. At high frequencies, the electrolyte resistance R_s was ~15 - 56 Ω, where the variation could

be related to different metal dissolution during E_{ocp} stabilization. In Fig. 4.7(d), the phase shift as a function of the frequency showed that the phase angle of $Al_{80}Mn_8Mo_{12}$ sample was closer to -90° than all other samples, confirming its more ideal capacitive response.

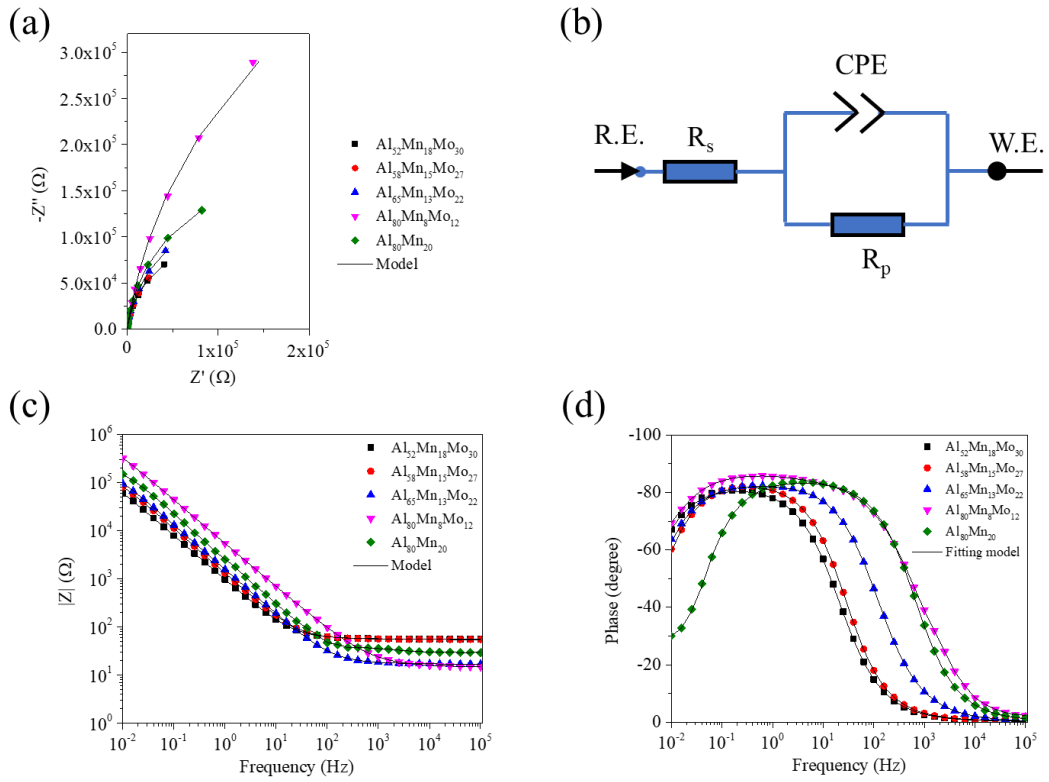

Figure 4.7 Summary of EIS measurements of all samples tested in 0.6 M NaCl solution at open circuit potential. (a) Nyquist plot of measured (scattered symbols) and fitted (lines) impedance via the equivalent circuit model shown in (b). Bode plot of the (c) impedance magnitude and (d) phase shift angle as a function of the frequency.

Table 4.5 The fitting parameters of EC model for all samples as shown in Fig. 4.6(b) and defined in eqns. (4.1) and (4.2).

	R_s (Ω)	R_p ($\times 10^4$ Ω)	Y_0 ($\times 10^{-5}$ S · s^n)	n	C_{CPE} ($\times 10^{-5}$ F)
$Al_{52}Mn_{18}Mo_{30}$	56.15 ± 0.78	5.78 ± 0.42	1.88 ± 0.71	0.886 ± 0.028	1.93 ± 0.81
$Al_{58}Mn_{15}Mo_{27}$	56.11 ± 1.22	7.59 ± 0.59	1.87 ± 0.62	0.906 ± 0.034	1.99 ± 0.84
$Al_{65}Mn_{13}Mo_{22}$	17.25 ± 0.64	9.18 ± 0.46	1.93 ± 0.86	0.916 ± 0.020	2.12 ± 0.72
$Al_{80}Mn_8Mo_{12}$	15.44 ± 0.59	27.20 ± 6.80	3.29 ± 0.58	0.928 ± 0.011	4.52 ± 0.27
$Al_{80}Mn_{20}$	29.78 ± 0.43	12.10 ± 7.10	2.43 ± 0.64	0.925 ± 0.032	2.58 ± 0.69

4.4.3 XPS analysis of the passive layer

For a better understanding of the passive film, the surface chemistry and structure of selected samples: $Al_{80}Mn_{20}$, $Al_{80}Mn_8Mo_{12}$, and $Al_{52}Mn_{18}Mo_{30}$, were characterized in detail hereafter in section 4.4.3 and 4.4.4. The XPS elemental depth profiles are shown in Fig. 4.8. The metal/oxide interface (dash lines marked in Fig. 4.8) was defined at 16 at.% O. It can be seen that the passive film was mainly composed of aluminum and oxygen for all samples, regardless of Mn and/or Mo compositions in the alloy. The thinnest passive film was observed in $Al_{52}Mn_{18}Mo_{30}$, which corresponds to a sputtering time of ~ 5.5 mins. According to TEM measurement of the same passive film (~ 11.9 nm in Fig. 4.6), a sputtering rate of ~ 2.16 nm/min can be estimated. Based on this calibration, the passive film thickness of both $Al_{80}Mn_{20}$ and $Al_{80}Mn_8Mo_{12}$ is estimated to be around 19.5 nm. It is interesting to note here that for these two samples, despite of different Mn and Mo concentrations, their identical Al% led to the same passive film thickness. In addition, the passive element Mo was largely absent (less than 1 at.%) in the passive film of $Al_{80}Mn_8Mo_{12}$, despite it being a passive-element, similar to the behavior of the non-passive element Mn [30]. Nonetheless, with higher Mn and Mo concentration in the alloy, a slightly higher concentration of Mn (3.5 at.%) and Mo (2.5 at.%) was measured in the passive film of $Al_{52}Mn_{18}Mo_{30}$.

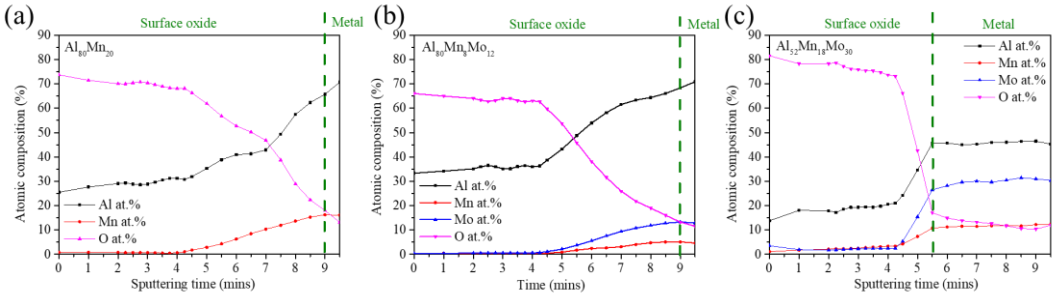

Figure 4.8 XPS depth profile of selected samples after PD test.

Fig. 4.9 shows XPS spectra of Al 2p, O 1s, Mo 3d and Mn 2p as a function of sputtering cycles (where cycle 1 is for the outmost surface) for all three samples. For all these samples, the outer surface contained mainly aluminum oxide (peak around 75.5-76 eV) and a small amount of Al-Al bond (peak around 72.5 eV), while the

intensities of the aluminum oxide and O 1s peaks decreased dramatically (~ 15-18 cycles for $Al_{80}Mn_8Mo_{12}$ and $Al_{80}Mn_{20}$, ~ 13 cycles for $Al_{52}Mn_{18}Mo_{30}$) with increasing sputtering depth. Mn was largely absent in $Al_{80}Mn_8Mo_{12}$ due to its low concentration, while a very small amount was detected in the passive film of $Al_{80}Mn_{20}$ and $Al_{52}Mn_{18}Mo_{30}$, Mn in its metallic state (0 charge), in agreement with our previous work [30]. Similar to Mn, the concentration of Mo was very low in the passive film and showed no enrichment at the metal/oxide interface, despite it being a passive element and high concentration in the alloy, consistent with prior reports from Al-Mo corrosion in Cl-containing neutral solutions [41]. Nonetheless, in $Al_{80}Mn_8Mo_{12}$ and $Al_{52}Mn_{18}Mo_{30}$, the very small amount of Mo oxide was found to be of +4 and +6 oxide state. The deconvoluted Mo 3d spectra (Fig. 10) can confirm that the topmost passive film included MoO_3 (~ 233.1 eV), while MoO_2 (~ 229.5 eV) remained in the inner passive layer. The absence of higher amounts of Mo oxide formation is likely due to a higher affinity of Al to O than that of Mo as a result of their respective oxidation energy per Ellingham diagram [45]. It is also noted that according to the Al-Mo-O phase diagram predictions [46], in addition to the alumina (Al_2O_3) and Mn phases, additional solid phases of $Al_{22}Mo_5$, Al_8Mo_3, and $AlMo_3$ phases could also form with increasing Mo/Al ratio, whose presence cannot be completely ruled out, but is estimated to be negligible given the lack of Al 2p peaks below 74 eV in the first ten cycles or so.

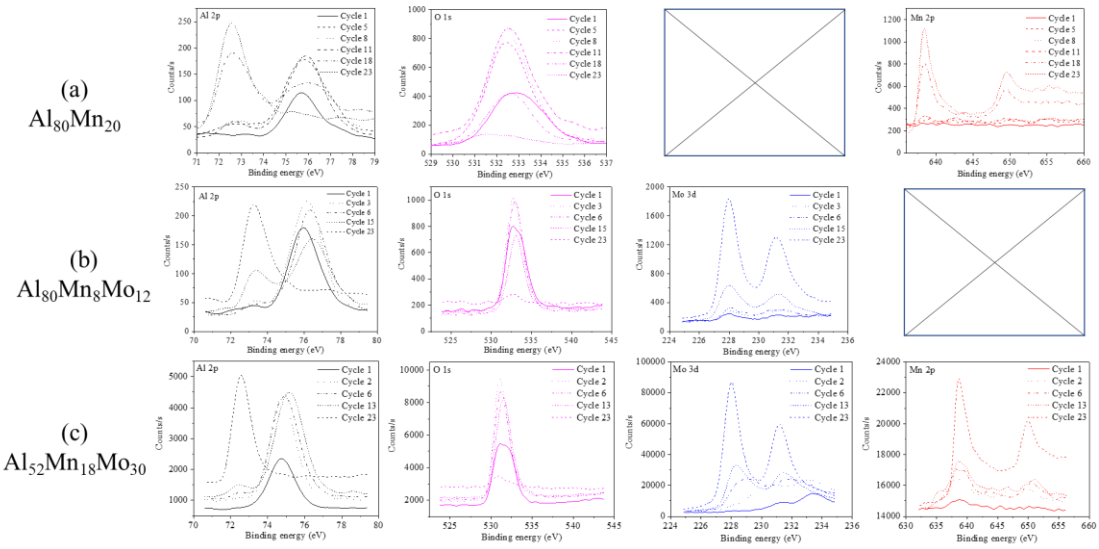

Figure 4.9 XPS depth profile of Al 2p, O 1s, Mo 3d and Mn 2p spectra for $Al_{80}Mn_{20}$,

$Al_{80}Mn_8Mo_{12}$, and $Al_{52}Mn_{18}Mo_{30}$ samples.

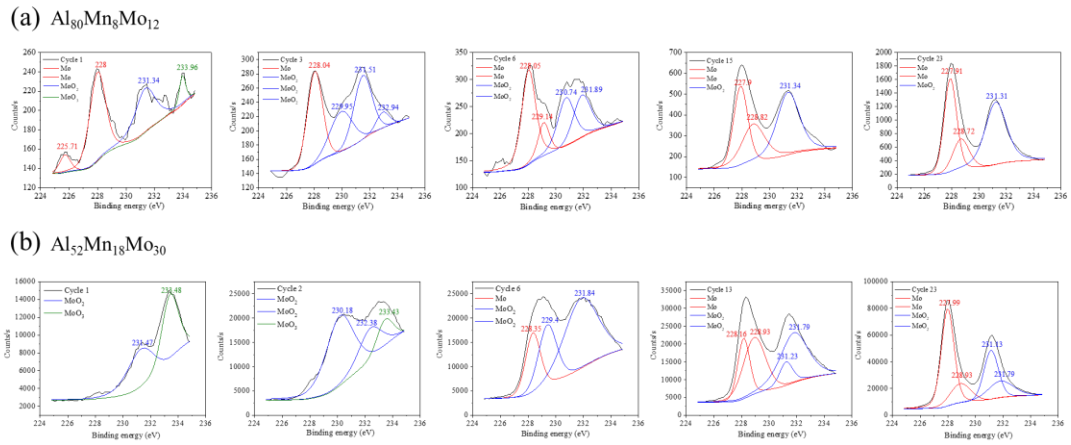

Figure 4.10 The spectral deconvolution of Mo 3d in the passive film of $Al_{80}Mn_8Mo_{12}$ and $Al_{52}Mn_{18}Mo_{30}$.

4.4.4 M-S analysis of the passive layer

Passive films on metal surface are usually semiconducting with some defects. The defect characteristics (e.g. type and density) governs the barrier characteristics and the breakdown of the passive films, which were measured by M-S analysis as summarized in Fig. 4.11. The defect densities (N) of the passive film were calculated by [47-51]:

$$\frac{1}{C^2} = \frac{\pm 2}{\varepsilon \varepsilon_0 e N}\left(E - E_{fb} - \frac{kT}{e}\right), \tag{4.3}$$

where C is the capacitance measured, ε is the passive film dielectric constant (assumed to be 10 for Al_2O_3 [52]), ε_0 is the permittivity of vacuum (ε_0= 8.85×10^{-14} F/cm), E is the applied potential, E_{fb} is the flat band potential, k is the Boltzmann constant (1.38×10^{-23} J/K), T is the absolute temperature, and e is the elementary charge (1.602×10^{-19} C). It was found that in all three cases, p-type defects appeared at lower potentials while n-type defects at higher potentials, similar to that of Al-Mn [30]. Usually, n-type defects include oxygen vacancies and/or cation interstitials (e.g. Al^{3+}), while p-type defects include cation vacancies. It thus indicates that metal-deficit (p-type) oxide forms at lower potentials, likely due to the selective dissolution of Mn and Mo, which changes to a metal-excess (n-type) oxide at higher potentials with increasing amounts of Al^{3+} generated. Fig. 4.11(b) shows that both n- and p-type defect density is lower in Al-Mn-Mo than Al-Mn alloys, with the smallest p-type defect density in

$Al_{80}Mn_8Mo_{12}$ and smallest n-type defect density in $Al_{52}Mn_{18}Mo_{30}$ alloys.

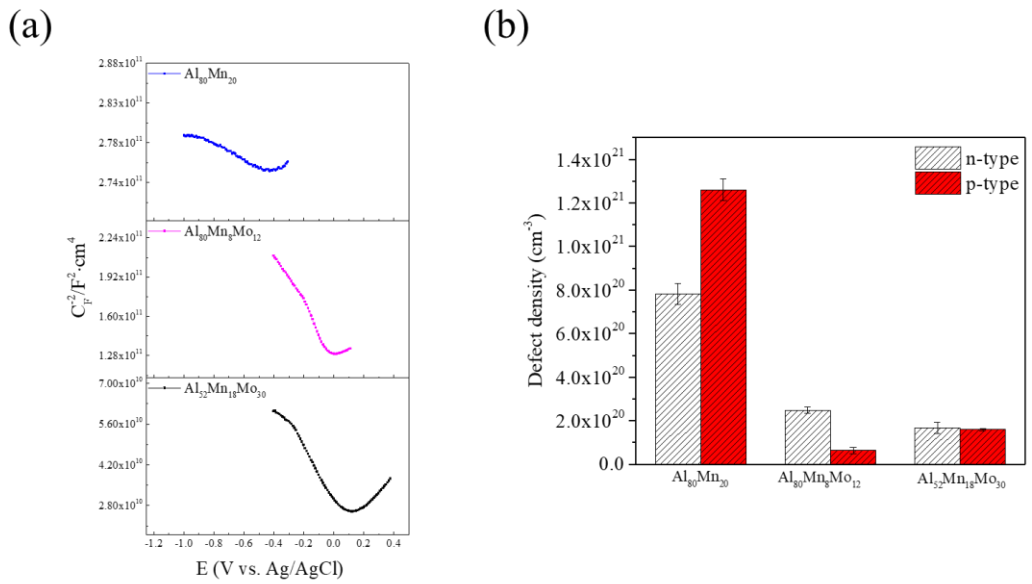

Figure 4.11 (a) M-S analysis of passive films (b) average of n-type and p-type defect on Al-Mn and Al-Mn-Mo concentrated alloys.

4.4.5 Alloying effects on the tribocorrosion behavior of Al-Mn-Mo alloys

Fig. 4.12 shows the current and current density evolution over time on the tribocorroded surface of all samples. Both current and current density evolution over time were plotted for 1,000 s for easy visualization. It can be seen that both current and current density increased with increasing Mn plus Mo content during tribocorrosion test. The current of the whole exposed area in $Al_{52}Mn_{18}Mo_{30}$ is 5 times higher than that in $Al_{80}Mn_{20}$, while the current density of the worn area in $Al_{52}Mn_{18}Mo_{30}$ is 3 times higher than that in $Al_{80}Mn_{20}$. This is due to the larger worn area of $Al_{52}Mn_{18}Mo_{30}$, which is shown in Fig. 4.13. The width of the worn area increased from 145.16 μm to 290.32 μm with increasing Mo content from 0 at.% to 18 at.%. The same trend of the worn area width was observed in dry wear (not shown here). This suggested that the mechanical properties, rather than corrosion properties, dominated the tribocorrosion behavior of Al-Mn-Mo alloys.

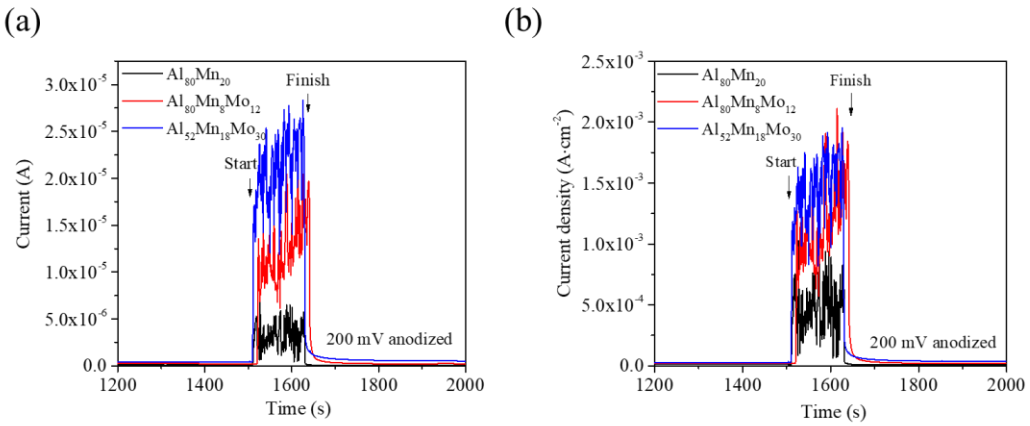

Figure 4.12 (a) Current and (b) current density evolution over time on the worn area of $Al_{80}Mn_{20}$, $Al_{80}Mn_8Mo_{12}$, and $Al_{52}Mn_{18}Mo_{30}$ samples during tribocorrosion test under 0.5 N and 1 Hz conditions.

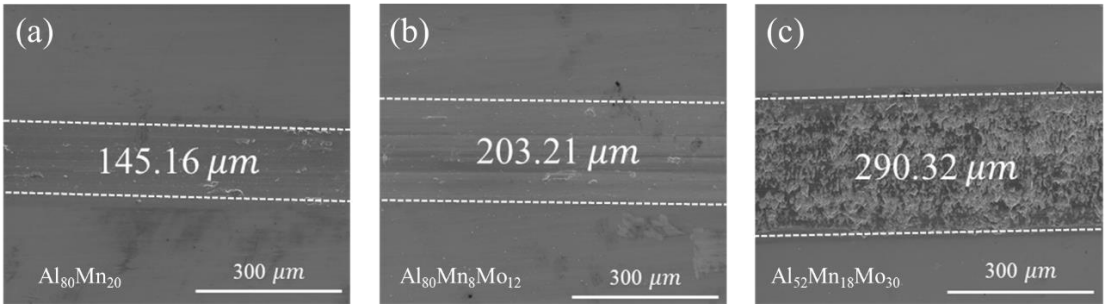

Figure 4.13 Surface SEM of (a) $Al_{80}Mn_{20}$, (b) $Al_{80}Mn_8Mo_{12}$, and (c) $Al_{52}Mn_{18}Mo_{30}$ after 120 s tribocorrosion test in 0.6 M NaCl solution at room temperature.

4.4.6 Discussion of corrosion mechanisms in Al-Mn vs. Al-Mn-Mo

Results in Sections 4.4.1-4.4.4 indicate that alloy compositions play a significant role in affecting the passive film characteristics and the corrosion behavior. The main conclusions include: (1) increasing Mo concentrations in the alloy increased the pitting potential and lowered the defect density in the passive film, (2) passive film thickness increases with Al% in the alloy and is insensitive to the Mn and Mo concentrations, and most interestingly, (3) a better corrosion resistance was observed in $Al_{80}Mn_8Mo_{12}$ than $Al_{80}Mn_{20}$, where the only difference was 12% Mo in the former vs. 12% Mn in the latter.

Here, we discuss the specifically corrosion mechanisms of $Al_{80}Mn_8Mo_{12}$ vs. $Al_{80}Mn_{20}$. The calculated potential/pH (Pourbaix) diagrams of Al_xMn_y and $Al_xMn_yMo_z$

with 1<x, y, z<99 at.% following algorithms reported in [53, 54] are shown in Fig. 4.14. With the addition of Mo, the passive region of Al-Mn expanded to a wider pH range. Unlike Mn that is selectively dissolved in water, Mo can form insoluble MoO_2 below 0 V. Such Mo oxide could also be dissolved at higher potentials and from MoO_4^{2-} per the following reactions [45]:

$$MoO_2 + 2H_2O \rightarrow HMoO_4^- + 3H^+ + 2e^-, \quad (4.4)$$

$$MoO_3 + H_2O \rightarrow HMoO_4^- + H^+. \quad (4.5)$$

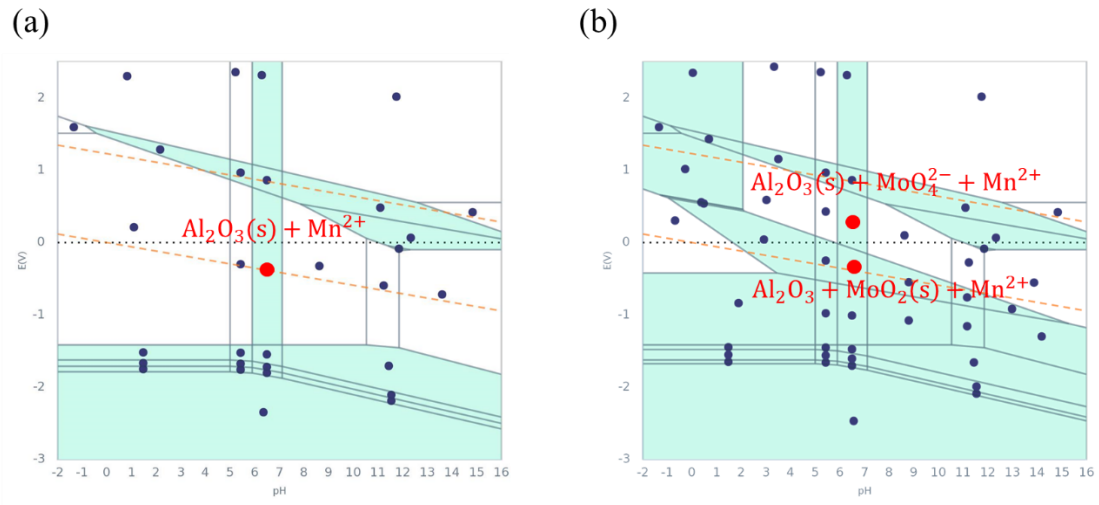

Figure 4.14 The calculated potential/pH (Pourbaix) diagram of Al_xMn_y and $Al_xMn_yMo_z$ with concertation of Al, Mn, and Mo ranging from 1 to 99 at.%.

As shown in Figs. 4.8 and 4.9, such thermodynamically predicted Mo oxide phases were indeed detected via XPS analysis, however, with concentrations less than 1 at.%, well below the alloy concentrations. It is thus argued that in both alloys, the aluminum oxide (alumina) phase, rather than Mo oxides, dominate the passive film growth, whose compactness and defect characteristics controls the corrosion kinetics.

Next, we discuss that the difference of 12% Mo vs. 12% Mn in affecting the passive film defect density. A schematic of the proposed defect structure of the two alloys are shown in Fig. 4.15. For both alloys, the passive film is p-type at lower potentials and n-type at higher potentials. For $Al_{80}Mn_{20}$, cation vacancies were created on the metal/passive film interface due to the selective dissolution of Mn at lower potentials. With increasing potential and more generation of Al^{3+}, the dominating defect

type changes to anion (oxygen) vacancy, hence a change to n-type defect. For $Al_{80}Mn_8Mo_{12}$, at lower potentials, less Mn was dissolved at the metal/passive film interface due to its lower alloy concentration (8%), hence lower p-type defect density. At higher potentials, the doping of Mo ions with higher oxidation state (+4 and +6) in alumina with Al (+3) leads to the generation of more free electrons. As a result, the oxygen vacancies can be reduced by combining with these free electrons, ultimately decreasing the n-type defect density. According to the point defect theory [55-57], the pitting corrosion is assumed to occur on the oxide/solution interface involving the adsorption of chloride ions into oxygen vacancies [58]. The chloride ions transported through the oxide film by means of oxygen vacancies. Therefore, reducing n-type defect density is expected to reduce chloride adsorption and improve pitting resistance. This is in good agreement with PD results shown in Fig. 4.4(b).

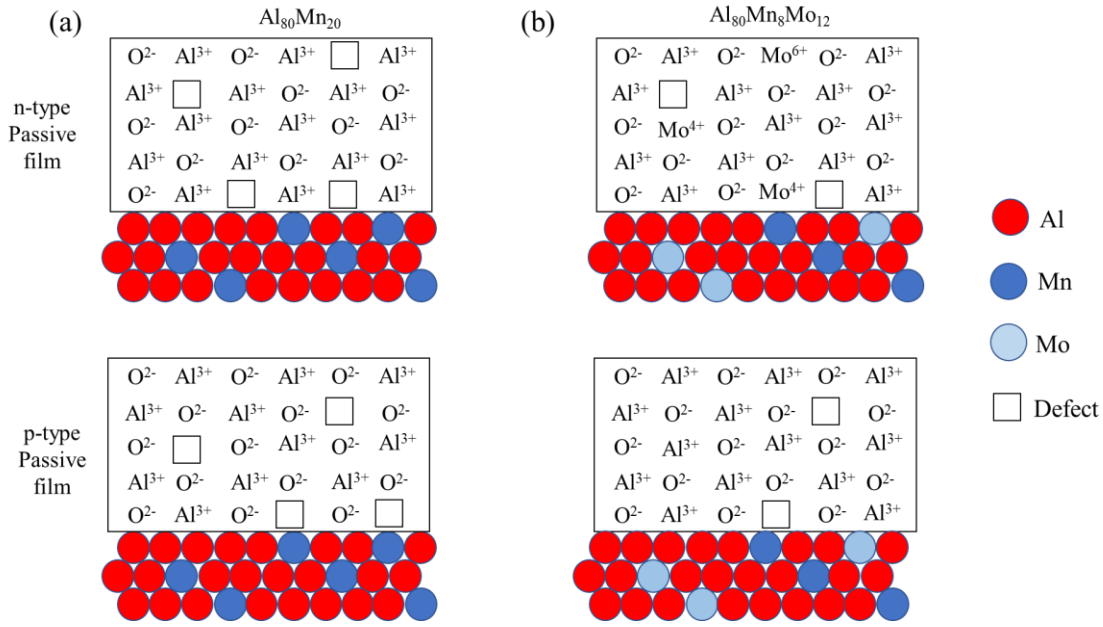

Figure 4.15 The schematic intrinsic defects in the passive film between $Al_{80}Mn_{20}$ and $Al_{80}Mn_8Mo_{12}$ formed at low and high corrosion potentials.

Finally, molecular dynamic simulations were performed by Jianwei Xiao and Chuang Deng to show that the compactness of the passive film was also affected by the Mn/Mo ratio in the alloy, mainly due to their different atomic radius. It was confirmed that the larger interatomic distance in Al-Mn-Mo than that of Al-Mn, leads to more Al-

O bonds formation. Since the interactions between O and Mn (or Pd) were muted in the simulations and the only difference between the two alloy systems was their atomic packing, it suggests that the more compact passive layer in Al-Mn-Mo than Al-Mn could be, at least partially, contributing to the higher corrosion resistance of the former as seen in the experiments. In summary, unlike some previous research that attributes the enhancement of corrosion resistance of Al-transition metal due to the enrichment of the transition metal in the passive film, our work clarifies the roles of transition metals Mn and Mo. Specifically for Mo, their selective dissolution, rather than oxidation, at the metal/oxide interface facilitate the formation of a more compact passive film with lower defect density.

4.5 Conclusions

This work systematically investigated the effects of Mo and Mn on the corrosion resistance of Al-Mn-Mo concentrated alloys via experiments and simulations. The main results and understandings are concluded as follows:

(1) The open circuit potential of all Al-Mn-Mo alloys was higher than that of $Al_{80}Mn_{20}$.
(2) Mo addition significantly improved the pitting resistance of Al-Mn-Mo.
(3) An optimum alloy concentration of $Al_{80}Mn_8Mo_{12}$ was identified that showed the highest corrosion resistance among all binary and ternary alloys studied.
(4) XPS revealed that the passive film is mainly composed of alumina in the ternary alloys, with trace amount of Mn (0) and Mo ions (+4 and +6).
(5) M-S analysis shows that Mo addition to the alloy reduced both the p-type and n-type defect density of the passive film. The doping of Mo ions with a higher oxidation state than Al ions decreased the n-type defect density in the passive film by creating more free electrons to combine with oxygen vacancies.
(6) The width of the worn area increased with increasing Mo content in tribocorrosion test.

In summary, these findings indicate the necessity to carefully tune the global as well as individual alloy concentrations of Al-based LCAs when designing future

corrosion-resistant concentrated alloys.

References

1. Li, L., M. Chakik, and R. Prakash, *A Review of Corrosion in Aircraft Structures and Graphene-Based Sensors for Advanced Corrosion Monitoring.* Sensors, 2021. **21**(9).
2. Chu, J.H., et al., *Bio-inspired graphene-based coatings on Mg alloy surfaces and their integrations of anti-corrosive/wearable performances.* Carbon, 2019. **141**: p. 154-168.
3. Heakal, F.E.-T. and A.E. Elkholy, *Smart coatings on magnesium alloys in transportation industries*, in *Advances in Smart Coatings and Thin Films for Future Industrial and Biomedical Engineering Applications*. 2020. p. 263-287.
4. Lekatou, A., et al., *Microstructure and corrosion performance of Al-32%Co alloys.* Corrosion Science, 2012. **63**: p. 193-209.
5. Zhang, S.D., et al., *Identifying the role of nanoscale heterogeneities in pitting behaviour of Al-based metallic glass.* Corrosion Science, 2011. **53**(9): p. 3007-3015.
6. Presuel-Moreno, F., et al., *Corrosion-resistant metallic coatings.* Materials Today, 2008. **11**(10): p. 14-23.
7. Ahmad, Z., *Aluminium Alloys - New Trends in Fabrication and Applications*. 2012.
8. Sahu, K.K., et al., *Phase separation mediated devitrification of Al88Y7Fe5 glasses.* Acta Materialia, 2010. **58**(12): p. 4199-4206.
9. Kim, Y. and R.G. Buchheit, *A characterization of the inhibiting effect of Cu on metastable pitting in dilute Al-Cu solid solution alloys.* Electrochimica Acta, 2007. **52**(7): p. 2437-2446.
10. Kim, Y., R.G. Buchheit, and P.G. Kotula, *Effect of alloyed Cu on localized corrosion susceptibility of Al-Cu solid solution alloys-Surface characterization by XPS and STEM.* Electrochimica Acta, 2010. **55**(24): p. 7367-7375.
11. Zhang, L.M., et al., *Thermally induced structure evolution on the corrosion*

behavior of Al-Ni-Y amorphous alloys. Corrosion Science, 2018. **144**: p. 172-183.

12. Babilas, R., et al., *Electrochemical characterization of Al84Ni9Y7 metallic glass after annealing process.* Journal of Non-Crystalline Solids, 2019. **518**: p. 24-35.
13. Gao, M., et al., *High corrosion and wear resistance of Al-based amorphous metallic coating synthesized by HVAF spraying.* Journal of Alloys and Compounds, 2018. **735**: p. 1363-1373.
14. Lucente, A.M. and J.R. Scully, *Localized Corrosion of Al-Based Amorphous-Nanocrystalline Alloys with Solute-Lean Nanocrystals: Pit Stabilization.* Journal of The Electrochemical Society, 2008. **155**(5).
15. Esquivel, J., et al., *Excellent corrosion resistance and hardness in Al alloys by extended solid solubility and nanocrystalline structure.* Materials Research Letters, 2017. **6**(1): p. 79-83.
16. Henao, J., et al., *Novel Al-based metallic glass coatings by Cold Gas Spray.* Materials & Design, 2016. **94**: p. 253-261.
17. Zhang, S.D., et al., *In situ EC-AFM study of the effect of nanocrystals on the passivation and pit initiation in an Al-based metallic glass.* Corrosion Science, 2014. **83**: p. 111-123.
18. Cheng, J., et al., *In-situ synthesis of novel Al-Fe-Si metallic glass coating by arc spraying.* Journal of Alloys and Compounds, 2017. **716**: p. 88-95.
19. Aburada, T., et al., *Effect of Ni as a minority alloying element on the corrosion behavior in Al–Cu–Mg–(Ni) metallic glasses.* Scripta Materialia, 2008. **58**(8): p. 623-626.
20. Tseng, K., et al., *A light-weight high-entropy alloy Al20Be20Fe10Si15Ti35.* Science China Technological Sciences, 2017. **61**(2): p. 184-188.
21. Qiu, Y., et al., *Microstructure and corrosion properties of the low-density single-phase compositionally complex alloy AlTiVCr.* Corrosion Science, 2018. **133**: p. 386-396.
22. Qiu, Y., et al., *A lightweight single-phase AlTiVCr compositionally complex*

alloy. Acta Materialia, 2017. **123**: p. 115-124.

23. Stepanov, N.D., et al., *Structure and mechanical properties of a light-weight AlNbTiV high entropy alloy.* Materials Letters, 2015. **142**: p. 153-155.
24. Stepanov, N.D., et al., *Structure and mechanical properties of the AlCrxNbTiV (x = 0, 0.5, 1, 1.5) high entropy alloys.* Journal of Alloys and Compounds, 2015. **652**: p. 266-280.
25. Gao, M., et al., *Influence of yttrium on surface chemistry and stability of passive film in Al-based binary metallic glasses.* Applied Surface Science, 2018. **457**: p. 536-547.
26. Yu, L., et al., *Corrosion behavior of bulk (Zr58Nb3Cu16Ni13Al10)100-xYx (x = 0, 0.5, 2.5 at.%) metallic glasses in sulfuric acid.* Corrosion Science, 2019. **150**: p. 42-53.
27. Raza, A., et al., *Corrosion resistance of weight reduced AlxCrFeMoV high entropy alloys.* Applied Surface Science, 2019. **485**: p. 368-374.
28. Lee, C.P., et al., *Enhancing pitting corrosion resistance of AlxCrFe1.5MnNi0.5 high-entropy alloys by anodic treatment in sulfuric acid.* Thin Solid Films, 2008. **517**(3): p. 1301-1305.
29. Zhang, L.M., et al., *Influence of cerium content on the corrosion behavior of Al-Co-Ce amorphous alloys in 0.6 M NaCl solution.* Journal of Materials Science & Technology, 2019. **35**(7): p. 1378-1387.
30. Chen, J., et al., *The origin of passivity in aluminum-manganese solid solutions.* Corrosion Science, 2020. **173**.
31. Ruan, S. and C.A. Schuh, *Electrodeposited Al–Mn alloys with microcrystalline, nanocrystalline, amorphous and nano-quasicrystalline structures.* Acta Materialia, 2009. **57**(13): p. 3810-3822.
32. Reffass, M., et al., *Corrosion behaviour of magnetron-sputtered Al1-x-Mn-x coatings in neutral saline solution.* Corrosion Science, 2010. **52**(11): p. 3615-3623.
33. Moshier, W.C., et al., *Corrosion Behavior of Aluminum-Molybdenum Alloys in*

Chloride Solutions. Journal of the Electrochemical Society, 1987. **134**(11): p. 2677-2684.

34. JanikCzachor, M., A. Wolowik, and Z. Werner, *Breakdown of passivity of Al-Mo glassy metals.* Passivation of Metals and Semiconductors, 1995. **185-**: p. 1049-1055.
35. Wolowik, A., et al., *Inter-relationships between alloy composition, passive film composition and pitting behaviour of Al-Mo and Al-Mo-Si metastable alloys.* Corrosion Science, 1998. **40**(4-5): p. 731-740.
36. Janik-Czachor, M., et al., *The stability of the passive state on Al-Mo sputter-deposited glassy metals.* Corrosion Science, 1994. **36**(11): p. 1921-1923.
37. Tsuda, T., C.L. Hussey, and G.R. Stafford, *Electrodeposition of Al-Mo-Mn ternary alloys from the Lewis acidic AlCl3-EtMeImCl molten salt.* Journal of the Electrochemical Society, 2005. **152**(9): p. C620-C625.
38. Wolowik, A. and M. Janik-Czachor, *Anodic behaviour of Al-refractory metal amorphous alloys.* Materials Science and Engineering a-Structural Materials Properties Microstructure and Processing, 1999. **267**(2): p. 301-306.
39. Janik-Czachor, M., et al., *Passivity and its breakdown in Al-based amorphous alloys.* Materials Chemistry and Physics, 2005. **92**(2-3): p. 348-353.
40. Al-Saffar, A.H., et al., *The effect of molybdenum ion implantation on the general and pitting corrosion behaviour of pure aluminium and a high strength aluminium alloy.* Corrosion Science, 1980. **20**(1): p. 127-144.
41. Principe, E.L., B.A. Shaw, and G.D. Davis, *Role of oxide/metal interface in corrosion resistance: Al-W and Al-Mo systems.* Corrosion, 2003. **59**(4): p. 295-313.
42. Jeurgens, L., et al., *Thermodynamic stability of amorphous oxide films on metals: Application to aluminum oxide films on aluminum substrates.* Physical Review B, 2000. **62**(7): p. 4707-4719.
43. Salih, S.M., I.K. Shakir, and A.M.A. Al-Sammarraie, *Comparison of Aggressiveness Behavior of Chloride and Iodide Solutions on 304 and 304L*

Stainless Steel Alloys. Materials Sciences and Applications, 2017. **08**(12): p. 889-898.

44. Chang, B.-Y., *Conversion of a Constant Phase Element to an Equivalent Capacitor.* Journal of Electrochemical Science and Technology, 2020. **11**(3): p. 318-321.
45. Wang, C.X., et al., *The effect of phase structure on the corrosion behavior of Al100-xMox alloy thin films.* Journal of Alloys and Compounds, 2019. **790**: p. 563-571.
46. Gubbels, G.H.M., *Interfaces in composites of alumina in a molybdenum matrix.* Materials Science and Engineering: A, 1991. **135**: p. 135-139.
47. Zhang, B., Y. Li, and F.H. Wang, *Electrochemical corrosion behaviour of microcrystalline aluminium in acidic solutions.* Corrosion Science, 2007. **49**(5): p. 2071-2082.
48. Zhang, J.F., et al., *Corrosion behaviors of Zn/Al-Mn alloy composite coatings deposited on magnesium alloy AZ31B (Mg-Al-Zn).* Electrochimica Acta, 2009. **55**(2): p. 560-571.
49. Martin, F.J., et al., *Impedance studies of the passive film on aluminium.* Corrosion Science, 2005. **47**(12): p. 3187-3201.
50. de Oliveira, M.C.L., et al., *Correlation between the corrosion resistance and the semiconducting properties of the oxide film formed on AZ91D alloy after solution treatment.* Corrosion Science, 2013. **69**: p. 311-321.
51. Lv, J.L. and H.Y. Luo, *Comparison of corrosion properties of passive films formed on phase reversion induced nano/ultrafine-grained 321 stainless steel.* Applied Surface Science, 2013. **280**: p. 124-131.
52. Gonzalez, J.A., et al., *Characterization of porous aluminium oxide films from ac impedance measurements.* Journal of Applied Electrochemistry, 1999. **29**(2): p. 229-238.
53. Persson, K.A., et al., *Prediction of solid-aqueous equilibria: Scheme to combine first-principles calculations of solids with experimental aqueous states.*

Physical Review B, 2012. **85**(23).

54. Singh, A.K., et al., *Electrochemical Stability of Metastable Materials.* Chemistry of Materials, 2017. **29**(23): p. 10159-10167.

55. Chao, C.Y., L.F. Lin, and D.D. Macdonald, *A Point Defect Model for Anodic Passive Films: I . Film Growth Kinetics.* Journal of The Electrochemical Society, 1981. **128**(6): p. 1187-1194.

56. Lin, L.F., C.Y. Chao, and D.D. Macdonald, *A Point Defect Model for Anodic Passive Films: II . Chemical Breakdown and Pit Initiation.* Journal of The Electrochemical Society, 1981. **128**(6): p. 1194-1198.

57. Chao, C.Y., L.F. Lin, and D.D. Macdonald, *A Point Defect Model for Anodic Passive Films: III . Impedance Response.* Journal of The Electrochemical Society, 1982. **129**(9): p. 1874-1879.

58. Macdonald, D.D., *Passivity - the key to our metals-based civilization.* Pure and Applied Chemistry, 1999. **71**(6): p. 951-978.

Chapter 5: Summary and Future Work

5.1 Summary of present work

In this thesis, Al-Mn and Al-Mn-Mo solid solution alloys were fabricated under vacuum by magnetron sputtering, which were found to exhibit both high corrosion and tribocorrosion resistance, outperforming most of commercial Al alloys.

In study 1, the depassivation-repassivation kinetics of Al-20 at.%Mn alloys were studied as a function of scratching frequency. It is discovered that both chemical and mechanical wear rate increased with increasing frequency. The mechanical wear increased with frequency due to faster depassivation rate and increased real contact area, while chemical wear increased with frequency due to higher repassivation kinetics. Specifically, the repassivation kinetics were found to strongly depend on the scratching frequency, which controlled the repassivation time between consecutive passes of the counter body on the depassivated wear track. At higher scratching frequency, the fast scratching rate left little time for repassivation. At lower frequency, the depassivated area had enough time to repassivate, thus a much lower repassivation current was required.

In study 2, the corrosion and passivation mechanism of Al-20 at.%Mn alloys were studied by electrochemical measurements and advanced surface characterization. It was discovered that Mn addition enhanced corrosion resistance of Al without participating in the surface oxidation process. A denser and thinner oxide layer was formed on the surface of Al-Mn as compared to pure Al, due to the selective dissolution of Mn in water, resulting in a higher free volume of Al at the surface. The observed alloying effect can be explained by a proposed lattice mismatch model considering the effective Pilling-Bedworth (PB) ratio between the metal substrate and its oxide. Alloys with effective PB ratio close to 1 favors the formation of an oxide layer with high density and low porosity due to excellent structural compatibility between the oxide and the metal lattices. In this study, the PB ratio was found to be ~ 1.06 for Al-20 at.%Mn, as

compared to ~ 1.33 in pure Al, in agreement with the higher barrier characteristics of the passive film in the former.

In the last study, the effects of Mo on the pitting corrosion and tribocorrosion of Al-Mn-Mo alloys with 8-20 at.% Mn and 0-30 at.% Mo were studied. The doping of Mo ions with higher oxidation state (+4 and +6) than Al (+3) led to the generation of more free electrons in the passive film. As a result, the oxygen vacancies (n-type defect) can be reduced by combining with these free electrons. Since pitting corrosion is assumed to occur on the oxide/solution interface involving the adsorption of chloride ions into oxygen vacancies, thus reducing n-type defect density is expected to reduce chloride adsorption and improve pitting resistance. The tribocorrosion resistance of Al-Mn-Mo alloys was lower than that of Al-Mn alloys, which was mainly controlled by mechanical mechanism. The worn area increased with increasing Mo content.

5.2 Future work

Several future research directions are proposed next based on results from this thesis, with a goal of developing mechanistic understanding of the alloying effects on the mechanical and corrosion properties of Al alloys, with an ultimate goal of developing high performance, lightweight, strong, and corrosion resistant metals.

A. For the future design of Al-based concentrated alloys and high entropy alloys, it would be of great interest to design compositions based on the effective PB ratio to optimize the barrier characteristic of the passive film, based on the models developed in chapters 3 and 4. Specifically, it would be interesting to study the effect of passivating element such as Cr and Co on the passivation of corrosion resistance of Al-based concentrated alloys, where all elements could participate in the surface oxidation. A detailed characterization of the corroded and tribocorroded surfaces of these alloys could further modify the PB ratio model developed in this thesis, to become a more universal model for complex alloy systems.
B. In terms of tribocorrosion, it is unclear how the microstructure at and below the

surface of Al alloys evolve as a function of testing parameters such as normal load, sliding frequency, solution temperature, and chemistry. Some researchers have used TEM analysis to reveal the plastic deformation of the steel on the wear track from the first sliding cycle. It would be of great interest to see whether the deformation could be changed by cyclic loading in Al alloys. Since the thickness of passive film is nano scale, it really needs a higher resolution TEM equipment to analyze the microstructure of the passive film, e.g., Grand ARM and FEI Tecnai. The microstructure information can be obtained from TEM images and SAD patterns. To improve the image signal from the passive film, the field emission gun should be chosen. The EDS signal can be enhanced by using smaller spot size and higher electron current.

C. Lastly, future research in this area could benefit greatly by combining atomistic surface characterization and computer simulations. MD simulation can be used to calculate activation energy and identify oxygen transport pathways, then to understand the free volume or Al-Al bond distance via alloying with other elements. Density functional theory (DFT) can be used to calculate the chloride and oxygen adsorption energy, then to understand the passivation of Al-based high entropy alloys in corrosive environment (note: Al-based high entropy alloys should be a crystalline structure when using DFT).

Appendix A:

Determining Tribocorrosion Rate and Wear-Corrosion Synergy of Bulk and Thin Film Aluminum Alloys

Jia Chen[1,2], Hesham Mraied[3], and Wenjun Cai[1,2]

1 Department of Mechanical Engineering, University of South Florida
2 Department of Materials Science and Engineering, Virginia Polytechnic Institute and State University
3 Department of Civil and Environmental Engineering, University of South Florida
*Corresponding author E-mail address: caiw@vt.edu.
Declarations of interest: none

*This appendix has been adapted from a **published** manuscript by Jia Chen, Hesham Mraied and Wenjun Cai from the following reference:*

Jia Chen, et al. "Determining Tribocorrosion Rate and Wear-Corrosion Synergy of Bulk and Thin Film Aluminum Alloys." Journal of Visualized Experiments, vol. 139, no. 139, 2018.

Reprinted with permission from JoVE.

A.1 Abstract

The increasing complexity and severity of service conditions in areas, such as aerospace and marine industries, nuclear systems, microelectronics, batteries, and biomedical devices, etc., impose great challenges on the reliable performance of alloys exposed to extreme conditions where mechanical and electrochemical attack co-exist. Finding ways for alloys to mitigate the combined attack of wear and corrosion (i.e., tribocorrosion) under such extreme conditions is thus highly critical for improving their reliability and service lifetime when used in such conditions. The challenge lies in the fact that wear and corrosion are not independent of each other, but rather work synergistically to accelerate the total material loss. Thus, a reliable method to evaluate the tribocorrosion resistance of metals and alloys is needed. Here, a protocol for measuring the tribocorrosion rate and wear-corrosion synergy of Al-based bulk and thin film samples in a corrosive environment under room temperature is presented.

A.2 Introduction

Tribocorrosion is a material degradation process caused by the combined effect of wear and corrosion[1, 2]. Tribocorrosion takes place both in nature and in industrial applications where mechanical contact and a corrosive environment are simultaneously present. The complexity of tribocorrosion lies in the fact that chemical and mechanical degradation mechanisms are not independent of each other. A combination of mechanical and chemical attack often leads to accelerated failure, due to synergetic effects. Thus, the total material loss can be calculated as

$$T = C_0 + W_0 + S, \tag{1}$$

where C_0 is the material loss resulted from corrosion in the absence of wear, W_0 is the material loss due to mechanical wear in the absence of corrosion, and S is the material loss due to wear-corrosion synergy [3, 4]. The synergetic effect is prominent for passive alloys such as aluminum, titanium, and stainless steels, which spontaneously form a protective thin (a few nanometers in thickness) oxide film (passive film) when in contact with oxygen or water [5, 6]. During corrosion, and if this passive film is locally disturbed by mechanical wear, depassivation could lead to localized corrosion and unexpected failures[1, 3, 7-9].

As an example of the economic impact of tribocorrosion in our society, wear and corrosion are estimated to cost nearly $300 billion per year in the United States [10]. In Florida, tribocorrosion phenomena of structural alloys in seawater is of interest given its ocean economy (fishing, marine transportation, and coastal construction), which contributes around 4% of Florida's total Gross Domestic Product [11]. Thus, a better understanding of tribocorrosion of metals and alloys will lead to better guidelines for application and usage of alloys in harsh environment service conditions. Such understanding will also serve to improve design principles for manufacturing new alloys and coatings against tribocorrosion and enhancing durability.

Tribocorrosion studies require integration of a tribometer and an electrochemical measurement system. The tribometer provides controlled mechanical loading and relative motion, and measures the friction force and sample surface height change. The electrochemical measurement system includes a potentiostat/galvanostat with a zero-resistance ammeter (optional) that determines open-circuit potential (OCP) and electrochemical polarization measurements. Such techniques provide a quick and inexpensive method to obtain the electrochemical properties of a material, where the corrosion rate of a metal can be measured by observing the response of the charge-transfer process to a controlled electrochemical disturbance. Here, we present a testing protocol for determining the tribocorrosion rate and wear-corrosion synergy of Al alloys, mostly following the ASTM standard G119 [2]. This protocol includes sample preparation, machine setup, tribocorrosion testing, and post-testing calculation procedures. We hope this effort will benefit those new to the field to perform reliable and repeatable tribocorrosion tests to evaluate the deformation and degradation behavior of bulk as well as thin film metallic samples.

CAUTION: Please consult all relevant materials safety data sheets (MSDS) before use. Some chemicals used in the protocol are toxic. Please use all appropriate safety practices when performing experiments, including the use of engineering controls (fume hood) and personal protective equipment (safety glasses, gloves, lab coat, full-length pants, and closed-toe shoes). The CNC (Computer Numerical Control) machine must be operated by trained personnel. Hydrofluoric acid must be handled inside a fume hood that is identified with a sign stating "Danger, Hydrofluoric Acid Used in this Area" or similar.

A.3 Sample preparation

NOTE: Proper surface preparation of samples prior to tribocorrosion tests is critical to ensure good reliability of the performed test and enhance test repeatability. In this protocol, a commercial Al 3003 alloy (Si: 0.1, Fe: 0.4, Cu: 0.08, Mn: 1.1 wt.%, balance Al) is used as an example.

3.1 Bulk metallic sample preparation

3.1.1 Cut as-received Al 3003 alloys (hereafter referred as Al) into several 1.5 × 2 cm^2 coupons using a CNC machine.

3.1.2 Mechanically grind one side of the sample surface using sandpaper with increasing grit numbers (#180, 240, 400, 600, and 1200).

3.1.2.1 Grind the sample using #180 sandpaper for 30 s along one arbitrary direction.

3.1.2.2 Rotate the sample 90˚ and grind it using #240 sandpaper until the scratch lines from the previous step are completely eliminated. Use an optical microscope to aid this inspection.

3.1.2.3 Repeat the sample rotation procedure and move to the next grinding paper. Use a soft brush between steps to clean the sample surface in running water to eliminate any contamination from the previous step.

3.1.3 After grinding, polish the sample surface using different sizes of high viscosity alumina polishing suspension (1 μm, 0.3 μm, and 0.05 μm) on microfiber cloth pads. Use a different cloth pad for each compound size.

3.1.3.1 Pour ~ 1 oz of 1 μm alumina suspension (10-30% alumina, 0.6-1% silica glass, 70-90% water) on a clean cloth pad. Polish the sample in one direction or draw a shape of '8' (avoid drawing a shape of '0') until removing the scratch lines from the previous step.

3.1.3.2 Repeat for 0.3 and 0.05 μm polishing suspension (10-30% alumina, 0.6-1% silica glass, 70-90% water) until reaching a mirror finish.

3.1.4 Place the polished specimen in a beaker with 40 mL of deionized (DI) water and place the beaker in an ultrasonic cleaner for 1-2 min to remove any surface particle. Use compressed gas to completely dry the surface. Fig. A.1(a) shows an example of an

unpolished vs. a polished Al sample.

3.1.5 Cut a 5 cm long, ~ 1-2 mm diameter electrical wire and strip away the protective plastic cover (~ 1 cm in length) on both ends to expose the interior Cu wire to air.

3.1.6 Electrically connect one end of the wire to the back (the unpolished side) of the sample using a conductive tape or conductive epoxy. If using conductive epoxy, follow the manufacturer's recommendation until complete cure.

3.1.7 Use electrochemical stop-off lacquer to paint a ~ 1×1 cm^2 window on the polished side and the complete back side of the sample. For the back side, paint over the exposed Cu wire.

3.1.8 Dry the painted sample completely in a well-ventilated fume hood for at least 24 h before the experiments. Fig. A.1(b) shows an example of the painted bulk sample, which is used as working electrode for the corrosion and tribocorrosion tests.

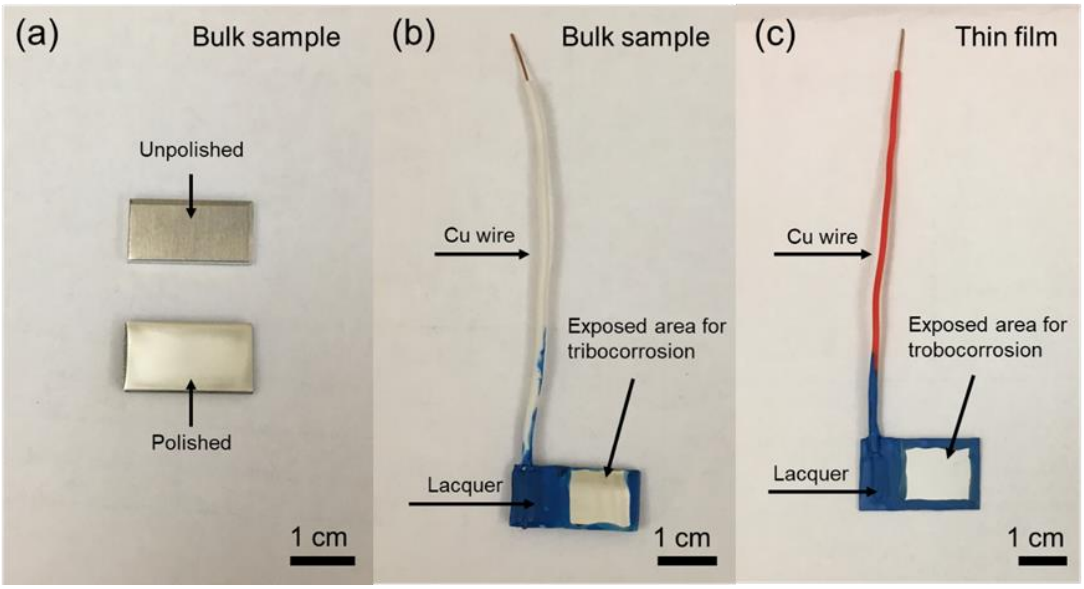

Figure A.1 Photo of (a) unpolished and polished Al bulk sample, (b) wired and painted bulk, and (c) thin film Al sample for tribocorrosion testing.

3.2 Thin film sample preparation

NOTE: Metallic thin films deposited on a flat substrate such as glass, Si wafer, and other metal plate using non-equilibrium processing techniques such as physical vapor deposition and electrodeposition can be used for tribocorrosion testing after proper preparation. Here a magnetron-sputtered Al-Mn thin film sample deposited on Si substrate is used as an example to explain the critical steps.

3.2.1 Polish a Si wafer (100 mm diameter) with 1:50 hydrofluoric acid water solution for 2 min to remove any surface oxidation layer.

3.2.2 Clean the Si wafer with 95% ethanol. Then dry it with compressed air and transfer it directly into a magnetron sputtering machine vacuum chamber.

3.2.3 Operate the sputtering machine at 80 W input power under a 5 mTorr argon atmosphere (99.99%) [1]. Grow a ~ 2-3 μm thickness Al-20at.%Mn film (hereafter referred as Al thin film) using an Al-Mn target in the sputtering machine.

3.2.4 Spin coat a thin protective layer of a positive photoresist (~ 10 mL for a 100 mL Si wafer) on the deposited side of Si wafer and dice it into several 1.5 × 2 cm^2 coupons.

3.2.5 Immerse the diced sample in acetone for 1 min to completely remove the protective layer. Rinse it by alcohol and finally dry it by compressed air.

3.2.6 Follow steps 3.1.5 and 3.1.8 to make an electrical connection and paint the sample surface for tribocorrosion test. Fig. A.1(c) shows an example of a painted thin film sample.

A.4 Tribocorrosion test

4.1 Tribocorrosion machine setup

4.1.1 Perform a tribocorrosion test using a custom-designed corrosion cell installed on a universal mechanical tester (UMT) as shown in Fig. A.2(a). Use the schematic of the tribocorrosion testing setup as shown in Fig. A.2(b). Fig. A.3 shows the custom-designed corrosion cell installed on the UMT rotary stage. The force sensing resolution is 50 μN and 50 mN for load ranges of 5-500 mN and 10-1000 N, respectively.

4.1.2 For the electrochemical measurement, use 2 x 10^{-17} Amp current resolution and 10^{14} Ω input impedance.

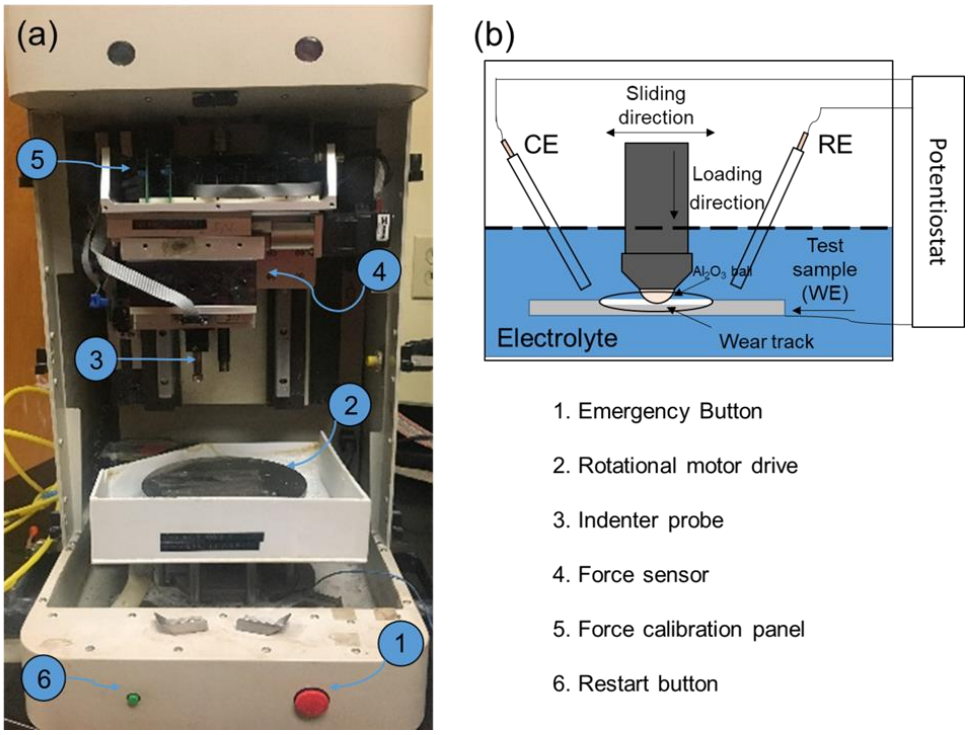

Figure A.2 (a) Photo of the front of the Bruker UMT machine without custom-made tribocorrosion cell. (b) schematic of tribocorrosion testing setup.

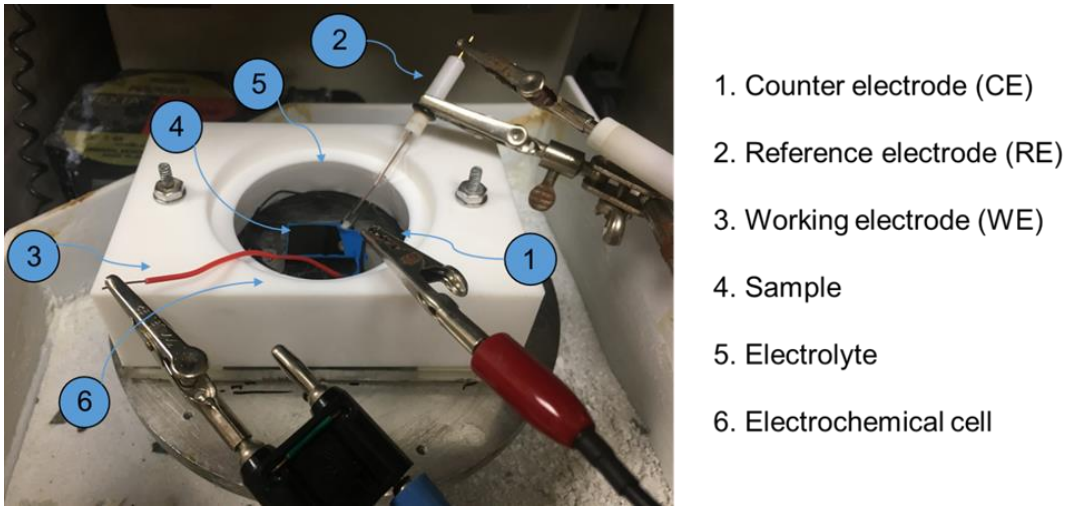

Figure A.3 Photo of custom-made tribocorrosion cell installed on the UMT rotary stage. The cell is made from Teflon with an O-ring at the bottom surface to prevent liquid leakage during tribocorrosion test.

4.2 Tribocorrosion rate measurement principle

4.2.1 Measure tribocorrosion resistance according to the ASTM G119 standard [2], where the total material loss $T = C_0 + W_0 + S$ (see introduction for details).

4.2.1.1 Measure the corrosion rate C_0 from the potentiodynamic test.

4.2.1.2 Measure the pure wear rate W_0 during cathodic polarization from tribocorrosion test. Apply a ball-on-disc configuration using an alumina ball to impose reciprocal mechanical wear in the load range of mN to a few N.

4.2.1.3 For the thin film sample, choose a proper normal load. This ensures that the plastic deformation is confined within the top surface so that the deposited sample thickness is large enough to resemble true bulk material behavior. Such estimation can be made by using Hertzian contact theory [12].

4.2.1.4 Measure the tribocorrosion rate T from tribocorrosion test at OCP.

4.2.1.5 Calculate the synergy S from the above measurements and equation 1.

4.3 Measurement of corrosion rate C_0 from potentiodynamic (PD) test

4.3.1 Prepare the working electrode (i.e., bulk, or thin film metal specimen under analysis). Clean the surface of the metal with acetone, followed by 95% ethanol.

4.3.2 Clean the corrosion cell before every corrosion run. Scrub the cell with household detergent and rinse thoroughly with tap water. Repeat this step 3 times.

4.3.3 Rinse the corrosion cell 3 times with de-ionized water (DI) water to remove potential contaminants found in tap water.

4.3.4 Pour 100 mL of 95% ethanol into the corrosion cell and swirl around to contact all internal surfaces. Pour out the ethanol and repeat this step 3 times.

4.3.5 Leave the corrosion cell under a fume-hood for 30 min to allow all ethanol to completely evaporate.

4.3.6 Take the clean, dry corrosion cell and rinse it with the electrolyte that will be used for the corrosion run. For each rinse, fill the corrosion cell with 40 mL of the electrolyte and repeat this procedure 3 times. For this protocol, rinse the corrosion cell with 3.5 wt.% (0.6 M), pH ≈ 7 sodium chloride aqueous solution (i.e., simulated sea water).

4.3.7 Following the rinse, fill the corrosion cell with 40 mL of electrolyte ready for the reaction.

4.3.8 Setup the three-electrode configuration. Use the Al sample, a standard Ag/AgCl,

and an activated titanium mesh as the working, reference, and counter electrode respectively.

4.3.9 Place the working electrode centrally at the bottom of the corrosion cell and glue the bottom using super glue. Place the exposed Cu wire tip above the expected electrolyte surface height.

4.3.10 Place the reference electrode ~ 1 cm above the working electrode.

4.3.11 Loosely bend the counter electrode to wrap around the specimen under test (working electrode). The distance between the counter and working electrode is ~ 2-4 cm.

4.3.12 Connect electrodes with the potentiostat. Ensure that the electrodes are not touching.

4.3.13 Open the electrochemical software package, which interfaces with the USB controlled potentiostat. Turn the potentiostat on.

4.3.14 Open and use the **Measurement View** to view the potential and current readings of corrosion environment. During the OCP phase where no ramp potential is yet applied the current reading between the working (positive potential) and counter (negative) electrode is around 0 ± 0.01 μA.

4.3.15 Leave the sample to equilibrate and stabilize at OCP within the corrosion cell environment. The time duration for this varies (1 to 6 h) and is dependent on the material tested. Monitor the potential using measurement view to determine if a stabilized condition (i.e., a potential change of less than 50 mV over more than half an hour) is reached.

4.3.16 Run the corrosion test. Following the stabilization of the corrosion potential (E_{corr}), ramp the applied potential in the positive direction relative to the reference electrode.

4.3.17 Select the cyclic voltammetry potentiostat procedure within the setup view from the procedure tab. Enable the following parameters to be sampled for the corrosion run: time, working electrode (WE) potential, and current for the corrosion run.

4.3.18 Select the option to automate the current range. Set the highest current in the range to be 10 mA, and the lowest current in the range to be 10 nA for the WE.

4.3.19 Ensure that the final cut-off selection is controlled through the potential by setting the 'cycle back' parameter to 0.8 mV to allow the hysteresis loop to complete.

4.3.20 Record OCP from the measurement view into the OCP parameter text box. Set the start potential at 100 mV below the recorded OCP value. Set the upper vertex potential to 800 mV, the lower vertex to 100 mV below the start potential and the stop potential to 100 mV below the lower vertex potential. Set the scan rate to 0.167 mV/s (ASTM standard).

4.3.21 Press start. After a few hours, the corrosion test is finished.

4.3.22 View the results in the software.

NOTE: Optical microscopy will be performed after each test. Discard samples showing any indication of crevice corrosion under the stop-off lacquer. The results for each test condition should be repeated at least three times. Fig. A.4 shows representative results of bulk and thin film Al after PD tests in 3.5 wt.% NaCl aqueous solution at pH ≈ 7.

4.3.23 Determine the pitting potential (E_{pit}) from the PD test as the potential at which a rapid increase in corrosion current took place (Fig. A.4).

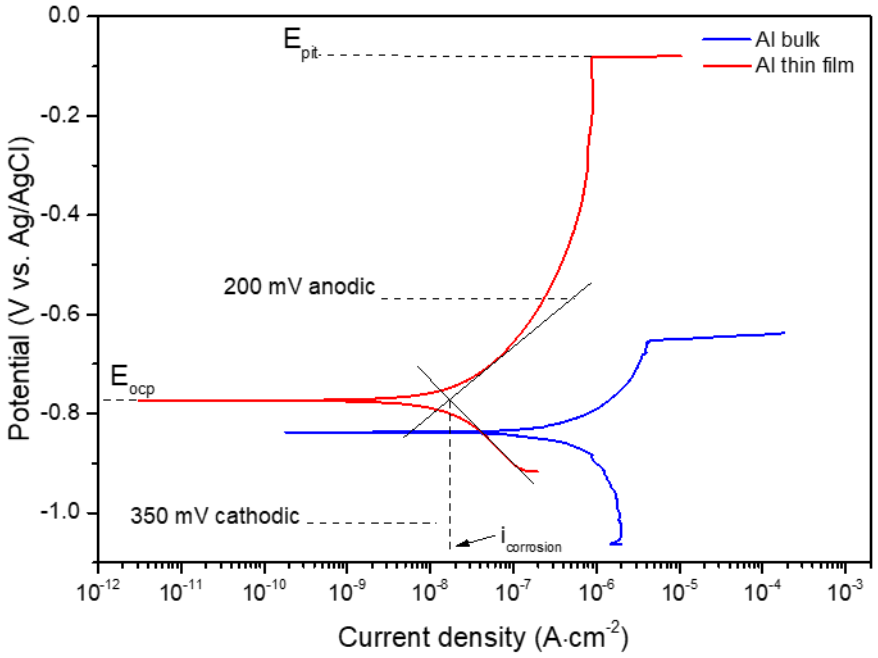

Figure A.4 Representative potentiodynamic polarization curves of Al bulk and thin film after 1 hour immersion in 0.6 M NaCl solution.

4.3.24 Obtain a nominal value of the cathodic polarization slope (β_c) by fitting a straight line to the portion of the polarization curve that corresponds to potentials more than 50 mV lower than E_{oc}.

4.3.25 Obtain a nominal value of the anodic polarization slope (β_a) likewise using the portion of the curve that started at potentials > 50 mV higher than E_{oc} and ended at E_{pit}.

4.3.26 Extrapolate both of those trends to Eoc and suitable average of both to obtain a nominal corrosion current density (i_{corr}) (Fig. A.4).

4.3.27 Calculate corrosion rate C_0 from the corrosion current icorr using Faraday's conversion (1 μA.cm^{-2}≈ 10.9 μm/y) assuming uniform corrosion with the formation of Al^{3+}. The Faraday's equation is $R = M/nF\rho(i_{corr})$, where R is the corrosion rate, i_{corr} is the corrosion current measured from the PD test, M is the atomic weight of the metal, ρ is the density, n is the charge number that indicates the number of electrons exchanged within dissolution reaction, and F is Faraday's constant equivalent to 96,485 C/mol. M/n is the equivalent weight.

4.4 Measurement of wear rate W_0 from cathodic protection test

NOTE: To measure the wear rate, an alumina ball with 4 mm diameter is used as the counter body to scratch on the sample surface while the sample is immersed in the solution, as shown in Fig. A.5. Below is the procedure of cathodic protection test.

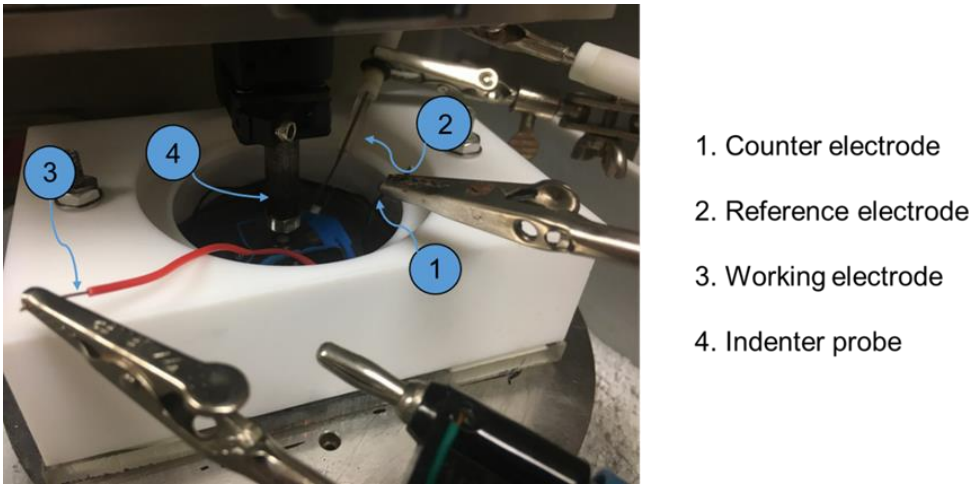

Figure A.5 Photo of tribocorrosion machine during testing where the indenter probe is moving on the sample surface in reciprocal motion.

4.4.1 Perform steps from 4.3.1 to 4.3.13 in section 4.3.

4.4.2 Move the indenter probe down towards the surface of the sample as closer as possible (1 mm distance away from sample surface). Ensure the indenter stays near the center of the sample and there is no electrical contact between the electrodes, the probe, and the sample surface.

4.4.3 Move the indenter up forward for 200 mm. Pour the 3.5 wt.% NaCl aqueous solution into the corrosion cell until all electrode, probe and sample surface are immersed.

4.4.4 Move the indenter probe down towards the sample surface as close as possible. Connect the electrodes with the potentiostat.

4.4.5 Open the electrochemical software package, which interfaces with the USB controlled potentiostat. Turn on the potentiostat.

4.4.6 Select **Experiment** to view **DC Corrosion** and choose **Potentiostatic** mode.

4.4.7 Apply a cathodic potential of 350 mV below OCP. This cathodic potential (350 mV below OCP) is chosen to avoid hydrogen evolution reaction during sliding, which might lead to embrittlement of the samples [13]. The initial potential and final potential is -350 mV vs E_{oc}. The total experimental time is 1,800 s including 300 s of scratching time.

4.4.8 Set up the wear test from the UMT software by applying 1 Hz scratch frequency, 5 mm scratch length, and 0.5 N normal load. Press the **Run** button in the wear system to start the tribocorrosion. Note, the scratch frequency, scratch length, and applied load are testing parameters that can be varied based on the purpose of experiment.

4.4.9 After 1,800 s, the test finished. View the results in the UMT software. For reliable testing, repeat the tests under the same condition for at least three times.

4.4.10 Use a surface profilometer to measure the depth of wear track from at least three different locations along the wear track for each sample. The scan direction is vertical to the scratch line and the scan length is larger than the width of wear track (see Fig. A.6). The radius of the profilometer stylus is 5 μm, the stylus force is 3 mg, and the scan resolution is 0.028 μm/sample.

4.4.11 Export the profile measurement data. Use software to directly integrate the depth below the unworn surface (shaded area in Fig. A.7).

4.4.12 Calculate the cross-sectional wear area as $A = \int_0^a h(x)dx$, where *h(x)* is the surface height as a function of position *x*, and *a* is the wear track width. Using *A*, calculate the wear volume as $V = A \times L$ (*A* is the cross-sectional wear area, *L* is the wear track length = 5mm).

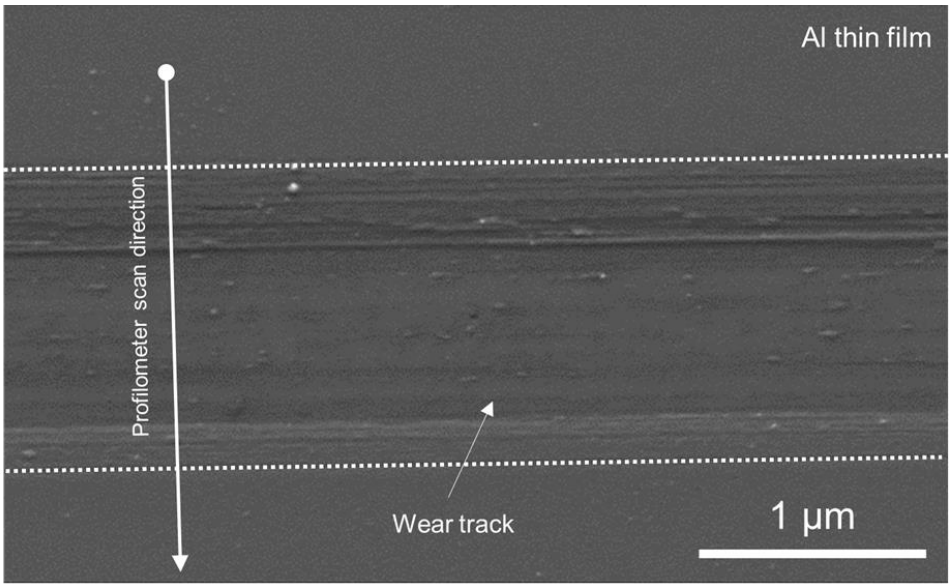

Figure A.6 Scanning electron microscopy image of the wear track after tribocorrosion test. The dashed lines represent the boundaries of the wear track.

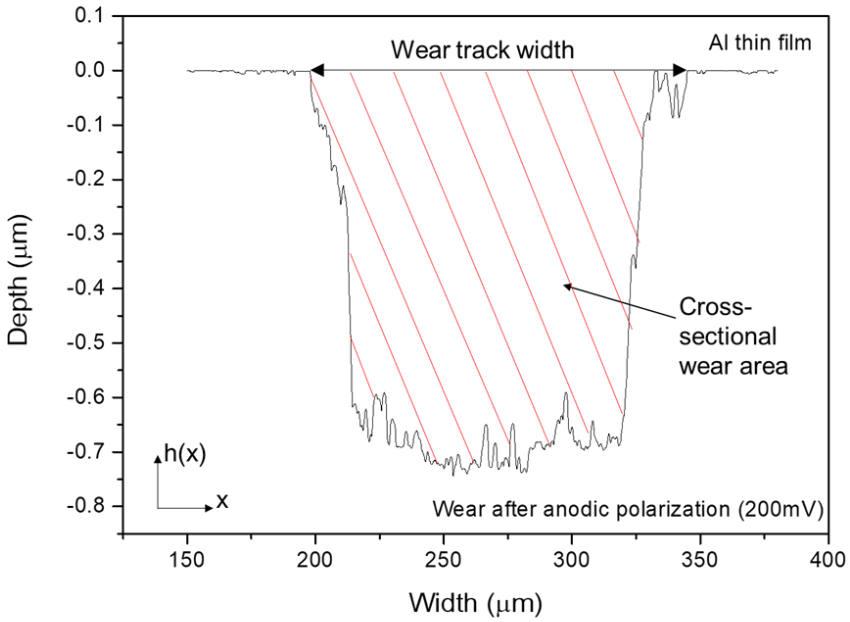

Figure A.7 Typical wear track profile of Al thin film after tribocorrosion test obtained by profilometer.

4.4.13 Finally, calculate the wear rate W_0 as $W_0 = V/L_{tot}$, where L_{tot} is the total sliding distance.

4.5 Measurement of tribocorrosion rate T from tribocorrosion test at OCP

4.5.1 Following steps 4.4.1-4.4.8 except in step 4.4.6, set the applied potential during the test as the OCP.

4.5.2 Once the test is finished, follow step 4.4.13 to calculate T, where $T=V/L_{tot}$.

4.6 Calculation of wear-corrosion synergy S

4.6.1 After performing all previous steps, calculate the wear-corrosion synergy as $S = T - W_0 - C_0$, where T is the total material loss measured at OCP, W_0 is the material loss measured at the cathodic potential primarily due to mechanical wear (where corrosion becomes negligible compared to wear), and C_0 is the material loss due to pure corrosion estimated from PD tests [14, 15]. Note, if C_0 is measured in terms of depth loss/year from the PD test, it is important to convert it to an equivalent volume loss per time for correct calculation of S.

A.5 Representative results

Following the testing protocol described above, the tribocorrosion rate (T) is measured at various potentials. Fig. A.8 represents the material loss obtained for the Al thin film sample after tribocorrosion at the cathodic (350 mV below OCP), open circuit, and anodic (200 mV above OCP) potential. The test was performed in 3.5 wt.% NaCl aqueous solution for 5 min under 0.5 N normal load, at a 1 Hz sliding frequency and 5 mm stroke length. Prior to each test, the OCP was stabilized for 20 min. Fig. A.9 shows the summary of all components of eqn. 1, including the tribocorrosion rate (T), wear rate (W_0), corrosion rate (C_0), and wear-corrosion synergy (S) of Al thin film.

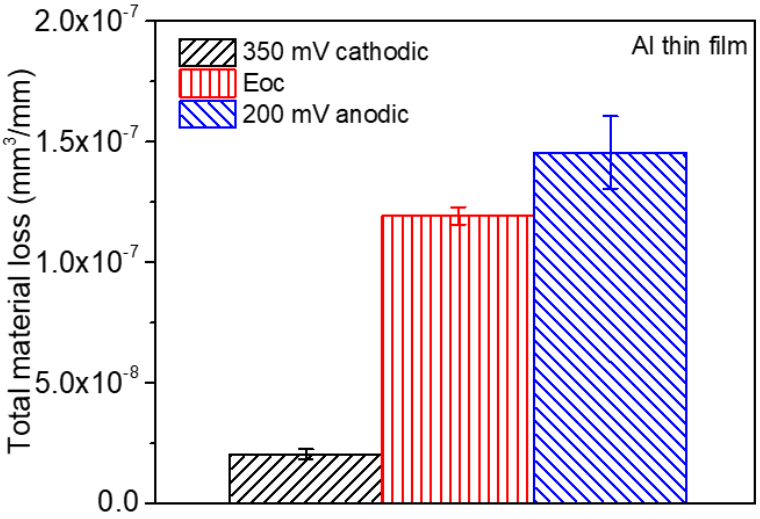

Figure A.8 Summary of tribocorrosion rate (T) of Al thin films at different applied potential. The arrow bar represents one standard deviation from all repeated test results.

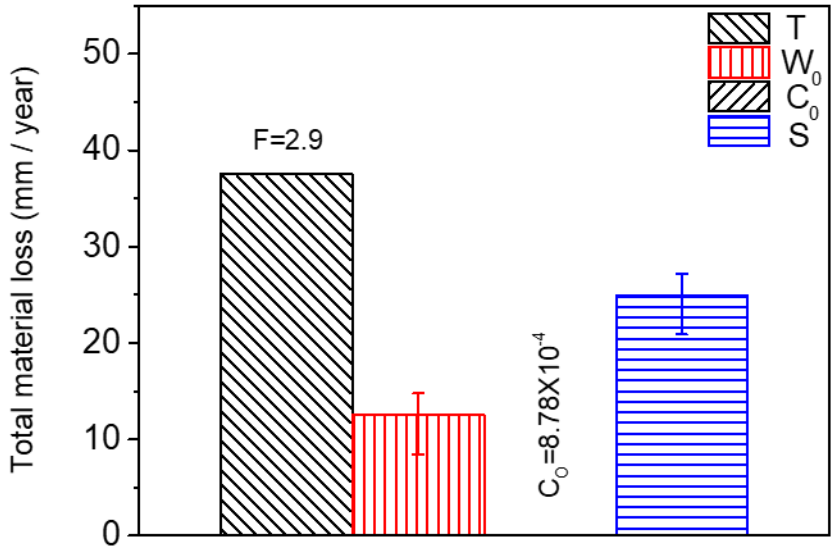

Figure A.9 Summary of tribocorrosion rate (T), wear rate (W0), corrosion rate (C0), and wear-corrosion synergy (S) of Al thin films. The arrow bar represents one standard deviation from all repeated test results.

A.6 Discussion

There are several critical steps within this protocol. First, proper surface preparation of the samples prior to the tribocorrosion tests is critical to ensure good reliability of the performed test and enhance test repeatability. Different bulk alloys are to be prepared following different procedures to ensure a controlled surface roughness,

and removal of any surface contaminants or scales. The procedure described here consists of solely mechanical grinding and polishing. This method generally applies to alloys with medium to high hardness such as Al, Ti, Ni, Cu alloys and steel. For softer alloys such as Mg alloys, electrochemical polishing or ion milling should be coupled with mechanical polishing to achieve the desired surface roughness. Secondly, for thin film sample sputtering, maintaining an ultra-low (< 10^{-6} Torr) vacuum in the sputtering chamber is critical to ensure low defect concentration in the deposited film, which would otherwise affect the corrosion resistance significantly. Thirdly, when preparing either bulk or thin film samples into the working electrode, it is important to ensure a good electrical connection between the sample and the connecting (Cu) wire. In this protocol, conductive tape or conductive epoxy is used. Alternatively, soldering, spot welding or similar techniques may be used. However, the effect of heating during welding on the microstructure and eventually the tribocorrosion resistance of samples have to be evaluated carefully. This is especially important for metals and alloys with low melting point. Finally, since tribocorrosion involves a three-body interaction (including the two bodies in contact, and the third body in between), it is important to ensure that a new ball tip (or a new area of the ball tip) is used when performing repeated tribocorrosion test.

The current protocol evaluates tribocorrosion rate by measuring material loss. Modifications of this protocol can be easily made to evaluate the depassivation and repassivation kinetics of tribocorrosion. This is achieved by tracking the current, potential, and coefficient of friction (COF) evolution during the test. As an example, Fig. A.10 and A.11 show representative results of the evolution of corrosion potential and COF respectively, of Al thin film after tribocorrosion test at OCP. The arrows in Fig. A.10 represent the start and finish of scratching. It can be seen that for passive alloys such as Al, the mechanical disruption during tribocorrosion leads to local breakdown/removal of the passive film on the wear track and exposing a depassivated area which leads to a decrease in the corrosion potential by ~ 20 mV. Our earlier work [16] showed that the magnitude of corrosion potential reduction is strongly related to the microstructure of the metal given the testing parameters (e.g., applied load, sliding speed, temperature) are the same. For Al with higher hardness and finer microstructure, the same applied load may lead to a smaller depassivated area, hence smaller change in corrosion potential. It is also noted that during the open circuit mode, the current is too

low to be detected as the circuit is 'open'. However, current evolution during tribocorrosion test at imposed cathodic or anodic potentials can be monitored. An example can be found in our previous work [16]. Fig. A.12 shows the current evolution of Al thin film during tribocorrosion at an imposed anodic potential of 200 mV more positive than OCP. This anodic potential was selected within the passive region yet well below the pitting potentials. This result can be used to quantify the wear accelerated corrosion. In this case, the total material loss can be evaluated as $T = V_{mech} + V_{chem}$, where V_{mech} and V_{chem} corresponds to the contribution of mechanical and electrochemical material loss, respectively. Specifically, V_{chem} can be regarded as resulting from metal oxidation under anodic applied potential. Thus it can be calculated by Faraday's law as [17-19] $V_{chem} = \frac{QM}{nF\rho}$, where Q is the electrical charge (calculated by multiplying the difference between the average anodic current during and before sliding by the time), M is the molecular weight, n is the oxidation valence, F is Faraday's constant, and ρ is the density of Al. Fig. A.13 shows the typical result of both terms for Al thin films. From the above discussion, it can be seen that an evaluation of the electrochemical parameters change, in addition to the weight loss, will thus offer critical insight to the depassivation kinetics during tribocorrosion.

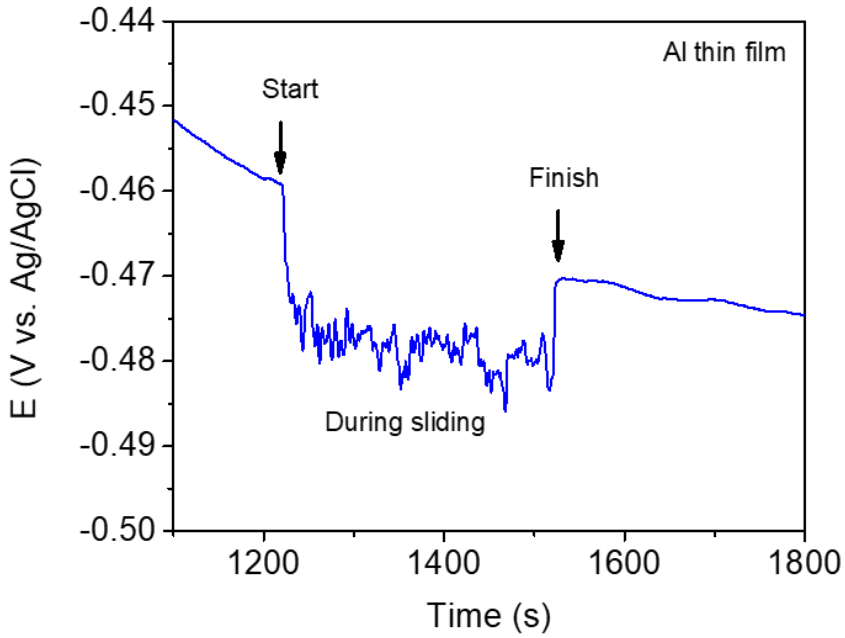

Figure A.10 Evolution of corrosion potential during tribocorrosion test of Al thin film at OCP.

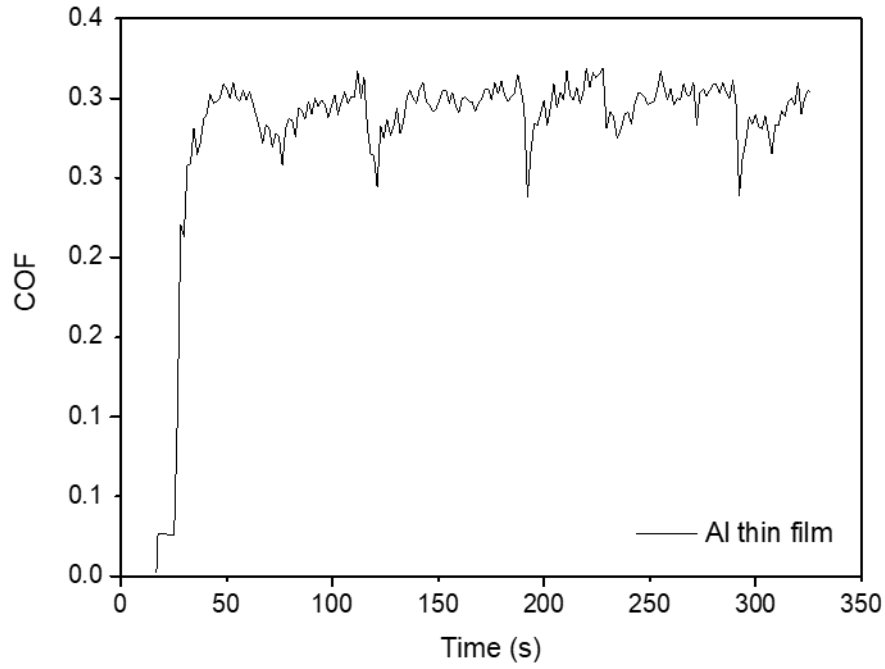

Figure A.11 Evolution of coefficient of friction (COF) during tribocorrosion test of Al thin film at OCP.

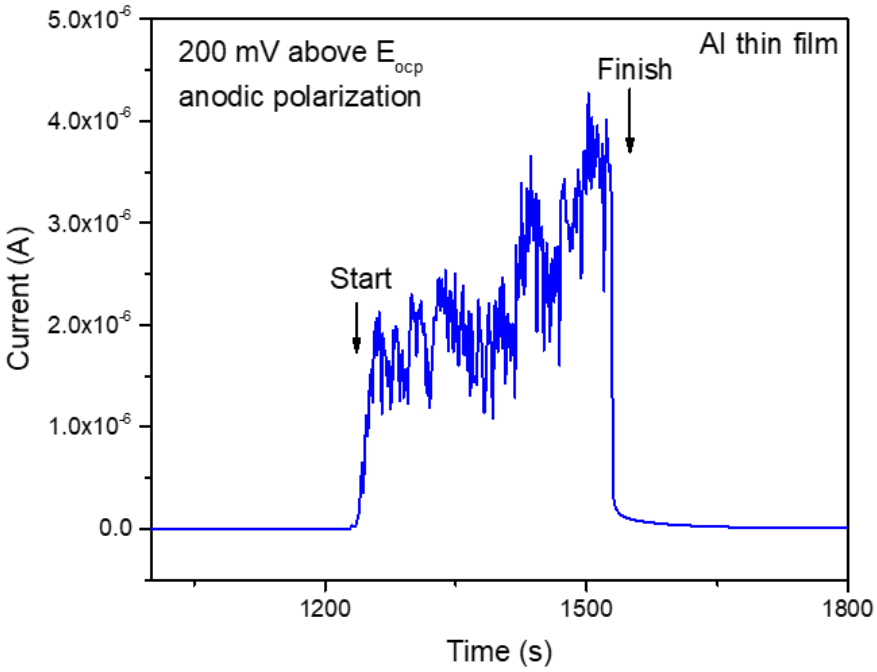

Figure A.12 Evolution of corrosion current during tribocorrosion test of Al thin film at 200 mV above OCP.

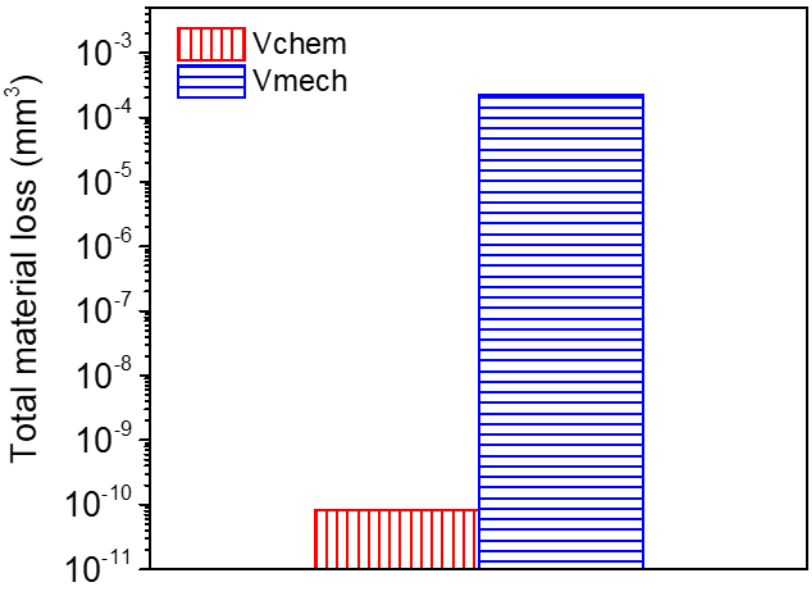

Figure A.13 Summary of mechanical and chemical wear of Al thin film during tribocorrosion test at 200 mV above OCP.

The protocol presented here also bears several limitations. First, the corrosion cell is made from Teflon (polytetrafluoroethylene) or similar material. Thus, all tests were performed near room temperature. For applications that require higher temperature (e.g., above 400 °C for nuclear reactor cores), a special corrosion cell and tip have to be manufactured that will withstand high temperature creep and corrosion. Additional safety is also needed for handling molten salt electrolyte and metallic samples at high temperatures. Secondly, the attachment of a reference electrode near the working electrode (sample) has limited the wear motion to be linear reciprocal. In applications where a rotational motion of the sample is required, a special tribocorrosion setup has to be designed. Thirdly, in the present setup, the wear scratch rate is much faster than the corrosion rate. Hence the contribution of C_0 is negligible compared to all other terms. While corrosion itself did not lead to significant material loss during the limited testing time, its effect on S is significant. In real world applications where mechanical scratch occurs at much lower frequencies, this trend might change where C_0 may become dominant. Finally, special care has to be paid to errors generated during testing. This is especially important for evaluating the wear-corrosion synergy (S), which is derived from tribocorrosion rate (T), wear rate (W_0), and corrosion rate (C_0). Thus errors can be accumulated. To minimize errors generated in T and W0, a non-contact 3D optical profilometer (instead of the contact 2D profilometer) can used to determine the total

material loss volume. To minimize error in C_0, PD tests can be coupled with non-destructive EIS (electrochemical impedance spectroscopy) test to evaluate corrosion rate [20].

As a final note, tribocorrosion rate is not a material property, but rather a system's response that depends on the testing parameters (applied load, sliding speed, etc.), the environment (temperature, pH, salt concentration, etc.), and material properties (hardness, surface roughness, etc.). The protocol presented here is demonstrated using only one set of condition. The readers should consider the differences and adopt appropriate changes in sample preparation, testing setup, and data analysis when dealing with different systems. Alternative testing setup including pin on plate (reciprocating), micro abrasion, cylinder on bar, et al. can be found in [21]. Tribocorrosion is an emerging interdisciplinary subject. It is hoped that this protocol will facilitate both the evaluation of existing engineering materials as well as the design of new materials resistant to both wear damage and corrosion degradation. Such materials become increasingly demanded in future applications such as advanced implantable medical devices, next generation nuclear power plants, and high capacity fast charging batteries, etc., which all require not only a strong and tough material, but one that is robust and reliable when interacting with some very extreme environment.

References

1. Landolt, D. and S. Mischler, *Tribocorrosion of passive metals and coatings*. Woodhead publishing in materials. 2011, Oxford ; Philadelphia: Woodhead. xxi, 554 p.
2. .
3. Mischler, S., *Sliding Tribo-Corrosion of Passive Metals: Mechanisms and Modeling.* Tribo-Corrosion: Research, Testing, and Applications, 2013. **1563**: p. 1-18.
4. Landolt, D., S. Mischler, and M. Stemp, *Electrochemical methods in tribocorrosion: a critical appraisal.* Electrochimica Acta, 2001. **46**(24-25): p. 3913-3929.
5. Macdonald, D.D., *Passivity - the key to our metals-based civilization.* Pure and

Applied Chemistry, 1999. **71**(6): p. 951-978.

6. Obadele, B.A., et al., *Tribocorrosion behaviour of laser cladded biomedical grade titanium alloy.* Materials and Corrosion, 2015. **66**(10): p. 1133-1139.
7. Wolf, D., et al., *Deformation of nanocrystalline materials by molecular-dynamics simulation: relationship to experiments?* Acta Materialia, 2005. **53**(1): p. 1-40.
8. Rupert, T.J. and C.A. Schuh, *Sliding wear of nanocrystalline Ni–W: Structural evolution and the apparent breakdown of Archard scaling.* Acta Materialia, 2010. **58**(12): p. 4137-4148.
9. Pokhmurs'kyi, V.I. and V.M. Dovhunyk, *Tribocorrosion of Stainless Steels (Review).* Materials Science, 2010. **46**(1): p. 87-96.
10. Davis, J.R., *Surface engineering for corrosion and wear resistance*. 2001, Materials Park, OH: ASM International : Institute of Materials. viii, 279 p.
11. Song, D., et al., *Corrosion behavior of equal-channel-angular-pressed pure magnesium in NaCl aqueous solution.* Corrosion Science, 2010. **52**(2): p. 481-490.
12. Johnson, K.L., *Contact Mechanics*. 2012.
13. Mischler, S., *Triboelectrochemical techniques and interpretation methods in tribocorrosion: A comparative evaluation.* Tribology International, 2008. **41**(7): p. 573-583.
14. Watson, S.W., et al., *Methods of Measuring Wear Corrosion Synergism.* Wear, 1995. **181**: p. 476-484.
15. Assi, F. and H. Böhni, *Study of wear–corrosion synergy with a new microelectrochemical technique.* Wear, 1999. **233-235**: p. 505-514.
16. Mraied, H. and W.J. Cai, *The effects of Mn concentration on the tribocorrosion resistance of Al-Mn alloys.* Wear, 2017. **380-381**: p. 191-202.
17. Vieira, A.C., et al., *Mechanical and electrochemical deterioration mechanisms in the tribocorrosion of Al alloys in NaCl and in NaNO3 solutions.* Corrosion Science, 2012. **54**: p. 26-35.

18. Mischler, S., A. Spiegel, and D. Landolt, *The role of passive oxide films on the degradation of steel in tribocorrosion systems.* Wear, 1999. **225**: p. 1078-1087.
19. Mischler, S. and A.I. Munoz, *Wear of CoCrMo alloys used in metal-on-metal hip joints: A tribocorrosion appraisal.* Wear, 2013. **297**(1-2): p. 1081-1094.
20. Mraied, H., W.J. Cai, and A.A. Sagues, *Corrosion resistance of Al and Al-Mn thin films.* Thin Solid Films, 2016. **615**: p. 391-401.
21. Mathew, M.T., et al., *Construction of a tribocorrosion test apparatus for the hip joint: Validation, test methodology and analysis.* Wear, 2011. **271**(9-10): p. 2651-2659.